The Institute of Paper Chemistry

Appleton, Wisconsin

Doctor's Dissertation

An Investigation of Time-Mean Velocity and Consistency Distributions in a Fiber Suspension Jet

David S. Walseth

January, 1976

AN INVESTIGATION OF TIME-MEAN VELOCITY AND CONSISTENCY DISTRIBUTIONS IN A FIBER SUSPENSION JET

A thesis submitted by

David S. Walseth

B.S. 1968, Stanford University

M.S. 1970, Lawrence University

in partial fulfillment of the requirements
of The Institute of Paper Chemistry
for the degree of Doctor of Philosophy
from Lawrence University
Appleton, Wisconsin

January, 1976

TABLE OF CONTENTS

SUMMARY

An experimental apparatus was developed for the study of an axially symmetric submerged and turbulent jet discharged into a cylindrical tank. Water jets were used to check the effects of the confining tank on the jet velocity profiles and momentum fluxes. Suspension jets of nylon-12 fibers in water were then investigated to determine if the presence of fibers would significantly affect the velocity profiles, momentum fluxes, and consistency distributions. Local time-mean velocities and consistencies of the suspension jets were measured by a water purged pitot tube and a water purged optical probe, respectively. The latter was calibrated in a flowing fiber suspension of known velocities and consistencies.

Velocity profiles in water jets showed the characteristic jet shape, and were correlated by a reduced form of the Gaussian error curve, in agreement with previous published results. The momentum flux of confined jets was found to decrease significantly with the increasing axial distance. This finding is in apparent variance with the assumption of momentum conservation in the analysis of ideal jets. A momentum balance in the experimental jet flow system showed that recirculation flows surrounding the jet could explain the discrepancy between theory and experiment. The unsteady tank flow also caused slow oscillation of the jet.

Reduced velocity profiles in the suspension jets at consistencies up to 0.75% showed very similar jet characteristics. The local suspension velocities, however, were always lower than those at the corresponding stations in a water jet. Therefore, the presence of fibers does affect the jet flow or its interaction with the surrounding tank flow.

The suspension jet showed no significant consistency distribution across its flow at various axial distances. Thus it appears that turbulent diffusion in the jet does not lead to consistency variations as long as the initial consistency in the jet tank system is uniform.

INTRODUCTION

The hydrodynamic analysis of a suspended solid phase of long, flexible fibers in turbulent flow is an important fundamental problem. Fiber networks have a unique influence on the turbulent flow properties of suspensions that is not completely understood. Sanders and Meyer (1,2) have presented a new theoretical approach to the problem, based partially on earlier work by Nelson (3) and Emmons (4). Sanders applied this approach to turbulent pipe flow and obtained agreement with measured velocity and consistency profiles in wood fiber suspension (1,5).

TURBULENT PIPE FLOW OF FIBER SUSPENSIONS

Most studies of the flow of fiber suspensions have been made in pipe flow. Some early reported observations of the effects of fiber networks on the flow properties of fiber suspensions were also made in Couette flow (6-8). Pipe flow studies completed before the systematic investigations began at Massachusetts Institute of Technology were reviewed by Daily and Bugliarello (9).

Ippen, et al. (10) considered four possible experimental flow patterns:

1. Turbulence grids
2. Circular pipe flow
3. Submerged jets
4. Expansions and contractions

Pipe flow was chosen for their study because it had the potential to provide more information than any of the other systems. Mih and Parker (11) observed that pipe flow is also simple experimentally. They introduce an annular purge impact probe for local velocity measurements. Recent studies of

turbulent suspension flow have been limited to pipe loops. Sanders has reviewed this literature (5).

One contribution of the studies by Daily and Bugliarello was an extensive experimental verification of two distinct regimes of turbulent suspension pipe flow (9). These flow regimes, reported earlier by Mason and coworkers (12,13), are called plug turbulence and damped turbulence. The distinction between the two regimes is based on the kind of dependence of the friction factor on the Reynolds number.

In laminar suspension pipe flow, the fibers form a coherent plug whose diameter is nearly equal to the inside diameter of the pipe. The regime called plug turbulence begins when the Reynolds number of the water has increased to a point where the flow in the water annulus around the plug becomes unstable and turbulent. High shear in the annulus together with turbulent stresses apparently causes increasing disintegration of the plug as the velocity increases. As this process ensues, the friction factor drops below that of pure water.

Damped turbulence begins when the plug is no longer coherent and the suspension flow has become turbulent across the entire pipe section. The fibers still apparently form fragmentary networks that affect the momentum transfer characteristics of the suspension. Within this regime the friction factor is practically independent of the Reynolds number and is everywhere below that of pure water: the fibers have a drag reducing effect.

Seely (14) reported, however, that at much higher velocities the friction factor approached that of pure water. Sanders verified the existence of a third regime which he called Newtonian turbulence. In this regime the turbulent intensity had dispersed the fiber network to such an extent that the fiber phase no longer affected the momentum transfer in the suspension (5).

Topics of interest in the field of turbulent fiber suspension flow include the pipe friction factor dependence on the Reynolds number, turbulent intensity and scale (15-17), flocculation (12,18-20), local time-mean velocity and consistency measurements. Several authors have reported time-mean velocity distributions in pipes (5,11,14) using a special purged impact probe (11). Sanders also measured time-mean consistency distributions with an optical probe (5). The conclusions of this pipe flow work are given in the following sections.

VELOCITY PROFILES

For single phase Newtonian fluids velocity distribution data for fully developed turbulent flow can be correlated by Prandtl's logarithmic distribution law:

$$v^+ = 1/\kappa \ln s^+ + B, \qquad (1)$$

where $v^+ = \bar{v}/\sqrt{\tau_o/\rho} = \bar{v}/v_*$

$$s^+ = s\rho\sqrt{\tau_o/\rho}/\mu = s\rho v_*/\mu$$

The von Karman constant, κ, and the intercept, B, are constant for all Newtonian fluids.

Mih and Parker (11), Seely (14), and Sanders (5) all represented their fiber suspension velocity distribution data according to similar logarithmic relationships. They found that the apparent von Karman constant, κ_*, is lower than that for the Newtonian fluids (11). Seely (14) and Sanders (5) showed that it increased with increasing velocity and approached the constant Newtonian value at high flow rates. Sanders also verified that κ_* decreased from its Newtonian value as the suspension consistency was increased at constant velocity (5).

Sanders and Meyer wrote and solved by use of Prandtl's mixing length hypothesis the new two-phase equations (1,5). Their final velocity distribution equation is also a formula for κ_*:

$$dv^+/d \ln s^+ = (\sqrt{\bar{\varepsilon}}/\kappa)\sqrt{1-\mu\bar{a}\bar{\varepsilon}\bar{v}_{rel}R/\rho v_*^2} = 1/\kappa_* \qquad (2)$$

The expression $\mu\bar{a}\bar{\varepsilon}\bar{v}_{rel}$ is a fiber-water drag term where $\bar{v}_{rel}$ is the difference between mean fiber velocity and mean water velocity at a point in the suspension. The resistance coefficient, $\bar{a}$, is a function of average consistency and fiber properties. Sanders and Meyer used Equation (2) to determine the unknown relative velocity between fibers and water, $\bar{v}_{rel}$, from the experimental data. The values of $\bar{v}_{rel}$ were small, negative, and decreased slightly with increasing flow rate (1,5). If an average known value of $\bar{v}_{rel}$ were assumed to be independent of the other experimental variables, Equation (2) could be used to predict κ_*. Sanders and Meyer did this (1,5). If this assumption were not made, the relative velocity would have to be measured independently or calculated from a second equation before Equation (2) could actually predict κ_*. According to Equation (2), the effect of the fibers on κ_* diminishes as the wall shear stress, ρv_*^2, increases, suggesting the existence of the Newtonian turbulent regime reported by Seely (14).

Measured velocity profiles in suspension flow in the turbulent zone of tube flow are similar to Newtonian profiles. They obey a logarithmic distribution law in which the coefficients are not constant but depend on velocity, consistency, pipe diameter, and fiber properties. The fibers obviously affect the turbulent momentum transfer process and so alter the slopes of the profiles.

CONSISTENCY PROFILES

Sanders reported the first measurement of time-mean consistency distributions in pipe flow (5). He studied flow in the damped turbulent regime. The fiber distribution that he measured is not uniform; the consistency was higher at the center line than at the pipe wall. The consistency profile became sharper with increasing flow rate at a given average consistency. As the flow rate increased and the consistency decreased the distribution became independent of flow rate and nearly uniform.

The solution of the water phase continuity equation by Sanders and Meyer, also employing the mixing length hypothesis yielded a consistency distribution for dilute suspensions in pipe flow (1,5):

$$\ln(1-\bar{c}) = (C_\lambda/\kappa_\sigma\kappa_\lambda)(\kappa_*/v_*)(\ln s - \ln s_o), \qquad (3)$$

where $\bar{c}$ is the average volume fraction of the fibers and s is the distance from the pipe wall. Equation (3) predicts that $\ln(1-c)$ is a linear function of $\ln s$. Sanders' data verified this relationship. The slope of the plot of $\ln(1-c)$ against $\ln s$ contains the apparent von Karman constant, κ_*, a "void fraction exchange term," $C_\lambda/\kappa_\sigma\kappa_\lambda$, and the friction velocity, v_* (1,5). The water boundary layer thickness, s_o, and $C_\lambda/\kappa_\sigma\kappa_\lambda$ can be evaluated from the data.

LIMITATIONS OF THE STUDY OF SUSPENSION PIPE FLOW

Pipe flow studies have produced information about some aspects of the nature of turbulent fiber suspension flow. Suspension flow characteristics have been described on the basis of both actual results and qualitative observations. Thus, it is supposed that a coherent fiber structure could be possible in the presence of turbulence at relatively low Reynolds numbers

in other fiber suspension flow systems. It is generally believed that damped turbulence might exist in any suspension flow of pulp fibers at the right Reynolds number and consistency where a dynamic fiber network alters the momentum transport characteristics of the suspension. It has not been previously suggested that time-mean consistency nonuniformities might exist other than in pipe flow but such a speculation is possible.

Flow characteristics in a pipe are determined to a large extent by the influence of the pipe wall. The presence of the wall, imposing the no-slip condition, dictates the form of the velocity distribution and affects momentum transport. The wall, however, also certainly has other, independent, effects on the suspension flow. The wall could be the major cause of coherent fiber plugs, and even of dynamic fiber networks and nonuniform fiber distributions which could, therefore, be independent of the other flow characteristics. If this were so, then even turbulence damping might possibly not occur in flow systems without walls so that other flows of suspensions would always be in the regime of Newtonian turbulence.

Fiber suspension flow has not yet been studied in a flow system where walls are not a major influence. Until it has been, generalizations about fiber suspension flow based on pipe flow results cannot be verified. The question of wall effects must be settled by studying suspension flow in a flow system without walls.

A relatively simple turbulent flow system exists in which walls are not a factor: the submerged jet. The jet also does not have the pressure gradient of pipe flow and in it viscous forces are probably negligible. There is a time-mean velocity gradient but the velocity distribution is different from that in turbulent pipe flow. Study of fiber suspension flow in the turbulent jet would help to answer questions about the effect

of walls on suspension behavior as well as to provide a different flow system for the application of the two-phase equations.

SUBMERGED JET FLOW

An ideal submerged jet is a directed flow of fluid through a small orifice into an unbounded volume of that same fluid that is otherwise at constant velocity. Submerged jet flow becomes turbulent, or changes its turbulence character at a short distance from the orifice (21-23). Vortex sheets are produced along the tangential separation surface between the jet stream and the surrounding fluid at relative rest. Eddies diffuse from this boundary layer into the undisturbed fluid. As fluid is entrained in a downstream direction the width of the region of mean velocity gradient increases. Since the total momentum of an ideal pure fluid jet must be conserved, the mean velocities simultaneously decrease. Momentum transfers radially from the jet axis toward and into the undisturbed fluid.

Two simple orifice shapes have been previously studied both experimentally and theoretically. A long rectangular orifice creates a two-dimensional jet; a circular orifice creates an axisymmetric jet. The physical characteristics and theoretical treatment of the two are similar. This thesis is concerned with the axisymmetric jet and the following discussion deals with it.

GENERAL JET CHARACTERISTICS

A submerged jet has two distinct regions of flow separated from each other by a transition zone (Fig. 1). An initial region exists within a few orifice diameters of the jet origin. This region is a cylindrical zone of constant velocity surrounded by a turbulent boundary layer that grows continuously, eating away the constant velocity core. A transition zone

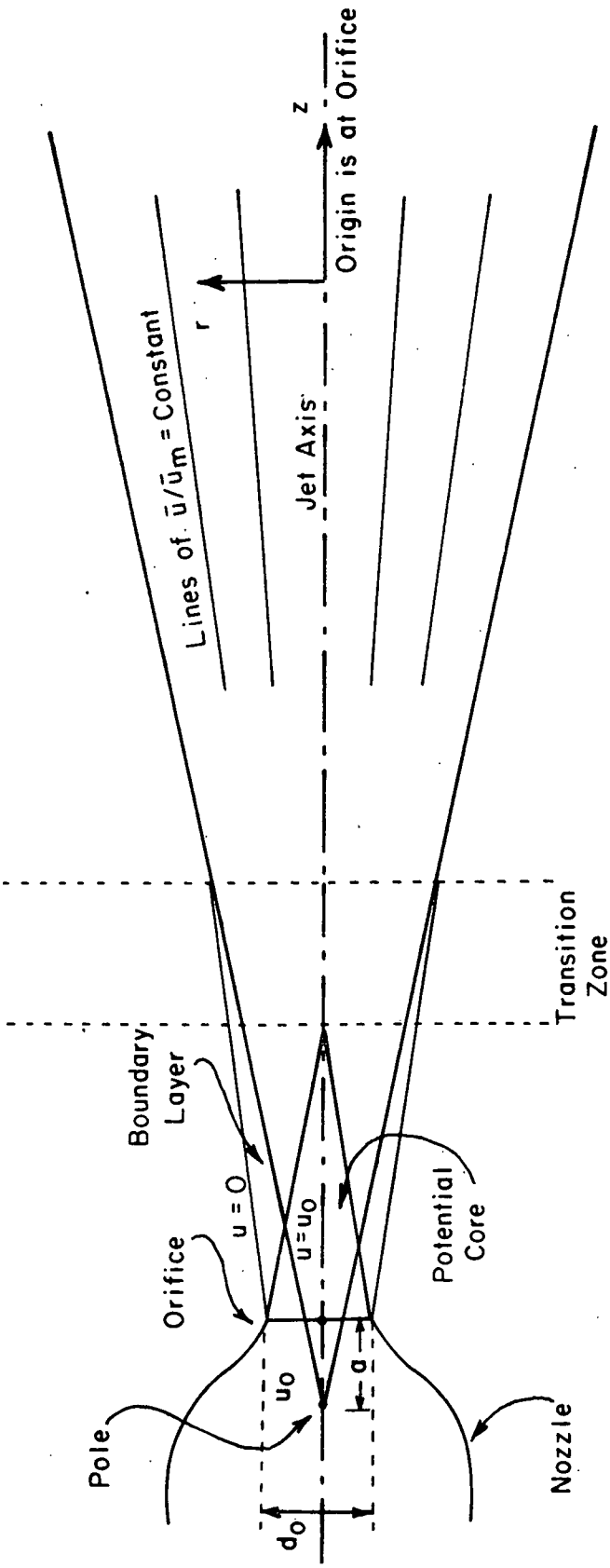

Figure 1. Axisymmetric Submerged Jet

begins where the core disappears and persists until all of the flow has become fully developed turbulent. The dividing lines between the regions of the jet are not exact; they must be considered merely as convenient nominal designations.

After the short transition zone the ideal axisymmetric submerged jet becomes identical in appearance to a flow of fluid from an infinitely small point source. In this main region lines of equal dimensionless velocity (the ratio of local velocities to the maximum velocity in that cross section), u/u_m, are straight and converge at the pole of the jet (23). In Fig. 1 this virtual jet origin is shown inside the orifice nozzle; it does not necessarily fall in the plane of the nozzle orifice. Experimental evidence has shown that the main region is established at a distance of between eight and ten orifice diameters from the origin (22). Most previous studies of submerged jets included measurements and semiempirical analyses of the time-mean velocity profiles in this main region. The shapes of the profiles are well established.

Cylindrical polar coordinates are the natural coordinate system for the analysis of an axisymmetric jet. The origin of the coordinate system is at the center of the nozzle orifice. The axial coordinate is z, the jet axis; the radial coordinate is r (Fig. 1). There is complete symmetry about the z-axis so consideration of the angular coordinate is not necessary. The distance from the "virtual origin" of the main region of the jet to the origin of the coordinate system (along the z-axis) is named a.

The radial velocities, v, are nonzero but are small in comparison to the longitudinal velocities, u. A plot of the local time-mean velocities, $\bar{u}$, against radial distances, r, in this plane through the z-axis is a two-

dimensional time-mean velocity profile. A family of several such curves at different z distances characterizes the main region of a particular submerged jet.

Two-dimensional experimental velocity distributions are similar in shape to the Gaussian error curve (22,24). They decrease in amplitude and become wider with increasing distance from the jet origin. An important property of these jet velocity profiles becomes apparent when the velocities and radial distances are put into dimensionless form. The dimensionless velocity is $\bar{u}/\bar{u}_m$; a suitable dimensionless radial distance is the actual radial distance divided by a characteristic measure of the profile width. The commonly accepted measure of width, r_c, is the distance from the z-axis at which $\bar{u}/\bar{u}_m = 0.5$. When velocity distributions at different z distances are reduced and replotted, they all fall on a single universal curve for axisymmetric jets. The individual profiles are said to be similar because they can be expressed in terms of the single variable r/r_c (or r/z) in the form $\bar{u}/\bar{u}_m = g(r/r_c)$, which describes the universal curve. An analysis based on the experimentally verified similarity relationship concludes that r_c should be directly proportional to z in the main region of the ideal jet (21-23). Experiments have verified this relationship approximately (22,24) for submerged jets in unconfined space.

In an unconfined submerged jet the "momentum" of the jet at an axial distance, z, is

$$M(z) = 2\pi \int_0^\infty u^2 r dr = M_o = \pi/4 \; d_o^2 u_o^2 \qquad (4)$$

Thus M_o is a known quantity for each jet. The value of $M(z)$ can be determined from experimental velocity profiles by graphical integration.

The jet momentum is dependent only on the initial jet conditions and does not vary with z. This is the underlying assumption of the simple submerged jet theory as presented in all textbook discussions of jets. Equation (4) can be expressed in nondimensional form with $\eta = r/(z+a)$:

$$2\pi\, u_m^2(z+a)^2 \int_0^\infty (u/u_m)^2 \eta d\eta = M_o \qquad (5)$$

Thus, conservation of momentum in the ideal jet demands that

$$u_m = m/(z+a), \qquad (6)$$

where m is an experimental constant. Conservation of momentum (and the related condition of profile similarity) is a necessary assumption for the complete solution of the equations in the following section.

THEORETICAL JET VELOCITY DISTRIBUTIONS FOR PURE FLUIDS

The theoretical analysis of jet flow for pure fluids begins with the Navier-Stokes equations of continuity and motion for an incompressible fluid with a constant viscosity. The particular flow conditions of the turbulent jet and its surroundings permit viscous terms and pressure terms to be dropped. The equations are written for turbulent flow as follows:

$$\partial\bar{u}/\partial z + \partial\bar{v}/\partial r + \bar{v}/r = 0, \qquad (7)$$

and

$$\bar{u}(\partial\bar{u}/\partial z) + \bar{v}(\partial u/\partial r) + \partial\overline{u'^2}/\partial z + 1/r(\partial r\overline{u'v'}/\partial r) = 0 \qquad (8)$$

Multiplication of Equation (8) by r and integration over r leads to the total momentum balance and Equation (4). Although u' is usually larger than v', they are both of the same order of magnitude. In submerged jet flow the velocities and fluctuations of velocities change more slowly along the axis than they do in the radial direction. Thus, $\partial\overline{u'^2}/\partial z$ is

smaller than $\partial\overline{u'v'}/\partial r$ (except near the edge of the jet) (22). When the term $\partial\overline{u'^2}/\partial z$ is neglected, the final approximate jet flow equation is traditionally written (21-23):

$$\bar{u}(\partial\bar{u}/\partial z) + \bar{v}(\partial\bar{u}/\partial r) + 1/r(\partial r\overline{u'v'}/\partial r) = 0 \qquad (9)$$

If Equation (7) and Equation (9) could be solved together, they would yield the approximate velocity distribution, $\bar{u}/\bar{u}_m = f(r/z)$.

Unfortunately, the two equations contain three unknown variables and cannot be solved exactly. The term $1/r\partial(r\overline{u'v'})/\partial r$ is commonly referred to as the turbulent Reynolds shear stress. Before a solution of the equations can be attempted, some approximation to the variable $\overline{u'v'}$ must be made in terms of one or both of the other two dependent variables $\bar{u}$ and $\bar{v}$. The various semiempirical approximations proposed for $\overline{u'v'}$ are a convenient step in the traditional analysis of all turbulent flows. These relationships contain a single factor which must be measured experimentally before the resulting solutions are complete.

Most of the accepted approximations to $\overline{u'v'}$ are analogous to the Newtonian laminar shear stress formula, $\tau_{rz} = \mu(\partial u/\partial r)$. The first approximation attempt, by Boussinesq, was the definition of a constant turbulent "eddy viscosity," A_t, so that

$$\overline{u'v'} = A_t(\partial\bar{u}/\partial r) \qquad (10)$$

Prandtl followed this later with his widely used mixing length assumption:

$$\overline{u'v'} = \pm \ell^2 \, \partial\bar{u}/\partial r|\partial\bar{u}/\partial r| \qquad (11)$$

With the mixing length ℓ assumed directly proportional to z the mixing length theory permitted useful solutions to pipe flow, and submerged jet

equations. Sanders applied it to his turbulent fiber suspension pipe flow equations (5).

Although mixing-length theory sometimes leads to acceptable results, some of its assumptions and conclusions are physically unsatisfactory (21,23). Prandtl, himself, later established a simpler expression for $\overline{u'v'}$ that counters some of the earlier difficulties. For submerged jet flow it can be written as

$$\overline{u'v'} = \kappa' b \bar{u}_m (\partial \bar{u}/\partial r), \tag{12}$$

where κ' is an experimental constant (21,23). In the axisymmetric case, the jet width, b, is proportional to z, so that $b/z = k$, and $\bar{u}_m$ is inversely proportional to z, so that $\bar{u}_m = m/z$. Equation (12) becomes

$$\overline{u'v'} = \kappa' k_m (\partial \bar{u}/\partial r), \tag{13}$$

or

$$\overline{u'v'} = A_t (\partial \bar{u}/\partial r), \tag{14}$$

if $A_t = \kappa' k_m$.

Reichardt (25) noticed the striking similarity of jet and wake velocity distributions to the normal probability expression:

$$n(x) = 1/\sqrt{2\pi}\, \exp(-x^2/2) \tag{15}$$

He established a set of equations whose solutions involve the normal error curve. A solution to the equation for the axisymmetric jet is of the form

$$\left.\begin{aligned} \overline{u^2} &= \overline{u_m^2}\, \exp(-\xi^2/2) \\ \xi &= r/b \end{aligned}\right\} \tag{16}$$

Tollmien solved Equations (7) and (9) for the two-dimensional jet using Prandtl's mixing length concept. Following Tollmien's solution technique, Abramovich presented a solution for the axisymmetric jet (23). In both cases a series solution was necessary. Curve 1 of Fig. 2 is the universal velocity profile computed from this solution.

Schlichting (21) and Abramovich (23) both present a solution of the axisymmetric jet problem based on the new Prandtl free turbulence assumption. An analytical solution can be written:

$$\left.\begin{aligned} \bar{u}/\bar{u}_m &= 1/(1 + 0.125\ \xi^2)^2 \\ \xi &= \sigma\ r/(z+a) \end{aligned}\right\} \qquad (17)$$

Any semiempirical solution contains an unpredictable factor such as σ which must be determined from the experimental data. Figure 2 also shows the distributions predicted by Equation (17) and by a reduced error curve equation (24):

$$\bar{u}/\bar{u}_m = \exp[-0.694(r/r_c)^2] \qquad (18)$$

The value of the axial velocity is determined from the assumption of the conservation of total momentum flux if the jet is ideal and not confined.

It is interesting to note a similarity in form between Equation (17) and an approximate form of the normal error curve equation obtained by an infinite series expansion. The Abramovich analysis gives the formula,

$$1.82/\sigma = r_c/(z+a) \qquad (19)$$

Using this relationship the new free turbulence Prandtl-Abramovich solution, Equation (17) can be expanded to

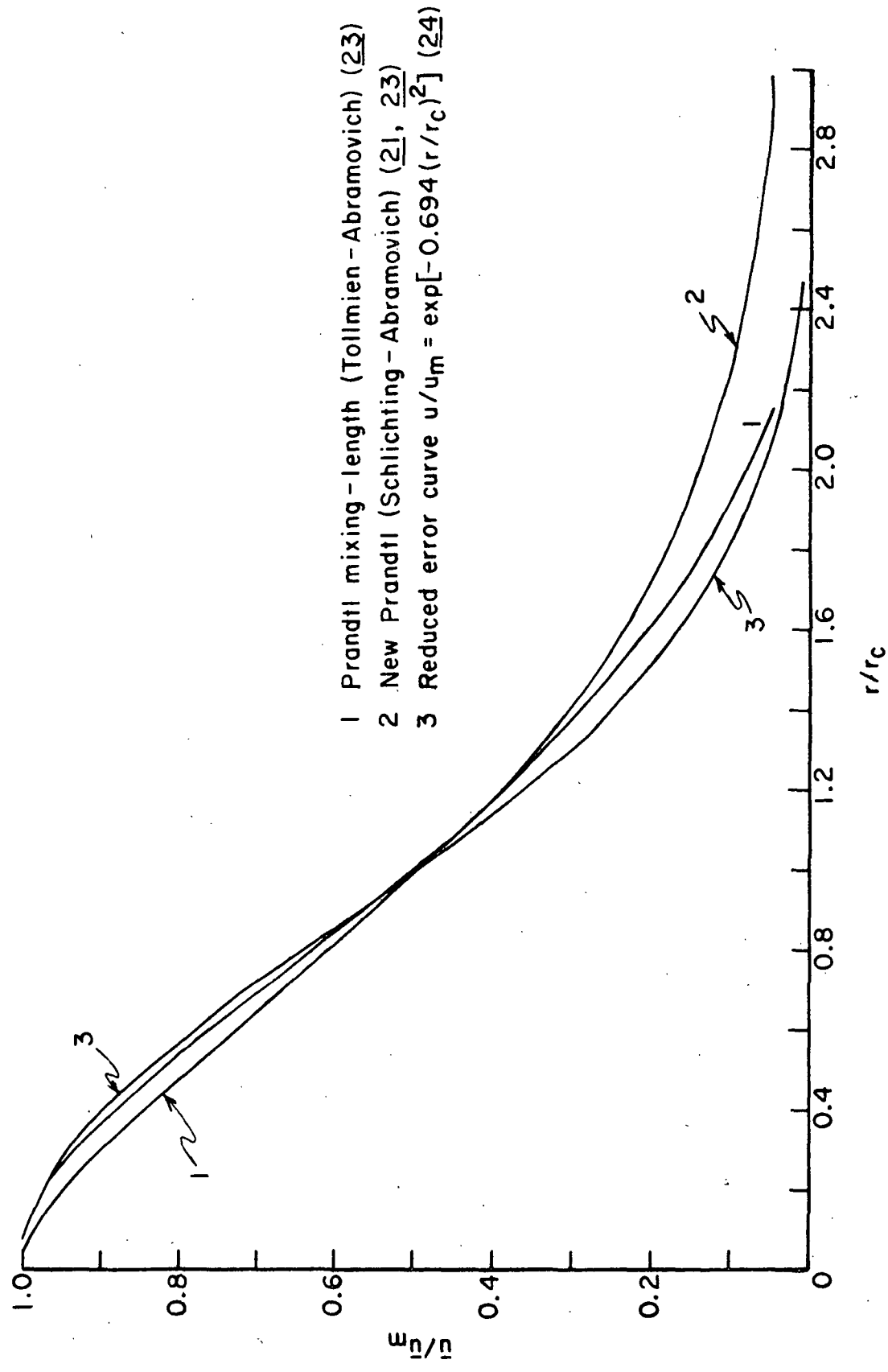

Figure 2. Reduced Theoretical Velocity Profiles

$$\bar{u}/\bar{u}_m = 1/[1 + 0.828\ R^2 + (0.414)^2\ R^4], \qquad (20)$$

where $R = r/r_c$. The reduced normal error curve form by Gaylord (24), Equation (18), can be expanded by the use of a series approximation to give

$$\bar{u}/\bar{u}_m = 1/\left[1 + 0.694\ R^2 + \frac{0.694^2}{2} R^4 + \ldots + \frac{(0.694)^{10}}{10!} R^{20}\right] \qquad (21)$$

Ten terms of the series are required for convergence near $R = 1.5$. An examination of the two equations shows why the two curves approximate each other at values of R below unity in Fig. 2. The error curve values for $\bar{u}/\bar{u}_m$ are slightly higher until $r = r_c$. Beyond this point the higher order terms of the error curve series approximation produce lower values of $\bar{u}/\bar{u}_m$ than the Prandtl semiempirical relationship.

In fact, the assumption of one or another of the proposed semiempirical relationships for $\overline{u'v'}$ does not have a great effect on the calculated mean velocity distribution (26). The curves are all nearly the same over most of the width of the jet, although none are exactly correct, and the error curve may be the closest of all to experimental results (24,26).

The two semiempirical approaches just described also lead to expressions for the dependence of $\bar{u}_m$ on z for a given r_o and u_o. The mixing length approach solution by Abramovich gives

$$\bar{u}_m/u_o = 0.645\ \sigma/\left(\frac{z+a}{r_o}\right) = 1.176\ (r_o/r_c) \qquad (22)$$

The new Prandtl assumption predicts a lower value:

$$\bar{u}_m/u_o = 0.612\ \sigma/\left(\frac{z+a}{r_o}\right) = 1.115\ (r_o/r_c) \qquad (23)$$

As mentioned in the previous section, these results are based on the total momentum flux conservation assumption for the ideal jet. The new Prandtl

equation does not approach $\bar{u}/\bar{u}_m = 0$ where the data does. One expects, therefore, that Equation (23) would assign too much of the momentum at high r values and so predict a low value for $\bar{u}/\bar{u}_m$. The mixing length formula would appear to give $\bar{u}/\bar{u}_m$ more accurately. In fact, the quite accurate error curve expression for the velocity distribution by Gaylord (24) gives

$$\bar{u}_m/u_o = 1.178\ r_o/r_c \qquad (24)$$

EXPERIMENTAL JET VELOCITY DISTRIBUTIONS FOR PURE FLUIDS

An experimental jet velocity profile is a number of local velocity measurements made on a radial traverse of the jet flow from one jet boundary to the other through the jet axis. A plot of all of these velocities is a family of velocity distributions with different shapes. From these plotted distributions the parameters, $\bar{u}_m$ and r_c are obtained. The data can then be reduced to $\bar{u}/\bar{u}_m = g(r/r_c)$ for a check of similarity and comparison with reported results for other jets. The experimental constant, σ, can be determined from z and r_c with Equation (19).

Velocity distributions for the axisymmetric submerged jet have been measured extensively in pure fluids. The results of several classic experimental jet measurements are available in the literature and others are given in fluid mechanics texts. They are not all presented in exactly the same way but when they are reduced to consistent terms there are no general discrepancies. There is considerable experimental scatter, however, in each of the published universal distributions. There is more scatter when several of these distributions are plotted together. The calculated values of σ differ by as much as 10% from one jet to another. This indicates some uncertainty in the measurement of these velocities and perhaps some unsteadiness in their values. It also suggests that not all of the ideal jet approximations are valid for any one experimental jet.

Reichardt reported his classical data as $\bar{u}^2$ against r at three values of z/d_o (25). Rouse and his coworkers gave their data in terms of an error curve formula (26). Abramovich analyzed data taken by Trupel and also a reduced version of the Reichardt measurements (23). In these published reports the experimental data were presented graphically only. The traditional investigations were in submerged air jets which are less troublesome than submerged liquid jets and more likely to be actually in unbounded space.

Three experimental studies of submerged axisymmetric water jets are available. The earliest was reported by Citrini in L'Energia Elettrica, in August 1946. He presented his data again in condensed form in a discussion of the paper by Rouse, et al. (27). The second study was a thesis dissertation by Gaylord written in 1953 (24). He described his submerged water jet in detail and all of his experimental data are available as plots of $\bar{u}/\bar{u}_m = g(r/r_c)$. He reported that the error curve expression fitted his data better than those from the other semiempirical assumptions. The third study, by Kiser, was of a water jet much like Gaylord's except that it was horizontal. Some velocity profile results were given but the data cannot be accurately transferred. The mixing length relationship fitted Kiser's data best (28).

Figure 3 gives some of the published data for the submerged water jets. Citrini reported that he took 19 different profiles on six different jets (different initial velocities from the same orifice). From his averaged experimental distribution curve he offered ten points in the form $\bar{u}/\bar{u}_m = g(r/r_c)$ (27). Gaylord made velocity profiles at five z distances (z/d_o = 9.45, 12.6, 17.5, 20.5, and 30.0) through a nozzle with d_o = 0.250 inch.

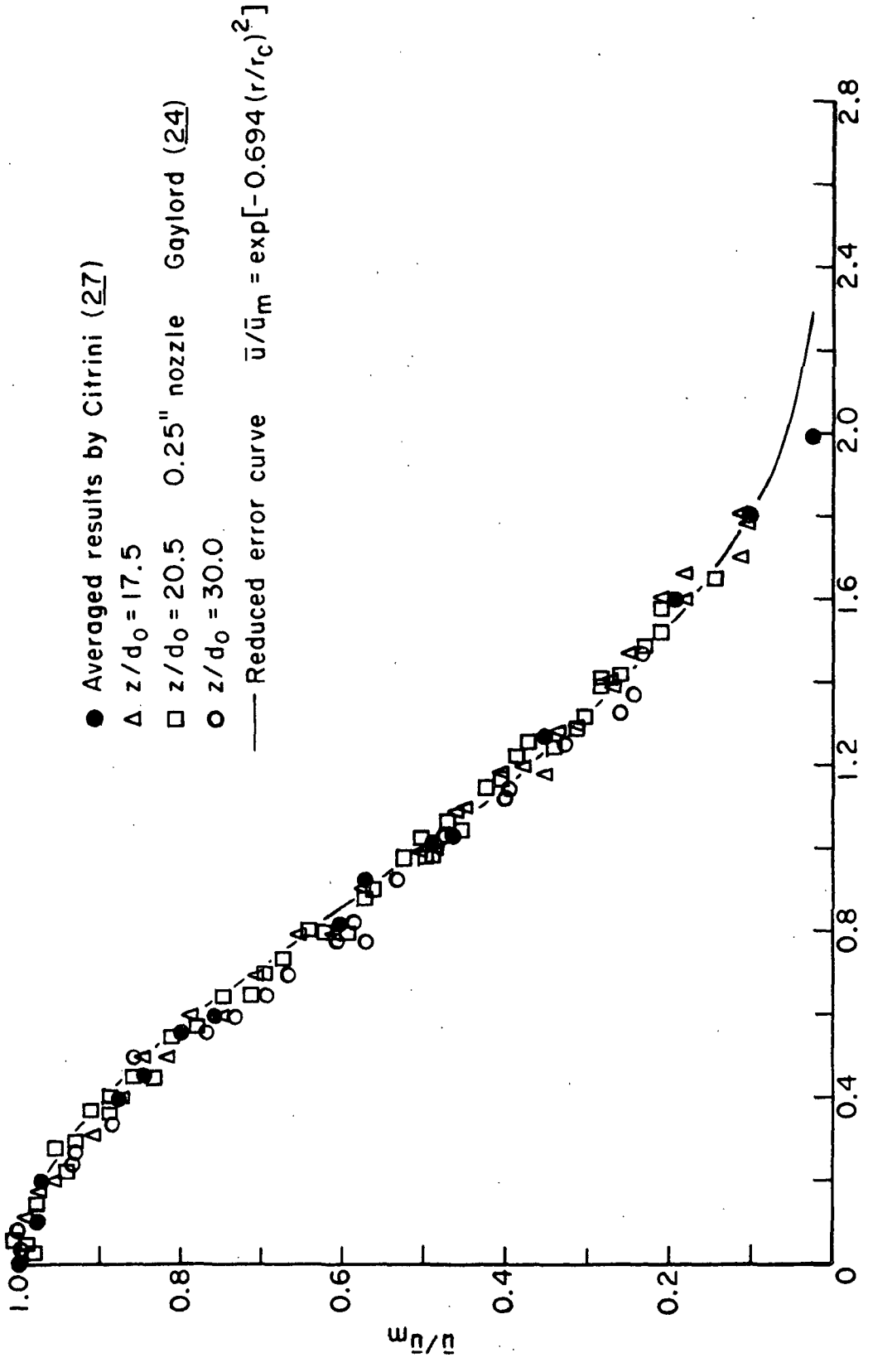

Figure 3. Experimental Water Jet Velocity Profiles

He also made two profiles through a nozzle with d_o = 0.375 inch. Points from the three of Gaylord's profiles which are farthest from the origin are shown in Fig. 3 (24). Some accuracy is likely lost in the transfer. The curve in Fig. 3 is the error curve exactly as it is drawn in Fig. 2. From the error curve and Fig. 2, it is easy to see where the two other semiempirical curves would be in relation to the data on Fig. 3. Appendix I contains similar plots of the data reported for air jets. It includes the results of Reichardt (25) and Rouse (26) along with Trupel's data from the Abramovich test (23). The profiles are not distinguishable from the water jet profiles, as expected (24).

Overall, the error curve agrees with the data as well as either of the other curves, although it does predict $\bar{u}/\bar{u}_m$ slightly high at r values less than r_c. The mixing length profile predicts $\bar{u}/\bar{u}_m$ slightly too low at low r values but it is as good as the error curve above r_c. The new Prandtl theory agrees extremely well below $r = r_c$ but predicts $\bar{u}/\bar{u}_m$ much too high at large values of r.

In the main region of the jet Gaylord found an average value of σ of about 20.0 (r_c/z = 0.091) (24). Kiser found σ = 22.5 (r_c/z = 0.0810) and said that Gaylord's value must be in error (28). Reichardt's data gave σ = 21.5 (r_c/z = 0.0848) (21,25). Abramovich calculated σ = 18.5 (r_c/z = 0.0970), from Trupel's data (23). The data presented by Rouse and coworkers lead to a value of σ = 19.1 (r_c/z = 0.0954), although they did not compute it specifically in their own analysis (26).

The value of σ should be a universal constant for any ideal pure fluid jet. From the reported results it is clear that there are possibly important differences between the various experimental jets. There is also a definite

difficulty in locating the virtual origin of the jet, which is different for each jet. The value of a is probably dependent upon the uniformity of the initial velocity distribution, its turbulence characteristics, and the nozzle radius. It is likely also affected by counterflow in a confined jet. No generally valid relationships have been found (23). It does not seem reasonable, at this point, to accept any of the values of σ as correct or to try to average them.

STATEMENT OF THE PROBLEM

Meyer's theoretical treatment of fiber suspension flow led to two-phase equations for turbulent tube flow. Solutions to the equations were in agreement with experimental results for velocity and consistency distributions. A similar treatment of a second turbulent flow system with radically different forces and boundary conditions is valuable as a confirmation of the validity of the assumptions of the two-phase approach. This analysis must be verified by experimental results.

The present study of suspension flow in the submerged jet concerns velocity and consistency distributions. No attempt is made to detect regimes of turbulence corresponding to those of pipe flow. It is expected that over most of the ranges of velocity and consistency studied the flow would correspond roughly to damped turbulence, if, in fact, damping were to occur. The questions to be answered are whether fibers affect the jet velocity distribution (by affecting momentum transport or otherwise) and whether flow conditions can create a time-mean consistency nonuniformity in the jet.

ANALYSIS OF TURBULENT FLOW OF A FIBER SUSPENSION JET

An equation for the velocity distributions in the fiber suspension jet can be derived from the general two-phase equations of Meyer (1,2,5). Although an equation for the consistency distribution has been derived, no solution has been found. Both the fiber and water phases are treated as fluid continuua so that the laws of conservation of mass and momentum can be applied to each. Although it is often interrupted by fibers in a dilute suspension, the water phase certainly is a continuum. The fiber phase, however, is at best a "quasi-continuum." Meyer noted that the assumption that the conservation laws can be applied to the fiber phase is doubtful (2).

ANALYSIS OF FIBER SUSPENSION FLOW AS A TWO-PHASE SYSTEM

Sanders and Meyer (1,2,5) described the two-phase theoretical approach for turbulent flow. The equations of continuity and motion are derived separately for each phase from mass and momentum balances on an infinitesimal volume element of suspension. The equations apply approximately to a finite element that contains many fibers (forming a fiber continuum) but is much smaller than the dimensions of the flow system (2). In effect, the equations are space-averaged over the small volume of suspension.

For a single-phase fluid the equations of continuity and motion are

$$\partial\rho/\partial t = -\nabla\cdot\rho\vec{v} \tag{25}$$

$$\partial\rho\vec{v}/\partial t + [\nabla\cdot\rho\vec{v}\vec{v}] = -\nabla\rho - [\nabla\cdot\tau] + \rho\vec{g} \tag{26}$$

The fiber-water mixture contains a fraction, ε, of the water phase and a fraction, $(1-\varepsilon)$, of the fiber phase. The porosity, ε, is the void (water) fraction of suspension area or volume. For the water phase, $\rho_\lambda = \varepsilon\rho_\Lambda$ is the

apparent density at a true water density, ρ_Λ, and $\vec{v}_\lambda$ is an average of water velocities in the finite volume element. Similarly, $\rho_\phi = (1-\varepsilon)\rho_\Phi$ is the apparent fiber density at a true fiber density, ρ_Φ, and $\vec{v}_\phi$ is the velocity of the fiber continuum in the finite volume. There is no reason to expect that both phases move with identical velocities.

For the fiber-water mixture the density, ρ, and the mass flux, $\rho\vec{v}$, are expressed as

$$\rho = \varepsilon\rho_\Lambda + (1-\varepsilon)\rho_\Phi \tag{27}$$

$$\rho\vec{v} = \varepsilon\rho_\Lambda \vec{v}_\lambda + (1-\varepsilon)\rho_\Phi \vec{v}_\phi \tag{28}$$

The resulting equations of continuity for water and fiber with ρ_Λ and ρ_Φ constant are (2):

$$\partial\varepsilon/\partial t = -\nabla\cdot\varepsilon\vec{v}_\lambda \tag{29}$$

$$\partial(1-\varepsilon)/\partial t = -\nabla\cdot(1-\varepsilon)\vec{v}_\phi \tag{30}$$

The momentum equation can be similarly transformed since

$$p = \varepsilon p_\Lambda + (1-\varepsilon)\, p_\Phi, \tag{31}$$

where p_Λ is the pressure of the water phase and p_Φ is the pressure of the fiber phase, and

$$\tau = \tau_\lambda + \tau_\phi, \tag{32}$$

where τ_λ and τ_ϕ are the apparent water and fiber stresses. When the equations are written for the separate phases of the suspension, however, it is necessary to introduce an interaction force, $\vec{F}_\lambda$, per unit volume of mixture, exerted by the water on the fibers. Emmons (4) first wrote this as

$$\vec{F}_\lambda = -\rho_\Lambda(1-\varepsilon)\vec{g} + \vec{D} + \nabla(1-\varepsilon)p_\Lambda \qquad (33)$$

The first term accounts for the buoyancy of the fibers. The term $\vec{D}$ is a drag force due to the relative motion of the two phases. Sanders and Meyer used the Darcy equation form,

$$\vec{D} = \mu a\varepsilon(\vec{v}_\lambda - \vec{v}_\phi), \qquad (34)$$

for the drag term in dilute fiber suspensions. For Darcy's law to be valid it must be assumed that the fiber is the structure forming phase of the mixture and that the relative velocity, $\vec{v}_{rel} = \vec{v}_\lambda - \vec{v}_\phi$, is small.

The third term of $\vec{F}_\lambda$ is a correction for the fibers that are partly in and partly out of the volume element used in setting up the force balances for the two phases (2,4). The buoyancy and drag terms assume that the fluid pressure acts on all surfaces of the solid. The correction is necessary because fluid pressure does not act on the "cut" fiber ends at the faces of the volume element (4).

The final form of the equations of motion for the fiber and water phases may be written:

$$\rho_\Lambda\left(\frac{\partial\varepsilon\vec{v}_\lambda}{\partial t} + [\nabla\cdot\varepsilon\vec{v}_\lambda\vec{v}_\lambda]\right) = -\nabla p_\Lambda - \nabla\cdot\tau_\lambda + \rho_\Lambda\vec{g} - \mu a\varepsilon\vec{v}_{rel} \qquad (35)$$

$$\rho_\Phi\left(\frac{\partial(1-\varepsilon)\vec{v}_\phi}{\partial t} + [\nabla\cdot(1-\varepsilon)\vec{v}_\phi\vec{v}_\phi]\right) = -\nabla(\bar{p}-\rho_\Lambda) - \nabla\cdot\tau_\phi + (\rho-\rho_\Lambda)\vec{g} + \mu a\varepsilon\vec{v}_{rel} \qquad (36)$$

ANALYSIS OF TURBULENT TWO-PHASE FLOW OF A FIBER SUSPENSION JET

Flow in the circular jet with axis in the z-direction has been described in cylindrical coordinates. The fiber and water two-phase equations (35) and (36) will be expanded in this coordinate system. When polar cylindrical

coordinates are used, consideration of the angular coordinate is unnecessary because of symmetry. In this analysis the longitudinal water velocity, $\underline{v}_{\lambda\underline{z}}$, will be written $\underline{u}_\lambda$ and the radial water velocity, $\underline{v}_{\lambda\underline{r}}$, will be written $\underline{v}_\lambda$. Because a turbulent velocity fluctuation in the angular component is expected, an angular velocity is written as $\underline{v}_{\lambda\theta} = \underline{w}_\lambda$. The $\underline{z}$- and $\underline{r}$-components of Equation (35) are

$$\rho_\Lambda \left[\frac{\partial \varepsilon u_\lambda}{\partial t} + 1/r\ \partial/\partial r\ (r\varepsilon v_\lambda u_\lambda) + \partial/\partial z\ (\varepsilon u_\lambda^2) \right] = \Sigma F_{\lambda z}, \tag{37}$$

$$\rho_\Lambda \left[\frac{\partial \varepsilon v_\lambda}{\partial t} + 1/r\ \partial/\partial r\ (r\varepsilon v_\lambda^2) + \partial/\partial z\ (\varepsilon v_\lambda u_\lambda) - \frac{\varepsilon w_\lambda^2}{r} \right] = \Sigma F_{\lambda r}, \tag{38}$$

where

$$\Sigma F_{\lambda z} = - \frac{\partial p_\Lambda}{\partial z} - \rho_\Lambda g - \frac{\partial \tau_{\lambda zz}}{\partial z} - 1/r\ \partial/\partial r\ (r\tau_{\lambda rz}) - \mu a\varepsilon(u_\lambda - u_\phi),$$

$$\Sigma F_{\lambda r} = - \frac{\partial p_\Lambda}{\partial r} - \frac{\partial \tau_{\lambda rz}}{\partial z} - 1/r\ \partial/\partial r\ (r\tau_{\lambda rr}) - \mu a\varepsilon(v_\lambda - v_\phi),$$

where $\underline{g}_{\underline{z}} = -\underline{g}$ and $\underline{g}_{\underline{r}} = 0$. Similar equations can be developed from Equation (36) for the fiber phase.

The two-phase equations of continuity, Equations (29) and (30) are treated similarly to give:

$$\partial\varepsilon/\partial t + 1/r\ \partial/\partial r\ (r\varepsilon v_\lambda) + \partial/\partial z\ (\varepsilon u_\lambda) = 0 \tag{39}$$

$$-\partial\varepsilon/\partial t + 1/r\ \partial/\partial r\ [r(1-\varepsilon)v_\phi] + \partial/\partial z\ [(1-\varepsilon)u_\phi] = 0 \tag{40}$$

For the turbulent jet analysis each turbulent variable is written as the sum of a time-mean quantity (over bar) and a fluctuating quantity (prime):

$$\begin{aligned} p &= \bar{p} + p' \\ \varepsilon &= \bar{\varepsilon} + \varepsilon' \\ u &= \bar{u} + u', \text{ etc.,} \end{aligned} \tag{41}$$

where by definition the time-mean of a fluctuating quantity is zero:

$$\overline{\varepsilon'} = 1/T \int_{t_o}^{t_o+T} \varepsilon' dt = 0, \text{ etc.} \tag{42}$$

After time-smoothing, four terms of interest for the averaged equations (37) and (39) are

$$\begin{aligned}
\overline{\varepsilon u_\lambda u_\lambda} &= \bar{\varepsilon}\,\bar{u}_\lambda\bar{u}_\lambda + \bar{\varepsilon}\,\overline{u'_\lambda u'_\lambda} + 2\,\bar{u}_\lambda\,\overline{\varepsilon' u'_\lambda} \\
\overline{\varepsilon u_\lambda v_\lambda} &= \bar{\varepsilon}\,\bar{u}_\lambda\bar{v}_\lambda + \bar{\varepsilon}\,\overline{u'_\lambda v'_\lambda} + \bar{u}_\lambda\,\overline{\varepsilon' v'_\lambda} + \bar{v}_\lambda\,\overline{\varepsilon' u'_\lambda} \\
\overline{\varepsilon u_\lambda} &= \bar{\varepsilon}\bar{u}_\lambda + \overline{\varepsilon' u'_\lambda} \\
\overline{\varepsilon v_\lambda} &= \bar{\varepsilon}\bar{v}_\lambda + \overline{\varepsilon' v'_\lambda}
\end{aligned} \tag{43}$$

Introduction of these relationships into the continuity Equation (39) and a separation into time-independent and time-dependent parts yields two equations:

$$1/r\ \partial/\partial r\ (r\bar{\varepsilon}\bar{v}_\lambda) + \partial/\partial z\ (\bar{\varepsilon}\bar{u}_\lambda) = 0 \tag{44}$$

$$\frac{\partial \varepsilon'}{\partial t} + 1/r\ \partial/\partial r\ [r(\varepsilon'\bar{v}_\lambda + \bar{\varepsilon}v'_\lambda + \varepsilon' u'_\lambda)] + \partial/\partial z\ (\varepsilon'\bar{u}_\lambda + \bar{\varepsilon}u'_\lambda + \varepsilon' u'_\lambda) = 0 \tag{45}$$

Time-smoothing of Equation (45) gives

$$1/r\ \partial/\partial r\ (r\overline{\varepsilon' v'_\lambda}) + \partial/\partial z\ (\overline{\varepsilon' u'_\lambda}) = 0 \tag{46}$$

The fiber phase equation of continuity can be treated in exactly the same way to give

$$1/r\ \partial/\partial r\ [r(1-\varepsilon)\bar{v}_\phi] + \partial/\partial z\ [(1-\varepsilon)\bar{u}_\phi] = 0 \tag{47}$$

$$1/r\ \partial/\partial r\ (r\overline{\varepsilon' v'_\phi}) + \partial/\partial z\ (\overline{\varepsilon' u'_\phi}) = 0 \tag{48}$$

Equations (44) and (47) express continuity of time-mean superficial flow and Equations (46) and (48) express continuity for the turbulent mass flux.

The equations of motion can also be written for turbulent flow, using Equation (41) and time-smoothing of the z-component of the liquid phase momentum Equation (37) leads to

$$\rho_\Lambda \left[\frac{\partial \overline{(\bar{\varepsilon}+\varepsilon')(\bar{u}_\lambda+u'_\lambda)}}{\partial t} + 1/r\ \partial/\partial r \left(\overline{r(\bar{\varepsilon}+\varepsilon')(\bar{v}_\lambda+v'_\lambda)(\bar{u}_\lambda+u'_\lambda)} \right) + \partial/\partial z \left(\overline{(\bar{\varepsilon}+\varepsilon')(\bar{u}_\lambda+u'_\lambda)^2} \right) \right] = \Sigma \bar{F}_{\lambda z} \qquad (49)$$

The viscous shear term in $\bar{F}_{\lambda z}$ is small with respect to the Reynold's stresses arising from the turbulent analysis. When it is neglected and steady-state flow is assumed:

$$\rho_\Lambda \left[\partial/\partial z\ (\bar{\varepsilon}\bar{v}_\lambda\bar{u}_\lambda + \bar{\varepsilon}\overline{u'^2_\lambda} + 2\bar{u}_\lambda\ \overline{\varepsilon' u'_\lambda}) + 1/r\ \partial/\partial r \left(r(\bar{\varepsilon}\bar{u}_\lambda\bar{v}_\lambda + \bar{\varepsilon}\overline{v'_\lambda u'_\lambda} + \bar{v}_\lambda\overline{\varepsilon' u'_\lambda} + \bar{u}_\lambda\overline{\varepsilon' v'_\lambda}) \right) \right] =$$

$$\Sigma \bar{F}_{\lambda z} = -\frac{\partial p_\Lambda}{\partial z} - \rho_\Lambda g - \overline{\mu a \varepsilon (u_\lambda - u_\phi)} \qquad (50)$$

In a similar manner, the r-component, Equation (38), can be written:

$$\rho_\Lambda \left[\partial/\partial z\ (\bar{\varepsilon}\bar{v}_\lambda\bar{u}_\lambda + \bar{\varepsilon}\overline{u'_\lambda v'_\lambda} + \bar{v}_\lambda\overline{\varepsilon' u'_\lambda} + \bar{u}_\lambda\overline{\varepsilon' v'_\lambda}) + 1/r\ \partial/\partial r \left(r(\bar{\varepsilon}\bar{v}^2_\lambda + \bar{\varepsilon}\overline{v'^2_\lambda} + 2\bar{v}_\lambda\ \overline{\varepsilon' v'_\lambda}) \right) - \frac{\bar{\varepsilon}\overline{w'^2}}{r} \right] =$$

$$\Sigma \bar{F}_{\lambda r} = \frac{\partial p_\Lambda}{\partial r} - \overline{\mu a \varepsilon (v_\lambda - v_\phi)} \qquad (51)$$

VELOCITY DISTRIBUTIONS

In jet flow mean values change faster in the radial direction than in the longitudinal direction. The usual jet assumption is that gradients of mean

values in the z-direction can be neglected in comparison to those in the r-direction. The first series of terms in Equation (51) is therefore neglected and the equation can be integrated in the form:

$$- \rho_\Lambda \overline{\varepsilon v_\lambda'^2} + \rho_\Lambda \int_r^\infty 1/r \; \partial/\partial r \left(r(\overline{\varepsilon}\overline{v}_\lambda^2 + 2\overline{v}_\lambda \overline{\varepsilon' v_\lambda'}) \right) dr +$$

$$\rho_\Lambda \int_r^\infty \frac{\overline{\varepsilon(v_\lambda'^2 - w_\lambda'^2)}}{r} + \mu \int_r^\infty a \, \overline{\varepsilon(v_\lambda - v_\phi)} dr = \overline{p}_\Lambda - \overline{p}_{\Lambda\infty} \qquad (52)$$

In pure fluid jets the term $(\overline{v_\lambda'^2} - \overline{w_\lambda'^2})$ has been shown to be equal to zero (23). This assumption is now made for the suspension jet also so that the third term of Equation (52) can be dropped. Equation (52) can be written:

$$- \rho_\Lambda \overline{\varepsilon v_\lambda'^2} - \rho_\Lambda \overline{\varepsilon}\overline{v_\lambda^2} + \rho_\Lambda \int_r^\infty \frac{\overline{\varepsilon}\overline{v_\lambda^2}}{r} dr - 2\rho_\Lambda \overline{v}_\lambda \overline{\varepsilon' v_\lambda'} +$$

$$2\rho_\Lambda \int_r^\infty \frac{\overline{v}_\lambda \overline{\varepsilon' v_\lambda'}}{r} dr + \mu \int_r^\infty a \, \overline{\varepsilon(v_\lambda - v_\phi)} dr = \overline{p}_\Lambda - \overline{p}_{\Lambda\infty} \qquad (53)$$

Townsend's data shows that $\sqrt{\overline{v'^2}}/\overline{u}_{max}$ is ten times as great as $\sqrt{\overline{v^2}}/\overline{u}_{max}$ through most of the jet (22). In Equation (53) the second term can be neglected in favor of the first. The resultant equation is differentiated with respect to z:

$$- \frac{\partial \overline{p}_\Lambda}{\partial z} = - \frac{\partial p_{\Lambda\infty}}{\partial z} + \rho_\Lambda \frac{\partial \overline{\varepsilon v_\lambda'^2}}{\partial z} - \rho_\Lambda \int_r^\infty 1/r \, \frac{\partial \overline{\varepsilon}\overline{v_\lambda^2}}{\partial z} dr + 2\rho_\Lambda \frac{\partial}{\partial z} (\overline{v}_\lambda \overline{\varepsilon' v_\lambda'}) -$$

$$2\rho_\Lambda \int_r^\infty 1/r \; \partial/\partial z \; (\overline{v}_\lambda \overline{\varepsilon' v_\lambda'}) \, dr - \mu \; \partial/\partial z \int_r^\infty a \, \overline{\varepsilon(v_\lambda - v_\Phi)} \, dr \qquad (54)$$

Because the pressure in a submerged jet is hydrostatically distributed, a simplification can be made by writing

$$- \frac{\partial \overline{p}_{\Lambda\infty}}{\partial z} - \rho_\Lambda g = 0 \qquad (55)$$

Equations (54) and (55) are substituted into the z-component water Equation (50). Since the fiber phase will not be dealt with further in this section, the subscript, λ, can be omitted with the understanding that only the water phase velocity will be dealt with.

$$\rho_\Lambda \, \partial/\partial z \,(\bar{\varepsilon}\overline{u^2} + \bar{\varepsilon}\overline{u'^2} + 2\bar{u}\overline{\varepsilon'u'}) + \frac{\rho_\Lambda}{r} \, \partial/\partial r \left(r(\bar{\varepsilon}\bar{u}\bar{v} + \bar{\varepsilon}\overline{v'u'} + \bar{v}\overline{\varepsilon'u'} + \bar{u}\overline{\varepsilon'v'}) \right) = - \mu \, a \, \overline{\varepsilon(u_\lambda - u_\phi)} + \rho_\Lambda \frac{\partial \bar{\varepsilon}\overline{v'^2}}{\partial z} + 2\rho_\Lambda \, \partial/\partial z \, (\bar{v}\overline{\varepsilon'v'}) -$$

$$\rho_\Lambda \int_r^\infty 1/r \, \frac{\partial(\bar{\varepsilon}\overline{v^2})}{\partial z} \, dr - 2\rho_\Lambda \int_r^\infty 1/r \, \partial/\partial z \, (\bar{v}\overline{\varepsilon'v'}) \, dr - \mu \, \partial/\partial z \int_r^\infty$$

$$a \, \overline{\varepsilon(v_\lambda - v_\phi)} \, dr \qquad (56)$$

Equation (56) can be rearranged to get the convective terms into a special form with squared terms in ε:

$$\partial/\partial z \, (\overline{\varepsilon^2}\,\overline{u^2} + \overline{\varepsilon^2}\,\overline{u'^2} + 2\bar{\varepsilon}\bar{u}\,\overline{\varepsilon'u'}) + 1/r \, \partial/\partial r \left(r(\overline{\varepsilon^2}\,\bar{u}\bar{v} + \overline{\varepsilon^2}\,\overline{u'v'} + \bar{\varepsilon}\bar{v}\,\overline{\varepsilon'u'} + \bar{\varepsilon}\bar{u}\,\overline{\varepsilon'v'}) \right) = - \mu\bar{\varepsilon}/\rho_\Lambda \, a \, \overline{\varepsilon(u_\lambda - u_\phi)} + \bar{\varepsilon} \, \partial\bar{\varepsilon}\,\overline{v'^2}/\partial z + 2\bar{\varepsilon}(\bar{v}\overline{\varepsilon'v'}) -$$

$$\bar{\varepsilon} \int_r^\infty 1/r \, \frac{\partial(\bar{\varepsilon}\,\overline{v^2})}{\partial z} \, dr - 2\bar{\varepsilon} \int_r^\infty 1/r \, \partial/\partial z \, (\bar{v}\,\overline{\varepsilon'v'}) \, dr -$$

$$\mu\varepsilon/\rho_\Lambda \, \partial/\partial z \int_r^\infty a \, \overline{\varepsilon(v_\lambda - v_\phi)} \, dr + (\bar{\varepsilon}\,\overline{u^2} + \bar{\varepsilon}\,\overline{u'^2} + 2\bar{u}\,\overline{\varepsilon'u'}) \frac{\partial\bar{\varepsilon}}{\partial z} +$$

$$(\bar{\varepsilon}\bar{u}\bar{v} + \bar{\varepsilon}\,\overline{u'v'} + \bar{v}\,\overline{\varepsilon'u'} + \bar{u}\,\overline{\varepsilon'v'}) \frac{\partial\bar{\varepsilon}}{\partial r} = R \qquad (57)$$

The velocity arguments of the convective terms of Equation (57) can be generated by starting from the expression

$$U = \bar{\varepsilon}(\bar{u}+u') + \overline{\varepsilon'u'}, \qquad (58)$$

which is squared to give

$$U^2 = \overline{\varepsilon}^2(\overline{u}^2 + 2\overline{u}u' + u'^2) + 2\overline{\varepsilon}(\overline{u}+u')\overline{\varepsilon'u'} + \overline{\varepsilon'u'}^2 \qquad (59)$$

After time-smoothing the square of the superficial turbulent velocity is obtained:

$$\overline{U}^2 = U^{*2} = \overline{\varepsilon}^2\,\overline{u}^2 + \overline{\varepsilon}^2\,\overline{u'^2} + 2\overline{\varepsilon}\overline{u}\,\overline{\varepsilon'u'} + \overline{\varepsilon'u'}^2 \qquad (60)$$

This is identical to the first velocity argument in Equation (57) if the term $\overline{\varepsilon'u'}^2$ is neglected as a small term of second order.

Similarly the expression

$$V = \overline{\varepsilon}(\overline{v}+v') + \overline{\varepsilon'v'} \qquad (61)$$

is combined with Equation (58) to give

$$UV = \overline{\varepsilon}^2(\overline{u}\overline{v} + \overline{u}v' + \overline{v}u' + \overline{u'v'}) + \overline{\varepsilon}(\overline{u}+u')\overline{\varepsilon'v'} + \overline{\varepsilon}(\overline{v}+v')\overline{\varepsilon'u'} + (\overline{\varepsilon'u'})(\overline{\varepsilon'v'}) \qquad (62)$$

Time-smoothing gives the result

$$\overline{UV} = \overline{\varepsilon}^2\overline{u}\overline{v} + \overline{\varepsilon^2\,u'v'} + \overline{\varepsilon}\overline{u}\,\overline{\varepsilon'v'} + \overline{\varepsilon}\overline{v}\,\overline{\varepsilon'u'} + (\overline{\varepsilon'u'})(\overline{\varepsilon'v'}) \qquad (63)$$

Again, the second order term, $(\overline{\varepsilon'u'})(\overline{\varepsilon'v'})$, is neglected and Equation (63) becomes identical to the second convective term of Equation (57). Finally, $\underline{\overline{U}}$ and $\underline{\overline{UV}}$ are introduced into Equation (57) to give

$$\partial/\partial z\ \overline{U^2} + 1/r\ \partial/\partial r\,(r\overline{UV}) = R \qquad (64)$$

The terms in $\underline{R}$ can be separated into three groups. The first consists of five terms involving the $\underline{z}$-direction derivatives of either $\overline{\underline{v}'^2}$, $\underline{\overline{v}}\,\overline{\varepsilon'\underline{v}'}$, $\underline{\overline{v}}^2$, or $\overline{\underline{v}_\lambda \underline{v}_\phi}$. Since all of these variables are small compared to $\underline{\overline{U}}^2$ their derivatives are small compared to $\partial/\partial z\ \underline{\overline{U}}^2$ and the entire group of five terms may be dropped.

Another group of two terms depends directly on $\partial\bar{\varepsilon}/\partial r$ and $\partial\bar{\varepsilon}/\partial z$. The final term is the time-mean drag term. A special case would exist where the fibers remain uniformly distributed. Equation (64) then would reduce approximately to

$$\partial/\partial z\ \overline{U^2} + 1/r\ \partial/\partial r\ r\overline{UV} = \frac{-\mu\varepsilon}{\rho_\Lambda}\ a\ \overline{\varepsilon(v_\lambda - v_\phi)} \tag{65}$$

There is no obvious reason why $\bar{v}_\lambda = \bar{v}_\phi$, which would make the drag term vanish also. In a case where the fibers and water did move with equal velocities, however, Equation (65) could be reduced further to

$$\partial/\partial z\ \overline{U^2} + 1/r\ \partial/\partial r\ (r\overline{UV}) = 0 \tag{66}$$

This equation is similar to the jet momentum equation,

$$\partial/\partial z\ \bar{u}^2 + 1/r\ \partial/\partial r\ (r\bar{u}\bar{v}) = 0, \tag{67}$$

for which Reichardt developed a solution for the pure fluid jet (25).

Following Reichardt's treatment of Equation (67), Equation (64) can be transformed into an inhomogeneous differential equation for $\overline{U^2}$. Using Reichardt's assumption of turbulent mixing leads to

$$\overline{UV} = -\mathcal{L}(z+a)\quad \partial\overline{U^2}/\partial r \tag{68}$$

The parameter $\mathcal{L}$ has the dimensions of length and is analogous to Prandtl's mixing length. Substituting Equation (68) into Equation (64) yields

$$\partial/\partial z\ (\overline{U^2}) = (\mathcal{L}/r)[\partial/\partial r\ (r\ \partial/\partial r\ \overline{U^2})] + R \tag{69}$$

The nondimensional variable, η, is introduced into the analysis, and the function, $f(\eta)$, is defined as

$$\overline{U^2} = m_o^2 u_o^2 [d_o/(z+a)]^2 \, f(\eta), \quad \eta = r/(z+a) \tag{70}$$

The squared factor is chosen after consideration of Equation (6), where m_o is an experimental constant independent of z and ε for a given jet.

Equation (69) then becomes a differential equation for $f(\eta)$

$$\mathcal{K}/(z+a)(\eta f^1)^1 + (\eta^2 f)^1 = \frac{-(z+a)^3}{m_o^2 d_o^2 u_o^2} \eta R \tag{71}$$

Assumptions about the form of $\mathcal{K}(z+a)$ and the existence of R are best left until the form of the experimental suspension velocity distribution is known.

CONSISTENCY DISTRIBUTIONS

An attempt to derive an equation for the time-mean fiber distribution would begin with Equations (44), (46)-(48). They can be rewritten in terms of $\bar{c} = 1-\varepsilon$, the volume fraction of fiber, as

$$-[1/r \, \partial/\partial r \, (r\bar{c}\bar{v}_\lambda) + \partial/\partial z \, (\bar{c}\bar{u}_\lambda)] + 1/r \, \partial/\partial r \, (r\bar{v}_\lambda) + \partial/\partial z \, (\bar{u}_\lambda) = 0 \tag{72}$$

$$1/r \, \partial/\partial r \, (r \, \overline{c'v'_\lambda}) + \partial/\partial z \, (\overline{c'u'_\lambda}) = 0 \tag{73}$$

$$1/r \, \partial/\partial r \, (r \, \bar{c}\bar{v}_\phi) + \partial/\partial z \, (r \, \bar{c}\bar{v}_\phi) = 0 \tag{74}$$

$$1/r \, \partial/\partial r \, (r \, \overline{c'v'_\phi}) + \partial/\partial z \, (\overline{c'u'_\phi}) = 0 \tag{75}$$

Use of either Equation (72) or (74) with the appropriate equation of motion forms a system of two equations with these unknowns. Sanders' flow geometry enabled him to simplify Equation (73) to a single term; he then used a mixing length substitution for $\overline{c'u'_\lambda}$. In the jet both terms of Equations (73) and (75) must be retained. No solution has been found for the consistency distribution in the submerged suspension jet.

EXPERIMENTAL EQUIPMENT AND PROCEDURES

The experimental investigation of the suspension jet required two different measurements. A purged impact tube traversing the width of the flow, together with a static pressure tube outside of the flow region, measured local time-mean impact pressures. The impact pressure distribution is related by the Bernoulli equation to the distribution of local time-mean velocities across the jet. A purged optical reflectance probe traversing the flow (at the same axial distances as did the impact tube) measured the corresponding distribution of local time-mean consistencies. A confined jet flow system filled with the fiber suspension served as a measuring chamber.

JET FLOW SYSTEM

The experimental jet emerged through a nozzle into a large tank that formed one part of a continuous flow system (Fig. 4). The major flow loop elements were

(1) the jet tank,

(2) the probe traversing mechanism, and

(3) the jet nozzle.

Auxilliary elements of the flow loop were the suspension mixing tank, the pump and drive motor, the magnetic flowmeter, and the associated valves and piping connecting the elements.

JET TANK

The jet tank (Fig. 5) was an upright cylindrical steel vessel; its top was an open surface and its bottom a circular sheet of Plexiglas. The transparent baseplate permitted visual detection of fibers settling to the bottom of the tank. It was covered to prevent room light interference during the optical consistency measurements.

A. Jet tank; painted steel, 3.05-m high and 1.16 m in diameter

B. Jet nozzle; polyvinylchloride (PVC), orifice diameter, 2.27 cm

C. Overflow trough, 13-cm deep and 8-cm wide

D. Baseplate; Plexiglas, 1-inch thick

E. Jabsco Model 3200-01, 2-inch ball bearing rotary pump; driven through a speed selector variable speed drive (no. 409-510) at 267-2400 rpm by a 3-hp, 1150 rpm, NEMA frame 215, squirrel cage motor

F. Two-inch brass gate valves

G. Drain plug

H. Two-inch brass check valve

I. Two-inch PVC ball valves

J. Foxboro Dynalog magnetic flowmeter, 2-inches

K. Suspension mixing tank; stainless steel

L. Hills-McCanna diaphragm valve, 1 and 1½-inches

The 6-m dropleg is 2-inch galvanized steel. The rest of the loop piping is 2-inch Schedule 80 PVC.

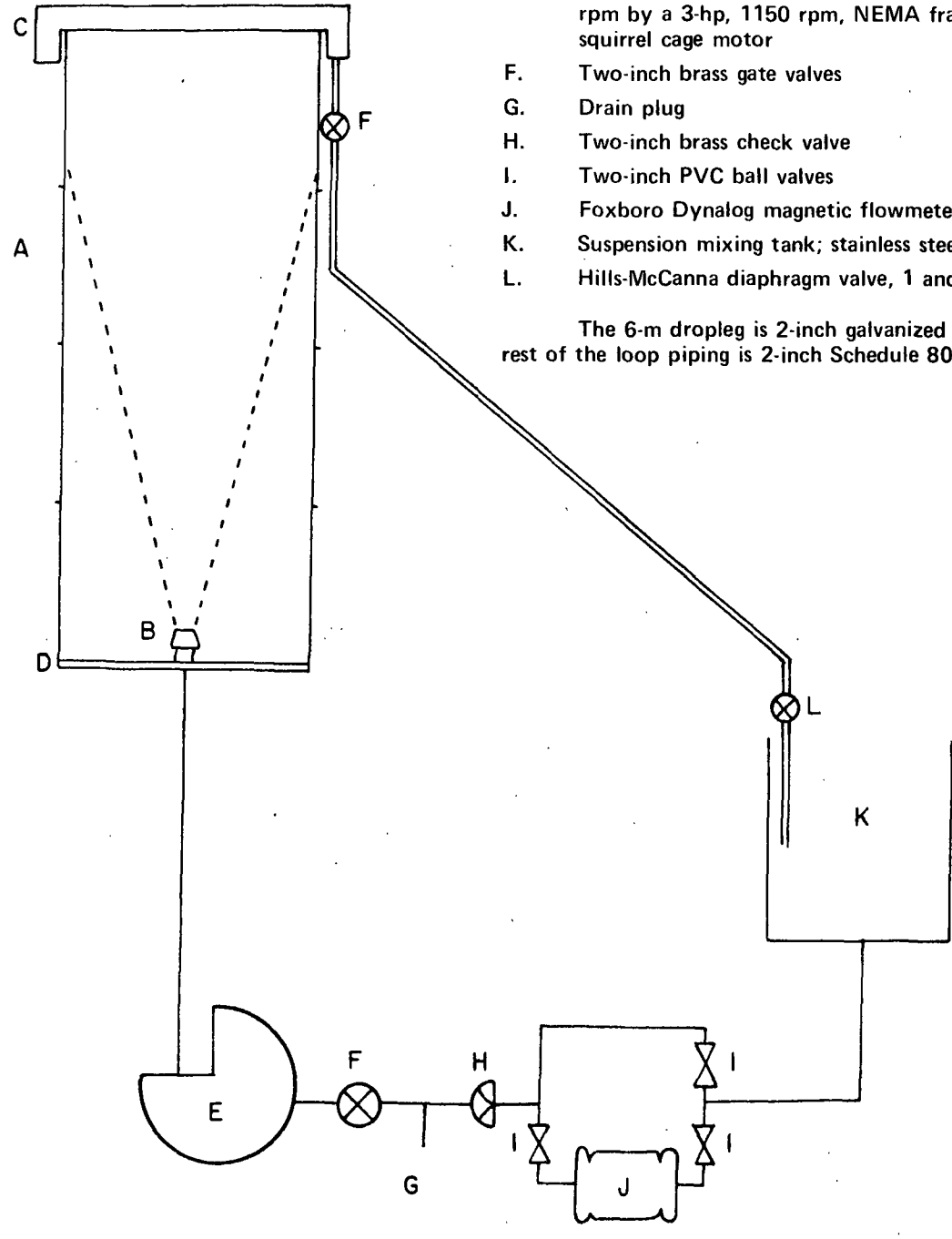

Figure 4. Jet Tank Flow System

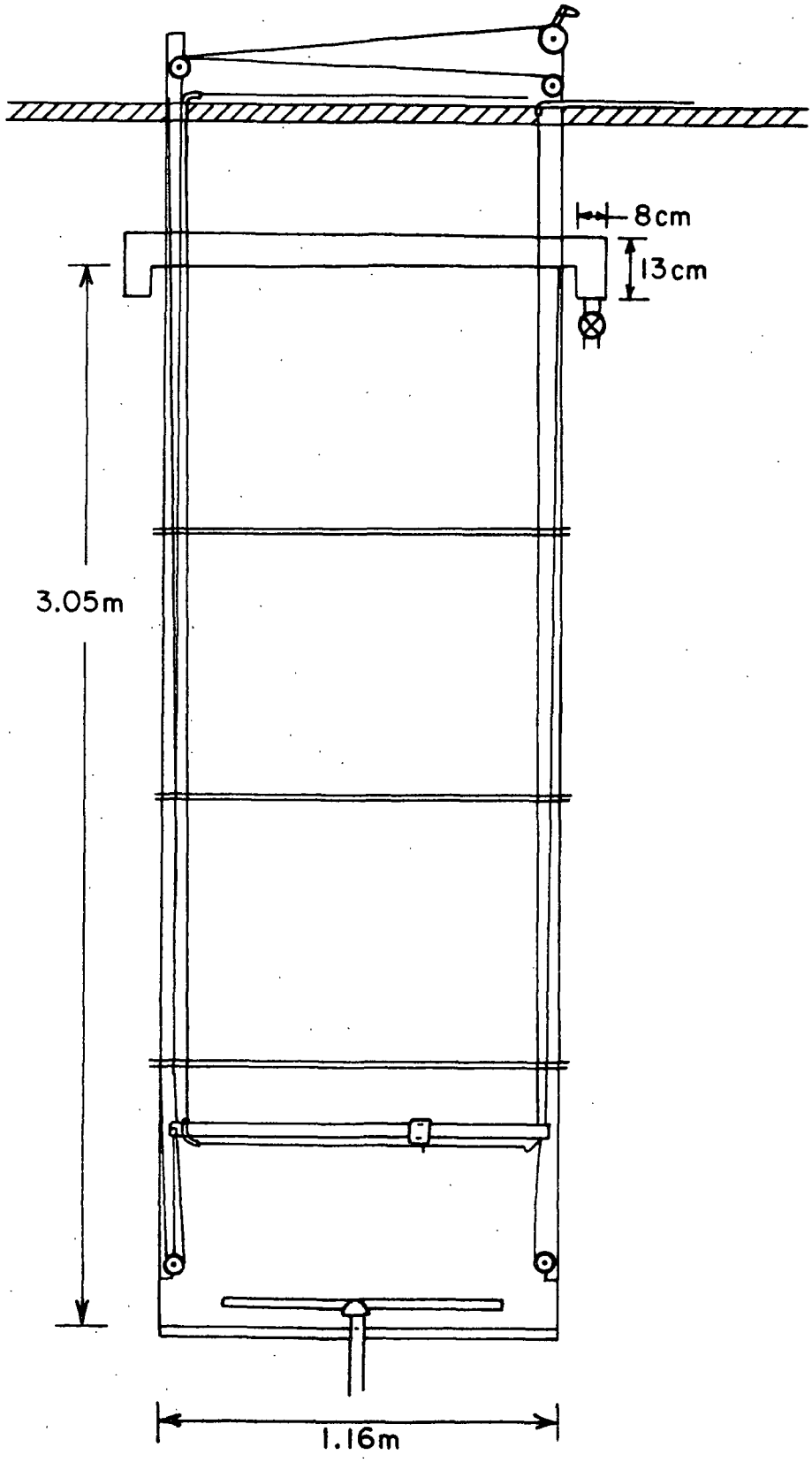

Figure 5. Jet Tank and Probe Traversing Mechanism

The flow in the tank was vertically upward from a nozzle located in the center of the Plexiglas baseplate into an overflow trough around the top of the tank (see Fig. 5). A 2-inch dropleg carried the overflow down to the mixing tank. A rubber diaphragm valve in the dropleg just above the mixing tank controlled the suspension surface level in the jet tank. The control of the surface level was critical; the trough had to be run as full as possible. If the surface level fell too low, a constant consistency suspension did not flow into the dropleg, and, if the trough became nearly empty, air was pulled into the suspension and attached to the fibers. If the surface rose too high, it was free to spill out of the tank. Because the control valve had to be nearly closed to keep the surface at its proper level, it did not throttle well. Constant attention and adjustment of the valve were needed; the tank could not be left running unattended.

PROBE TRAVERSING MECHANISM

A rigid support mechanism held either the velocity or consistency probe in the suspension flow at a known position. The support mechanism permitted the probe to traverse the width of the jet on a line perpendicular to the jet axis at any distance above the nozzle orifice (Fig. 5).

Each probe could be fixed (one at a time) to a brass plate that was, in turn, fastened to a 2-piece plastic block (Fig. 6). The block fitted around and slid horizontally on a rectangular brass bar that was perpendicular to but did not intersect the jet axis. The bar itself slid vertically on aluminum angle guides bolted to the side of the tank. These guides were positioned off of a radial line through the jet axis so that the probe tips themselves traversed exactly on that line. Cables operated from above the tank pulled the probe support block from side to side. Another pulley and cable system raised and lowered the support bar (see Fig. 5 and Appendix II, Fig. 37).

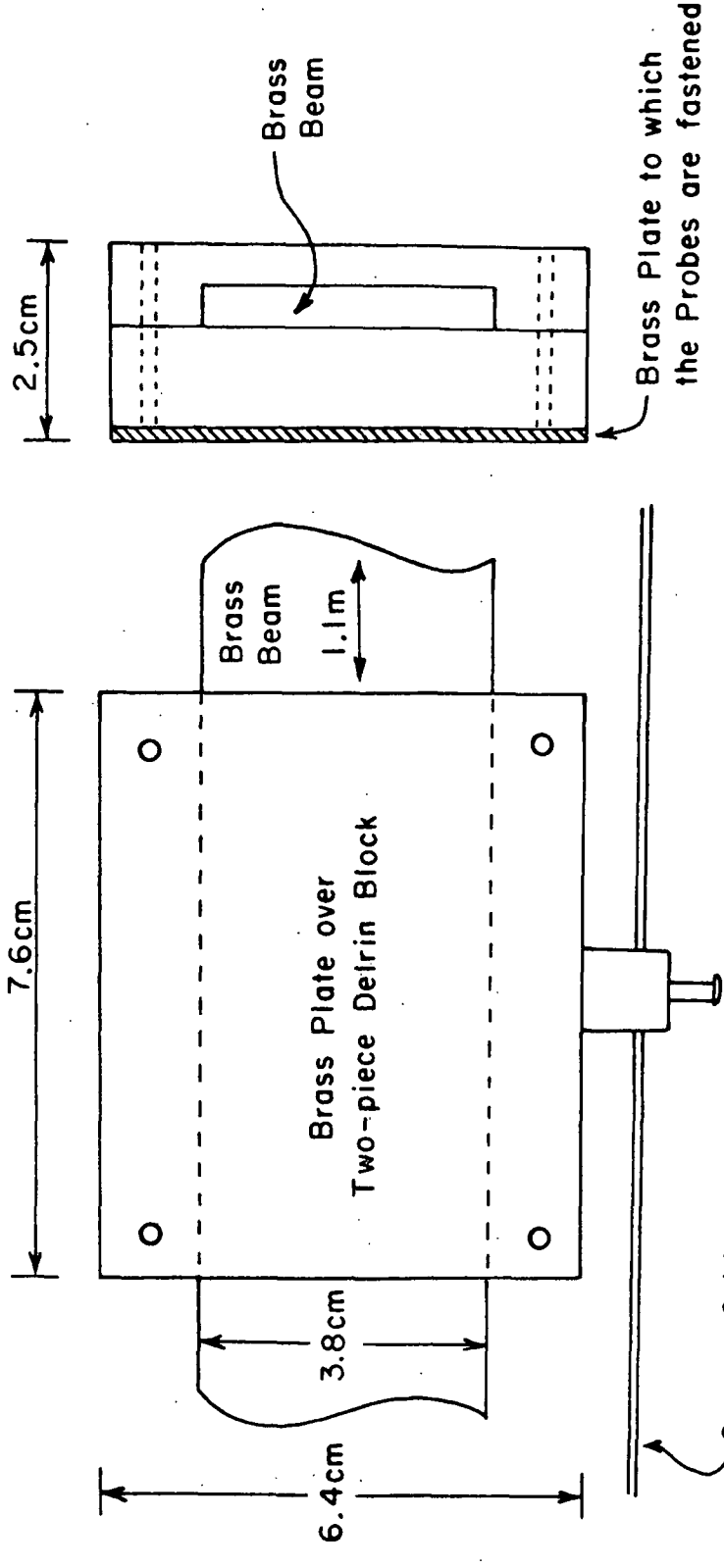

Figure 6. Probe Plate Support Block

The relative position of the probe tip was measured from above the tank. The copper cables were taut and did not stretch when the block or bar was moved. A marker fastened to the horizontal length of cable moved across a meter stick as the block slid horizontally; a similar marker moved across a second meter stick when the support bar moved vertically.

JET NOZZLE

The suspension jet nozzle in the jet flow tank was intended to provide approximately uniform velocity and consistency profiles at $z = 0$. The nozzle orifice was about 15 cm above the Plexiglas baseplate. A second circular Plexiglas sheet served as a flat wall around the nozzle in an attempt to improve the jet flow pattern. The end of the nozzle was flush with this Plexiglas surface through a hole in the center of the sheet. The smooth pipe leading up from the pump to the nozzle produced developed, symmetric, nonuniform profiles of velocity and consistency. The nozzle somewhat reduced the nonuniformity without introducing any asymmetry. The shape of the nozzle, which was cut from a short, cylindrical piece of polyvinylchloride (PVC) rod, was that of the Tsien nozzle described by Carrasquilla. He used the nozzle to calibrate an impact probe in a suspension of buoyant particles and reported that the nozzle "greatly reduces the boundary layer thickness and gives a uniform velocity profile across most of the nozzle throat (31)." The contraction of the nozzle probably also mixed the fibers enough to reduce the consistency nonuniformity in the approach pipe. Details of the shape of the nozzle are in Appendix II.

The nozzle reduced the flow diameter from 5.10 to 2.27 cm. The large nozzle throat diameter was desirable because of the length of the nylon fibers that were used in this study.

AUXILLIARY ELEMENTS

The main dropleg from the overflow trough on the jet tank emptied into a smaller open-surface vessel. This tank was used to mix the fiber into, and remove fiber from, the suspension. It also served as a reservoir for the pump. The tank is cylindrical with a radius of 0.455 m and an area of 0.65 sq m. The total volume of suspension in the jet flow system at any one time depended on the variable suspension level in this mixing tank.

The suspension flowed from the mixing tank through a 2-inch Foxboro Dynalog magnetic flowmeter. Seely (15) and Sanders (5) calibrated the meter and it was rechecked regularly by pumping out of the calibrated mixing tank into an empty jet tank.

The Jabsco Model 3200-01 rotary pump could be driven through a Speed Selector variable speed system (No. 409-510) at 267 to 2400 rpm by a 3-hp, 1150-rpm motor. There was no throttle valve on the discharge side of the pump so the flow rate never dropped below the minimum pump discharge rate of about 5×10^{-2} ft^3/sec. The corresponding minimum Reynolds number in the 2-inch pipe was about 0.85×10^4. The minimum jet Reynolds number, based on the nozzle orifice diameter, was then about 4.3×10^4.

A brass check valve and a brass gate valve between the flowmeter and the pump prevented backflow when the pump was not running. Three PVC ball valves were used in the flowmeter by-pass loop. The piping from the mixing tank through the pump to the nozzle was 2-inch PVC; the main dropleg into the mixing tank was 2-inch galvanized steel.

The total volume of suspension in the system was determined by measuring the depth of suspension in the mixing tank when the jet tank was full and the

pump off. If $\underline{h}$ were than depth measured in meters:

$$\text{volume} = 3.199 + 0.650\ \underline{h} \qquad (m^3)$$

VELOCITY MEASUREMENTS

The local time-mean velocities in the axisymmetric submerged jet were measured with an annular purge impact tube. The annular purge impact probe is a conventional impact pressure tube within a slightly larger tube that forms an annular purge jacket. Purge water flows out of this jacket around the impact tube into the oncoming suspension flow. The velocity measurements were all made within 55 cm of the nozzle orifice, within the lower quarter of the jet tank. The rest of the tank volume served as a stilling chamber. The mean velocities in the measuring region ranged from 0 to 300 cm/sec. The total width of the region of mean velocity variation was less than 20 cm at a distance of 55 cm from the nozzle.

The impact tube was water-filled and connected to a pressure measuring instrument. The time-mean pressure at the probe tip is related to the time-mean velocity through the approximate Bernoulli equation:

$$\Delta\bar{p} = \bar{p}_s - \bar{p}_\Lambda = \rho_\Lambda\, \overline{u^2}/2 \approx \rho_\Lambda/2\ (\overline{u^2}+\overline{u'^2}), \qquad (76)$$

where $\bar{p}_s$ is the mean stagnation pressure at the probe tip, and $\bar{p}_\Lambda$ is the static pressure at the same point. In the submerged jet this was the hydrostatic pressure measured at a point outside of the jet region for accuracy (30). The mean pressure difference, $\Delta\bar{p}$, was measured by a PACE magnetic reluctance differential pressure transducer.

The experimental velocity measurements in the jet tank, which should have been routine, were particularly difficult. The annular purge impact tube

worked as previously described (5,11,14) and in itself was apparently not a problem. The stagnation pressure sensed by the probe, however, fluctuated at an extremely low frequency, both in water and in fiber suspensions. The period of the oscillation was between five and ten minutes and its magnitude was 10-40% of the mean $\Delta\bar{p}$. The only place in the jet pattern where a steady signal was observed was in the core of the jet mixing region a few centimeters above the nozzle. The steady signal here showed that the unsteadiness was not produced by small vibrations of the support bar or by the pressure measuring system. An investigation revealed only that the probable cause of the impact pressure unsteadiness was a slow wandering (a lack of constant direction) of the jet flow stream. This slow motion was probably caused by a slight unsteadiness in the extremely large, slow, counterflow loops along the walls of the jet flow tank. This unsteadiness could have caused a slow movement of the entire central jet with respect to the fixed dynamic pressure probe. A movement of 1 to 2 mm would be large enough to cause effects of the observed magnitude. In his doctoral thesis, Gaylord noted of his experimental, confined, water jet:

> "To prevent whipping or oscillations of the jet axis a 2-1/2 ft diameter cylindrical screen 3-ft high was placed in the tank to damp out disturbances caused by the recirculating flow (24)."

These recirculation loops are inevitable in the confined volume of the submerged liquid jet tank. They would not exist in the unconfined jet. No other investigators have reported similar problems in the available literature. Gaylord did not say how his screen was constructed or whether it actually did work. I have not been able to obtain this information.

A screen such as the one Gaylord probably used cannot be used in a fiber suspension flow. An attempt was made to reduce the unsteadiness by building

an analogous structure from lengths of 1/2-inch polyethylene tubing. Two semicylindrical "screens" were fashioned by threading the tubing through holes drilled in vertical lengths of 3/4-inch PVC pipe. The resulting structure was 1.2-m high and 0.75 m in diameter. The tubing was spaced to give the screen approximately 50% porosity. Although it produced only a small reduction in the unsteadiness, it was kept as a permanent structure in the jet tank. The nozzle baseplate was connected to the screen structure. It, too, was intended to reduce the nonideality of the confined jet. A detailed drawing of the screen structure is in Appendix II.

The final mean velocity measurements were made as accurately as possible in spite of the unconquered oscillations. Remarkedly good velocity profiles were obtained from the recorded impact pressure signals by drawing a smooth curve along the fluctuating signal trace and visually determining the mean level.

IMPACT PROBE

Since Daily and Bugliarello first reported measurements of local time-mean suspension velocities with modified impact pressure tubes (9), the technique has been extensively used and improved (5,11,14). The measuring tip of the velocity (and consistency) probe was of a size that snags fibers and bundles of fibers when held directly into an oncoming fiber suspension flow. Experience has shown that the probe tips must be clear to give accurate readings, so the probes have required a fiber purging feature.

A purge system should prevent contact between fibers and the probe tip without affecting the measurement of suspension velocity in the vicinity of the tip. Flushing water streams across or around the tip can approximate this ideal. Although it certainly dilutes the suspension and creates a

complex and poorly defined flow pattern in the measuring volume, the annular purge jacket system apparently permits accurate measurements with the impact probe.

Mih and Parker (11) and Sanders (5) obtained the best results with the impact tube extended slightly (1 mm) beyond the end of the purge jacket. They reported that the purge water velocity does not affect the impact pressure reading over a certain range, depending on the suspension velocity. When the purge was too low, however, fiber interference or stapling occurs, reducing the pressure reading. If the purge flow was too high, it formed a water barrier over the tip and the pressure reading dropped to a negative value (11,14).

The annular purge impact probe used in the present study is shown in place on the probe support block in Fig. 7. This probe was similar to the one Sanders described in detail (5) but was over twice as long. The probe was lengthened to 12 cm to reduce the anticipated interference of the flow disturbance caused by the bar and probe support block. There were slotted spacers cut from solder drops between the impact tube and the brass purge jacket. The spacers were found to be necessary to hold the impact tube in the center of the jacket for a symmetrical purge water flow that permitted a smooth, accurate, impact pressure signal. The tip of the impact probe protruded 1 mm beyond the end of the purge jacket. The end of the purge jacket was rounded to eliminate sharp edges and create a more streamlined flow.

The probe was checked by measuring the jet velocity profiles in water with and without purge water flow. The good agreement of these results with those reported in the literature justified the use of the probe and pressure

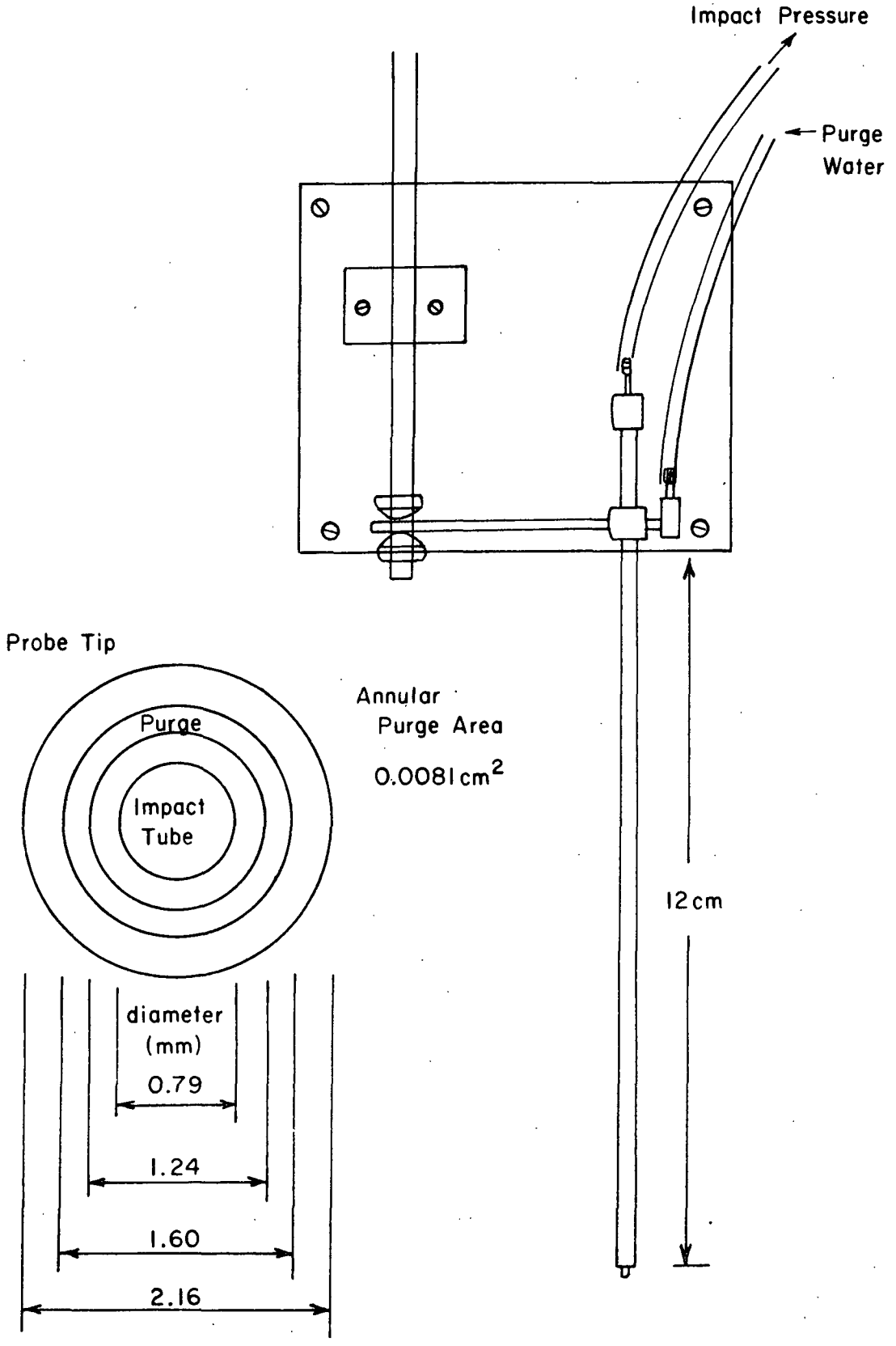

Figure 7. Impact Tube on Brass Plate

measuring system in the turbulent jet. The impact pressure signal responded to purge water flow changes substantially as described by Mih and Parker (11) and by Seely (14).

The probe was checked in water flow both in the jet tank and in a small consistency calibration loop that is described in a later section. The probe behaved in an identical fashion in each flow system. In water the measured impact pressure was not dependent on the purge water velocity until the purge velocity reached a value between 1.5 and 2.0 times the oncoming water flow velocity. The pressure signal then dropped. At low velocities of purge (and of main flow) there was an abrupt drop of the impact pressure to a negative value when the purge flow was too high. At higher absolute velocities this dropoff when the purge was too high was gradual and the signal was unsteady. The abrupt changes in the pressure reading to a steady and negative value showed that an unbroken purge jet had formed over the probe tip completely. The gradual, unsteady, decrease with increasing flow beyond the critical point at high velocities probably meant that this purge jet was unstable.

The probe has also been checked in suspension flow both in the main jet flow and in the calibration loop. The only difference between its behavior in suspension flow and in water flow was that the impact pressure signal was low at low purge rates, as expected, because of fiber stapling or interference at the probe tip. A purge velocity "plateau" existed over which range the pressure measurements had to be taken. The check of the probe in the calibration loop showed that this plateau impact pressure value was equal to the impact pressure measured by the probe in water at the same flow rate. Curves showing the purge velocity — flow velocity relationship in water and in suspension flow are in Appendix III.

IMPACT PRESSURE MEASUREMENT

A static pressure sensing tube fixed to the end of the probe support bar was connected through clear instrument tubing to the differential pressure indicating instrument (Fig. 8). Because the top surface of the tank was level and at a constant (atmospheric) pressure and because the static pressure tubing was water-filled, the vertical position of the static tube in the tank actually made no difference. It could have been anywhere below the liquid surface where the mean velocities and turbulent pressure fluctuations were negligible.

The impact tube was connected by water-filled tubing through an Ashcroft pulsation damper to the other side of the differential pressure instrument. Both impact and static lines were connected to Lucite air traps before they reached the differential pressure instrument (Fig. 8).

A CCl_4-water differential manometer was used to measure the impact pressure for several series of velocity profiles in water. The slow impact pressure oscillations made the manometer impossible to read accurately in a reasonable length of time. Observation of the manometer meniscus drifting over its range for twenty to thirty minutes permitted the estimation of an uncertain average value of a single point on the profile. Eight hours of constant observation produced a profile of uncertain average values that did agree fairly well with the published jet curve data.

The manometer was replaced with a PACE continuously recording differential pressure transducer. The amplified differential pressure signal had to be calibrated in pressure terms. The calibration was repeated several times during a run to insure that air leaks were not developing in the pressure measuring system. (Since the measuring instrumentation was above the top

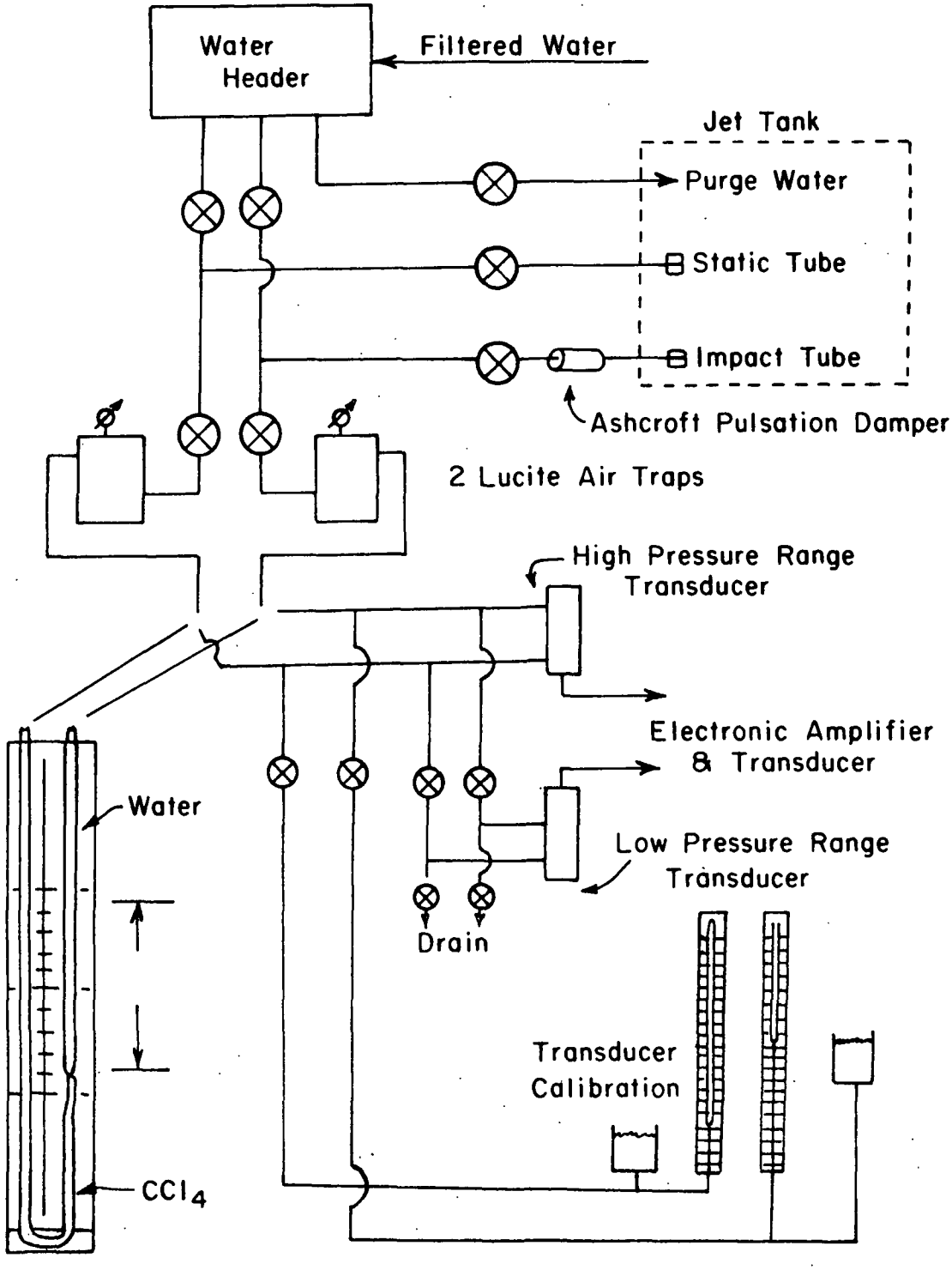

Figure 8. Pressure Instrumentation

surface of the tank, the pressures actually measured were both less than atmospheric.) The calibration standards were two static columns of water; the pressure was reported in centimeters of water. Two different transducers were used. One covered the full range from zero to 315 cm/sec; the other had a range of from zero to 150 cm/sec for greater accuracy at low velocities.

The $\Delta\bar{p}$ values from the transducer indicators were read from an Esterline Angus chart recorder connected through an RC high frequency filter to the PACE amplifier-indicator. Each local impact pressure point was recorded for between fifteen and thirty minutes depending on the steadiness of the signal so that a profile took eight to ten hours. From the chart recording a reliable average could be determined. To insure that the purge water velocity was within the plateau range, two purge water flow rates were used during the measurements of each point in a velocity profile.

CONSISTENCY MEASUREMENTS

The local time-mean consistencies in the axisymmetric submerged jet were measured with an annular purge two-branch light guide. The consistency measurements were made at the same axial distances as were the local time-mean velocity measurements. Since the velocity measurements were made first, the consistency measurements were made across a known velocity distribution.

The intensity of light reflected from a fiber suspension and returned through the light guide is a function of the suspension consistency when fiber properties and other suspension properties are constant. Before consistency measurements can be made, however, an independent determination must be made of a calibration curve giving consistency as a function of the reflected light signal. A separate flow system was built for this calibration study.

OPTICAL PROBE

Sanders was the first to use an optical probe to measure local time-mean consistency as well as velocity (5). The optical probe measured the light reflected from the fibers in a small volume of the flowing suspension. The annular purge optical probe that he described in detail was a two-branch glass fiber optics light guide surrounded by an annular purge jacket (5).

The heart of the annular purge optical probe was a two-branch fiber optics light guide (Fig. 9). The ends of two optical fiber bundles were mixed together to form a common end in which the individual fiber ends were randomly distributed. A stainless steel casing held this common end together; the ends of the glass fibers were coated with epoxy resin and polished. The other end of each of the two branches was also clad in a smaller stainless steel cap, resin coated and polished. The remaining length of each branch was sheathed in PVC between the capped ends; it was reasonably flexible but still extremely fragile, especially where the covering changed from PVC to steel.

There were approximately 525 individual, 3.5-m long glass fibers in the light guide. A single fiber diameter was about 0.1 mm. This light guide, built by the American Optical Corporation, was similar to the one Sanders described, except that at the common end the fibers were randomly distributed and the total length was much greater.

To form the optical consistency probe the stainless steel clad common end of the light guide was enclosed in a brass annular purge jacket, as shown in Fig. 10. This jacket was the one used by Sanders (5), modified so that the purge water entered from one side only. The light guide tip protruded slightly (less than 0.5 mm) from the end of the purge jacket. As in the impact

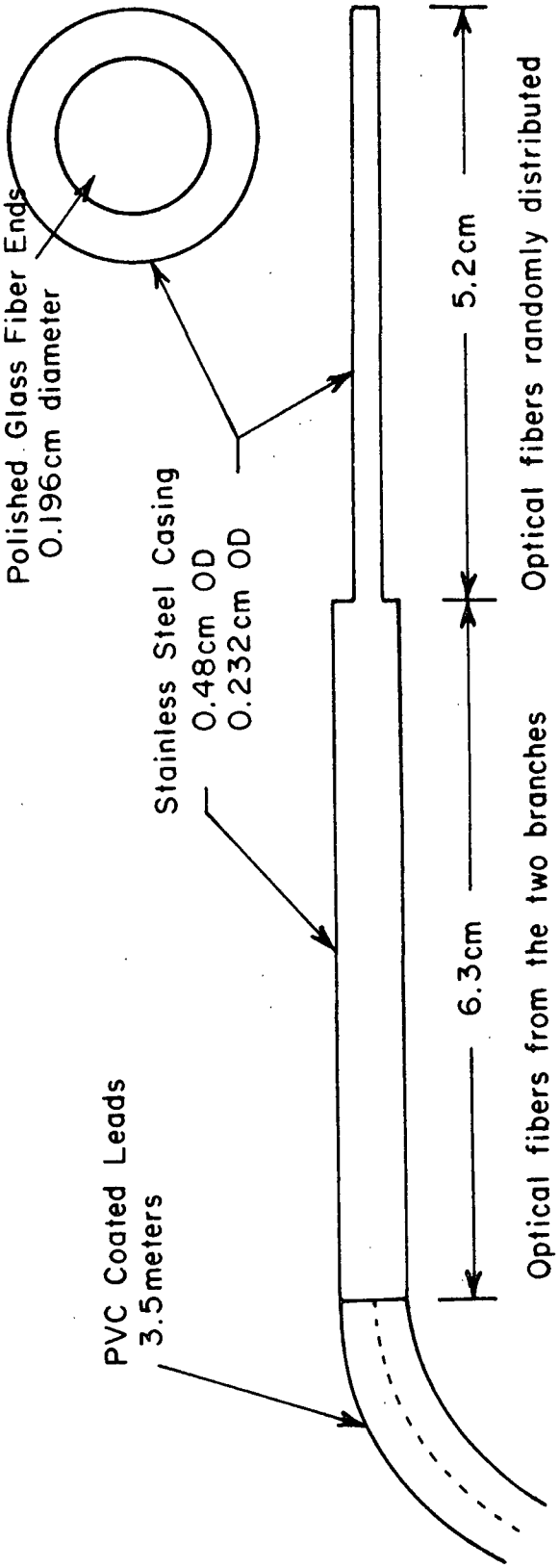

Figure 9. Common End of the Two-Branch Light Guide

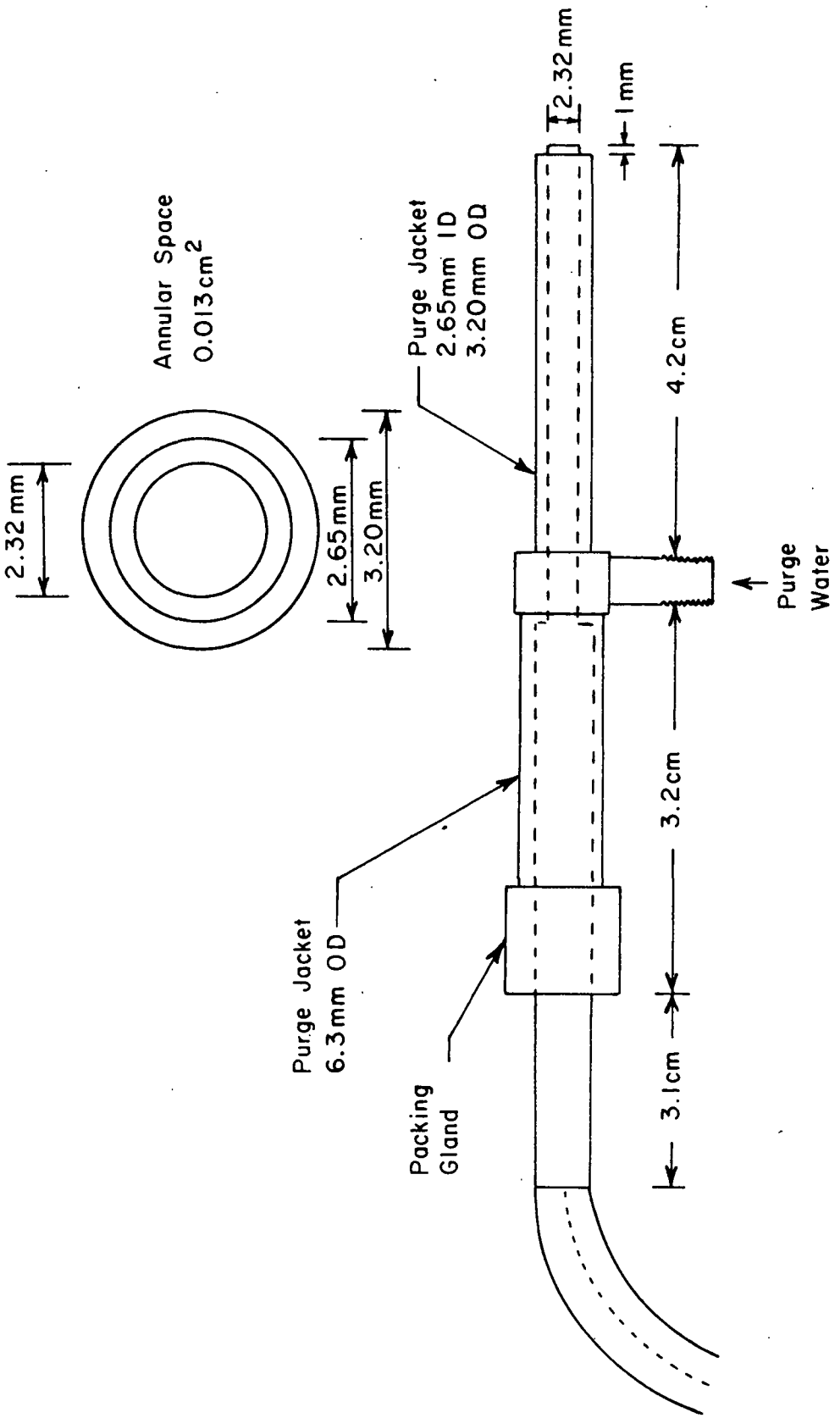

Figure 10. Annular Purge Consistency Probe

probe, the continuous purge water flow around the light guide formed a small, symmetric purge jet around but not over the probe tip. Under the proper conditions the purge prevented fiber interference without affecting the optical signal.

For consistency calibration experiments the probe was free as pictured in Fig. 10, so that it could be temporarily mounted in different ways in the calibration chamber. For the actual consistency measurements in the jet tank, however, the purge jacket attached to the brass plate (Fig. 11). The plate fitted to the traversing block just as it did when it carried the impact probe. The center of the probe tip was 1 cm off of the surface of the plate which put it exactly on the actual jet diameter. The probe tip was 12 cm below the lower edge of the traversing block.

LIGHT SOURCE AND DETECTION CIRCUIT

Light from a stable light source passed through one branch of the light guide, through the common end of the probe, into the fiber suspension. Light reflected in some way from the fibers in the suspension passed through the probe, through the second branch of the light guide to an electronic circuit sensitive to light. The detection circuit produced a reading that had to be calibrated in terms of absolute consistency.

The light source was a quartz-iodine lamp powered by a regulated dc power supply. The light guide branch tip was held at a fixed angle to the lamp but the distance of the light guide tip from the lamp was variable for flexibility during the preliminary calibration experiments. Prior to the final calibration measurements this distance was fixed and remained fixed throughout the rest of the study.

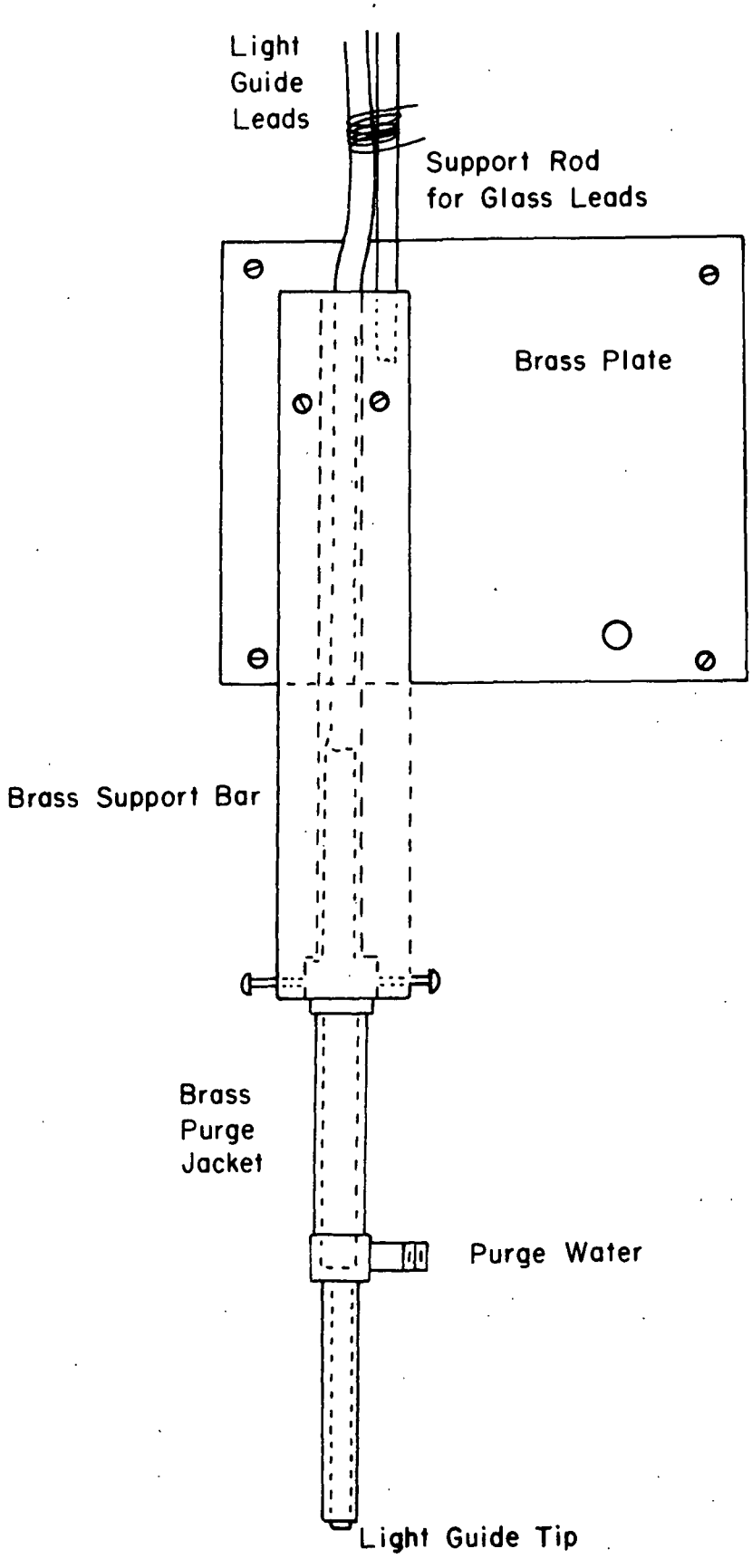

Figure 11. Optical Probe on Brass Plate

The relative intensity of the light reflected and returned through the second branch of the light guide was monitored continuously by the detection circuit. The clad tip of the return branch was held next to the sensitive area of a photoconductive cell. Variations in the reflected light intensity caused a variation in the electrical resistance of the photocell; the resistance was measured in a simple resistance bridge circuit (Appendix IV).

The photocell was a Clairex cadmium-sulfide cell with a rated resistance of 3.3 KΩ at a light intensity of 2 ft candles. The actual reflected light intensity from the nylon-12 suspensions, however, was in the range of 10^{-2}-ft candles and the photocell resistance there was roughly 500 KΩ. Clairex literature (Appendix IV) states that in this intensity range the photocell resistance is slightly dependent on its light history. After an intensity change from dark history to actual lighted operation a wait was necessary while the resistance increased from its initial value. In the experimental system the photocell never received anything approaching the high intensities of room light so this history effect was small. In actual operation up to four hours (at the highest consistency) were required for the signal to drop to its correct constant level when first struck with reflected light after a long dark history. At this low intensity level, also, the response time of the photocell to a reflected light change was quite long (on the order of two seconds to 60% of the total change).

A photoconductive cell was chosen as the sensitive element for the light detection circuit rather than a photomultiplier tube because the slower response time of the photocell produced a mean signal more easily related to the time-mean consistency. The system that Sanders used produced a sensitive fluctuating signal from which a large time-dependent component had to be filtered. No extra electronic damping was needed in the photocell light measuring system.

OPTICAL PROBE CALIBRATION

The recorded indication of the photocell resistance, related by the photocell characteristics to the intensity of light reflected from the suspension, is related in an unknown way to the suspension consistency. Because of the present lack of knowledge of the nature of the reflected light that reenters the light guide and of the flow patterns around the probe tip, a theoretical relationship is not available. The probe must be experimentally calibrated in terms of consistency for a particular suspension. The probe signal should also be checked for effects of the variation of the oncoming suspension velocity and purge water flow rate.

Sanders calibrated his optical probe and light measuring system, without the purge water jacket but with the same wood pulp fibers that he used in his pipe loop experiments (5). He was not able to calibrate his probe in a uniform consistency flow parallel to and impacting on his probe and annular purge water jacket. Thus he could not determine independently whether the velocity of such an oncoming flow affects the consistency signal.

A calibration system built for this purpose in this study held the probe directly into an oncoming suspension flow (Fig. 12). The flow velocity and consistency at the probe tip was known and variable.

Calibration Loop

The calibration system was a continuous flow loop containing an open surface calibration vessel (Fig. 13). The light guide and the purge water tubing passed through the wall of the cylindrical Plexiglas vessel. The probe tip was held just below the orifice of a vertical nozzle about 10 cm under the open suspension surface. The vertically downward flow to the nozzle had to be at the mean bulk consistency of the entire system for proper

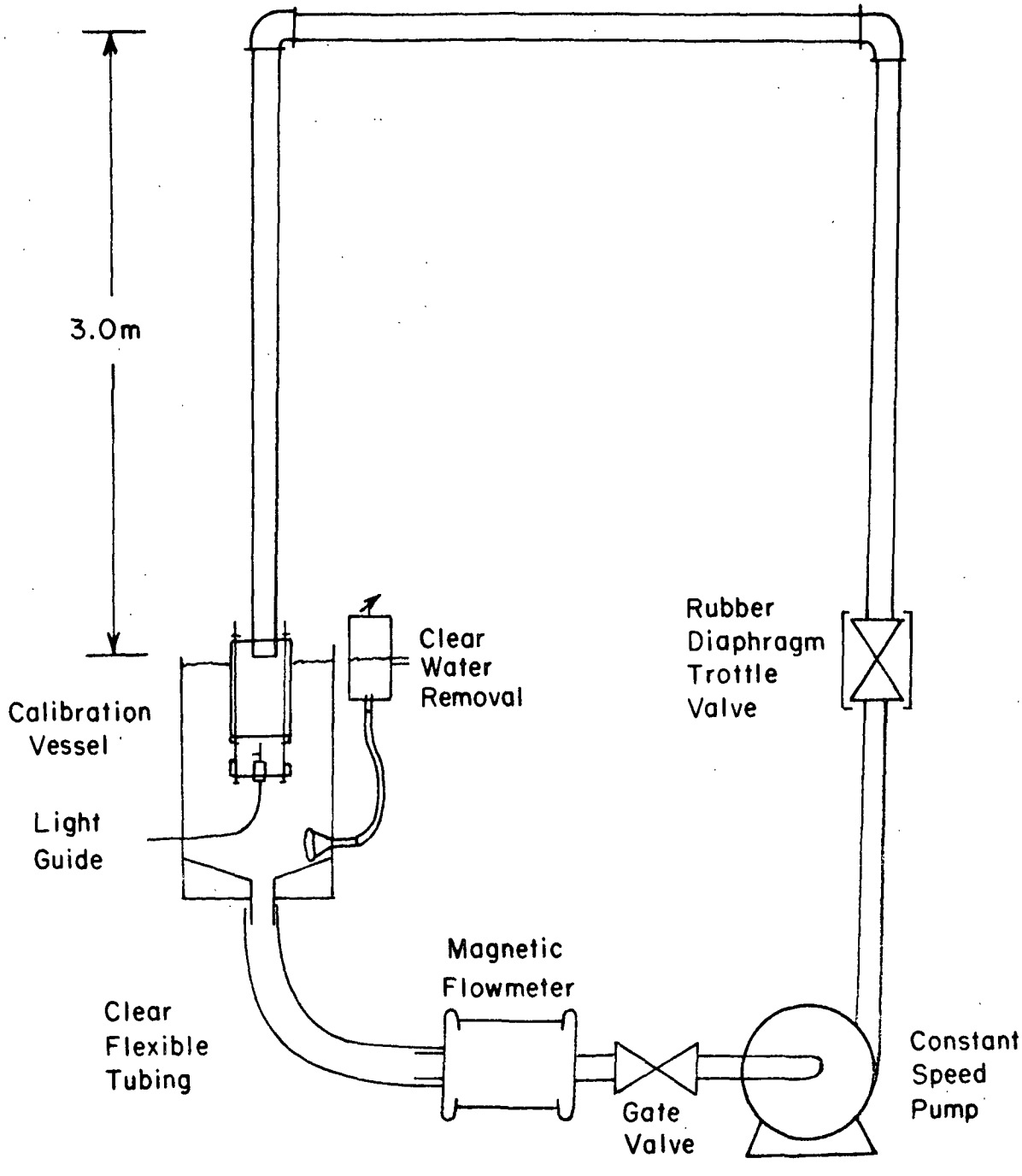

Figure 12. Consistency Probe Calibration System

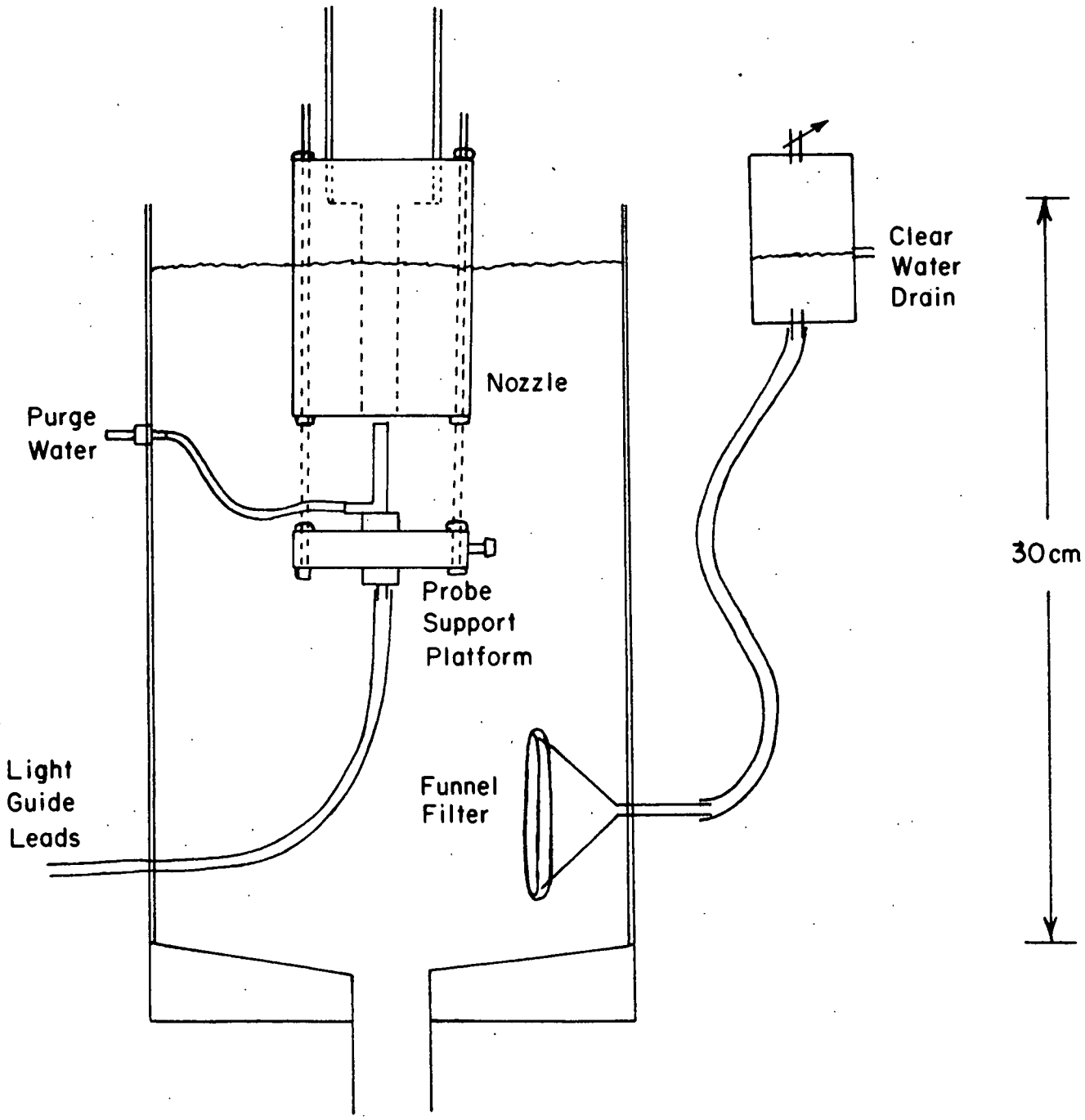

Figure 13. Calibration Vessel

operation. Mixing of the suspension in the vessel was generated by the high velocity flow from the nozzle. The calculated mean retention time of the suspension in the vessel was less than 20 sec; the volume of the vessel is about 10 liters (total system volume was 26 liters) and the flow rates were between 0.5 and 1.5 liters/sec.

The suspension left the vessel through an outlet in the center of the base. A 3-m length of clear flexible tubing carried it to a magnetic flowmeter (the same flowmeter described as a part of the jet tank system). A 1/2-hp pump moved the suspension up a 3 m vertical length of PVC pipe, through two elbows and down a parallel length of the same pipe. The calibration nozzle attached to the lower end of this straight, smooth dropleg.

The unthrottled output of the constant speed calibration loop pump was about 1.7 liters/sec which gives a nozzle velocity of about 600 cm/sec. To produce a variable and lower velocity there was a Hills-McCanna rubber diaphragm throttle valve above the pump on the vertical upleg. Because of the limitations of this pump and valve combination, the minimum practical flow rates at higher consistencies were larger than those in the jet tank. In fact, the lowest attainable velocity through the nozzle, even at lowest consistency, was about 100 cm/sec. At consistencies above about 0.50% the throttle valve plugged with fibers at flow rates below that which gave a nozzle velocity of about 200 cm/sec. Finally, all calibration measurements were made at velocities above about 300 cm/sec to provide sufficient suspension mixing. At lower flow rates the suspension pumped around the loop was of lower consistency than the bulk consistency.

The calibration nozzle was a cylindrical orifice 1.90 cm in diameter and 7.0-cm long drilled on the axis of a PVC rod (Fig. 14). The remaining

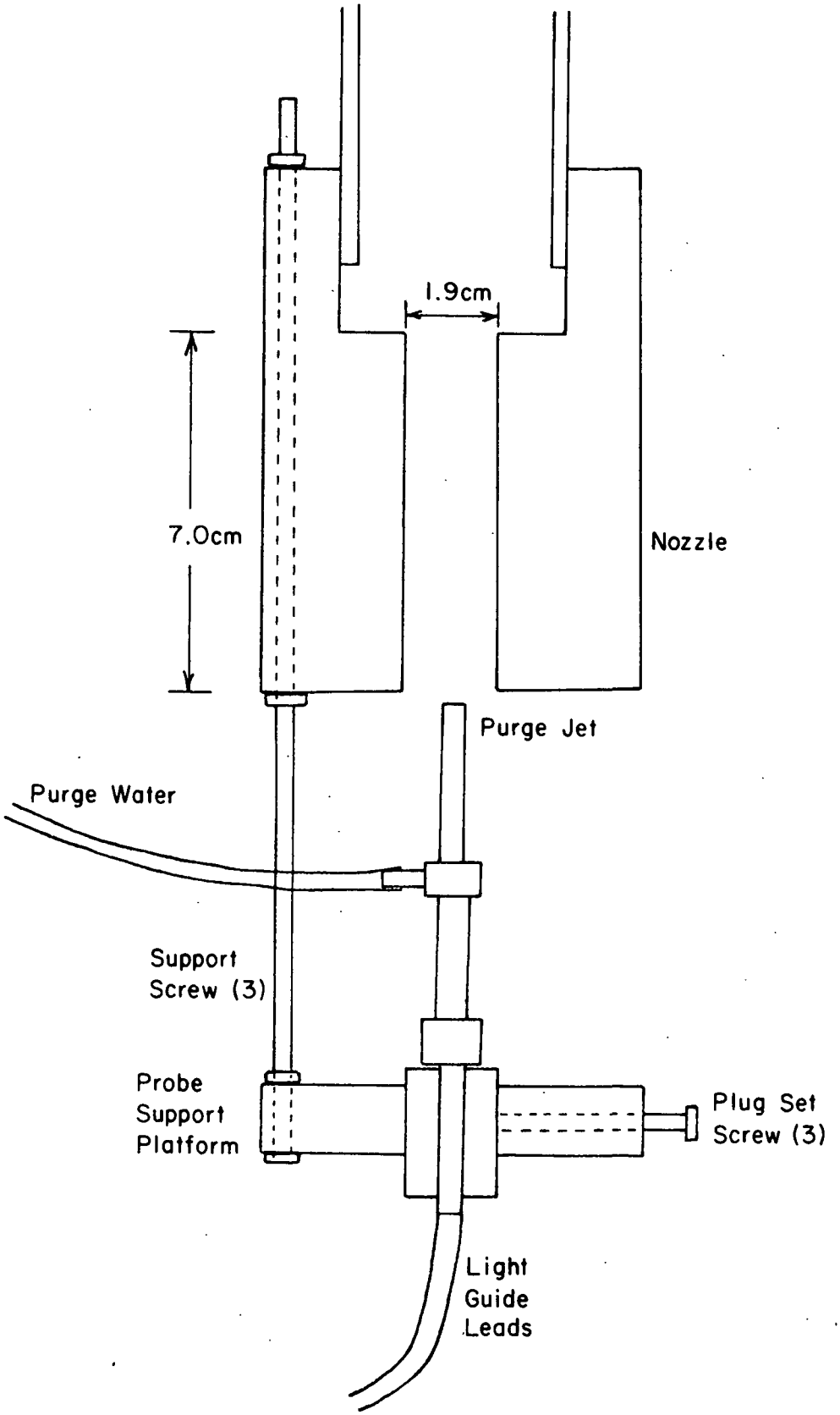

Figure 14. Calibration Nozzle

length of the rod was cut and threaded to screw over the end of the loop dropleg. The suspension flow area was reduced abruptly inside the nozzle from 12.6 to 2.83 cm^2. This contraction ahead of the nozzle was intended to destroy any developed mean velocity or consistency nonuniformities without introducing asymmetry. The nozzle orifice was too short to redevelop time-mean nonuniformities of velocity or consistency. The probe was held securely, directly under the nozzle orifice.

The calibration system volume was small enough so that the purge water had to be continuously removed at the rate at which it was added in order to prevent dilution of the suspension. The purge water was filtered fresh water that passed through a rotometer and an air trap before passing through the probe into the suspension. The conical end of a 75-mm glass funnel, covered with wire mesh and cotton cloth, acted as a filter to remove water from the calibration vessel (Fig. 13). The funnel neck was connected by tubing to the bottom of a small constant level container outside of the calibration vessel. The surface of this container was at the level of the suspension surface in the calibration vessel and addition of purge water caused an equal overflow of water from the constant level container. A level difference of about 1 cm caused no detectable change in the consistency signal from the optical probe.

Purge Water Effects

The dependence of the consistency signal on the purge water flow was investigated first in the calibration loop and then continued in the jet tank. The identical relationship of the purge flow to the optical signal behavior was observed in both systems. As in the case of the purge impact probe, at any suspension velocity there was a range of purge velocities over which the reflected light intensity remained constant. (Purge velocity is purge

water flow rate divided by the approximate annular flow area.) These constant level values were correlated with consistency to obtain a calibration curve.

The purge water flow had to be great enough to keep fibers from stapling over the probe tip. An artificially high concentration of fibers at the tip would have produced a high signal. Too much purge flow would have formed a jet over the tip, pushing fibers away and leaving clear water in front of the probe, producing a low signal. The correct signal had to be found between these two extremes. The correct purge jet was apparently one that extended to the proper point with respect to the light guide tip before slowing to zero velocity and being turned back by the oncoming suspension flow. This point was probably slightly beyond the tip. The mean velocity of the purge where it left the purge jacket was the only control measure of purge extent. For different probes (with different diameters and distances from light guide tip to purge jacket end) purge velocities considerably different from the oncoming suspension velocity could be required to hold the purge jet at a proper level.

The experimental observations verified the expectations but also introduced a new factor. At either of the two extremes caused by an improper purge velocity the optical signal was unsteady. As the purge velocity increased or decreased toward its correct level, the magnitude of the fluctuations decreased. When there were observable individual spikes in the fluctuating signal, they were generally positive (toward higher consistency indication) at a low purge flow rate and negative at a high purge flow rate. The recorded reflected light signal made a careful examination of these fluctuations possible.

This dependence of the signal fluctuation magnitude on the purge jet velocity was an important factor in insuring the proper velocity for a given suspension velocity. The sketch of Fig. 15 shows the light signal response to

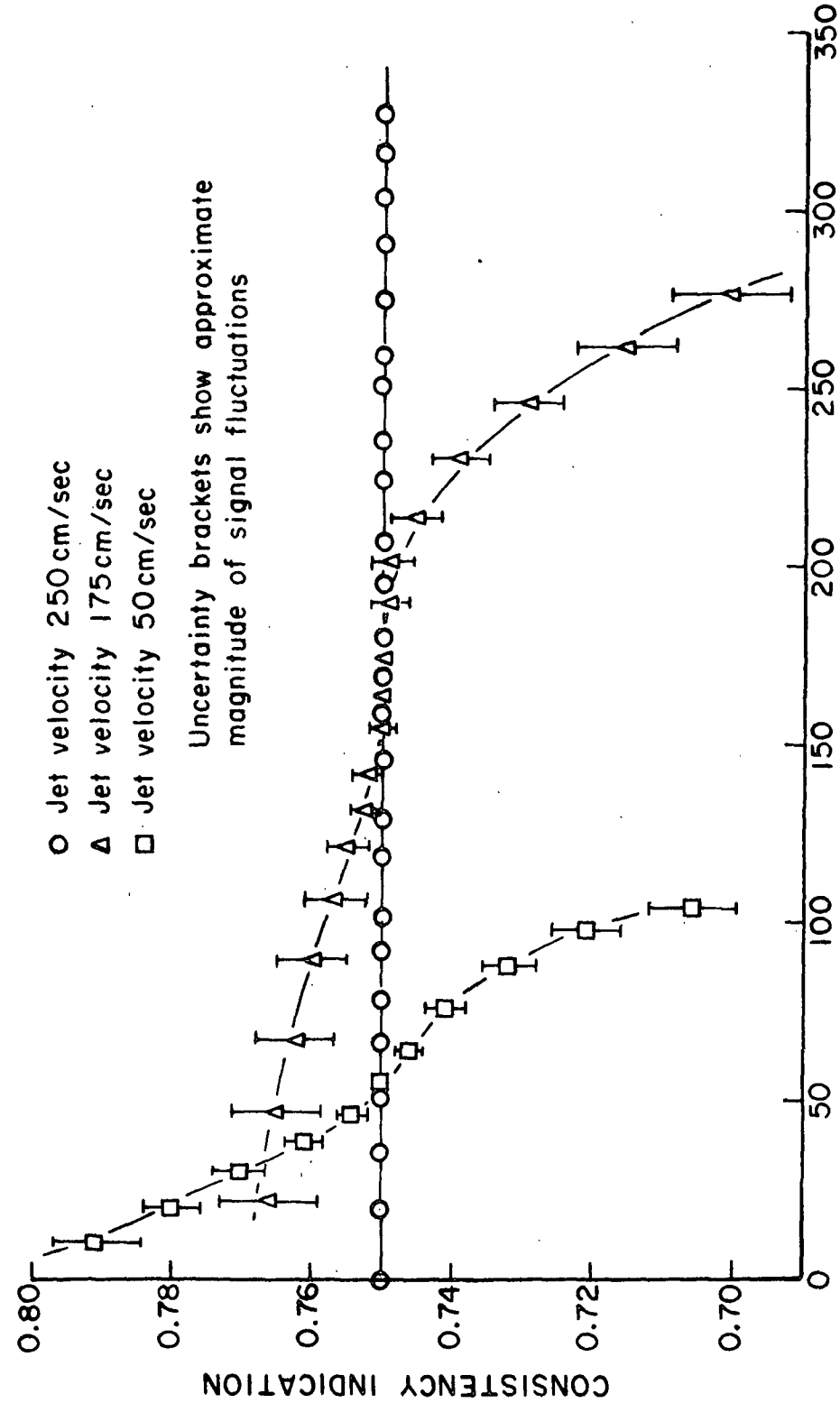

Figure 15. Effect of Purge on Light Signal

changes in purge velocity at three oncoming suspension velocities. The uncertainty brackets at each point represent the observed magnitude of fluctuation.

At sufficiently high suspension velocities, the signal was steady and completely independent of purge velocity. At the lowest suspension velocities the purge water plateau was small and was located most accurately by tuning the purge water velocity to give the lowest signal fluctuation level.

All consistency measurements were made at two or more purge velocities to insure that the signal was at the desired constant value level. As Fig. 15 indicates, this technique was less satisfactory at suspension velocities below about 50 cm/sec. At these velocities the magnitude of the signal fluctuation at different purge flow rates was a better guide to the correct reading. As the suspension velocity neared zero (at the edge of the suspension jet) the correct light signal cannot be determined accurately so that no measurements are reported from that region.

Calibration Curve

The consistency probe calibration curve measurements were made in the calibration loop at velocities above 300 cm/sec. There was no effect of the suspension velocity on the reflected light signal when the purge water was properly adjusted as described in the previous section. Figure 16 shows that the reflected light signal was clearly a smooth function of the suspension consistency as Sanders reported (5). The entire calibration procedure was repeated several times. The actual consistency data were calculated from the weight of fibers added and the known volume of the entire calibration system.

Some interesting data were also available from experiments in the jet tank itself. In preparation for jet consistency distribution measurements

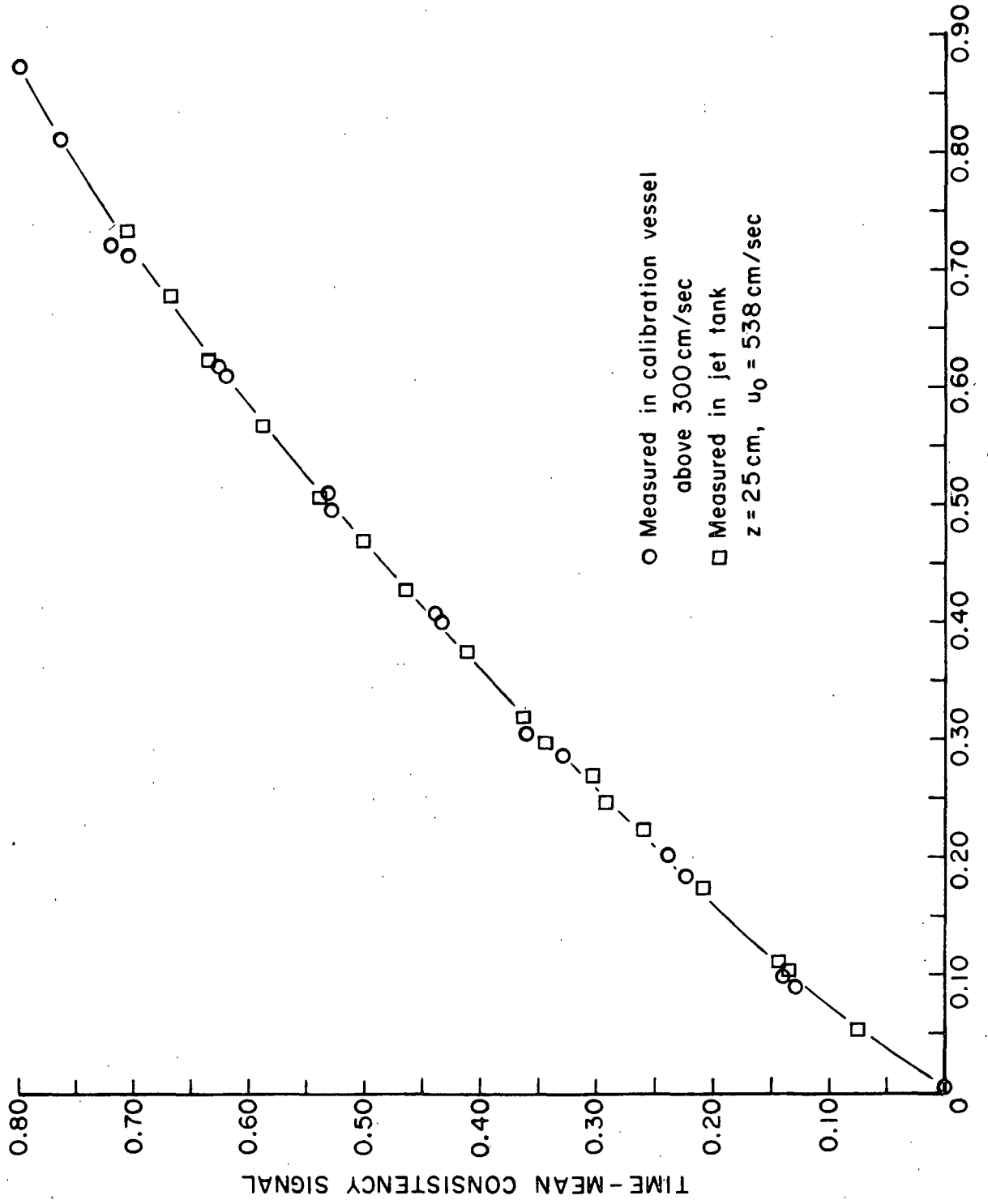

Figure 16. Consistency Probe Calibration Curve

the nylon-12 fibers were normally mixed into the jet flow tank system at a nozzle velocity of 538 cm/sec. This velocity corresponded to the highest of the three flow rates used in the jet tank, providing the most thorough mixing of fibers. The fibers were added in several increments. Consistency samples were taken from the mixing tank after steady-state conditions were reached following the addition of each increment of the fibers.

After each of these consistency increasing increments, measurements were made with the consistency probe at $\underline{r}$ = 0 and $\underline{z}$ = 25, 35, 45, and 55 cm. Those readings made at $\underline{z}$ = 25 cm fell approximately on the cuve from the calibration loop data in Fig. 16. No measurements were made in the jet tank below $\underline{z}$ = 25 cm because the main jet flow was not fully developed there.

CONSISTENCY DISTRIBUTION MEASUREMENT

The consistency distribution measurements were made by moving the optical probe across the width of the jet flow. The position of the probe was determined exactly as for the impact probe. Jet width and the approximate position of the jet axis were known from the velocity measurements. Also it was possible to determine the approximate jet boundary with the optical probe because the light signal became highly erratic as the suspension velocity approached zero. As expected, the magnitude of the signal fluctuations increased steadily from the jet axis to the outer boundary of the flow pattern. The absolute consistency was determined from the measured light intensity signal by using the calibration curve of Fig. 16.

FIBER SUSPENSIONS

Although wood pulp is of great practical interest in suspension studies, it is not always the best fiber to use. Wood fibers are twisted and fibrillated

and have a nonuniform cross section; uniform length is almost impossible to obtain. Important fiber suspension properties change when wood pulp is pumped in a loop or even just soaked in water for long periods. Wood fibers are relatively heavy in comparison to water, even when water soaked; their lack of buoyancy would be a problem in slowly moving flows. In fiber suspension research it is often advantageous to use synthetic fibers to model wood pulp. Fibers of nylon, rayon, or dacron have circular cross sections, can be cut to uniform lengths, do not deteriorate, and absorb insignificant amounts of water. A limited number of parameters describes them completely (9).

SYNTHETIC MODEL FIBERS

The tendency of wood pulp fibers to form fiber networks must be carefully modeled if synthetic fibers are to be used. The fiber length-to-width ratio (L/D) is probably the primary determinant of this behavior at a given consistency. Typical softwood pulp fibers that have been used in suspension studies have L/D ratios of about 50 (5,9). A closely related, and potentially more informative, parameter is the flexibility which is dependent upon the elastic modulus, E, of the fiber and cannot be made quantitative for wood pulp fibers. It can be used to compare synthetic fibers where E is known. The flexibility of a wood pulp fiber is greater than that of nylon fiber of equivalent dimensions. Actually, neither L/D nor flexibility should be relied on quantitatively because the synthetic fiber widths are usually cylinder diameters and the corresponding pulp fiber values are for widths of a thin ribbon. Higher L/D and greater flexibility cause an increase in network formation and departures during flow from Newtonian behavior (9,16).

Several investigators used synthetic model fibers in suspension flow studies (9,11,16). All reported satisfactory results over a wide range of

L/D values. Daily and Bugliarello used two sizes of nylon with L/D ratios of 334 and 369 (9). Mih and Parker used rayon of about the same size (L/D = 381) (11). Bobkowicz and Gauvin used much shorter nylon fibers; a range of widths and lengths gave them L/D values approximately from 12 to 51. The lengths of their fibers ranged from 0.5 to 1.0 mm (16,17). The phenomenon of network formation was apparently observed in each case, although Bobkowicz and Gauvin had to work at rather high consistencies.

Daily and Bugliarello reported that they experienced great difficulty in dispersing their nylon fibers at suspension consistencies above 0.5%. With dispersing agents and antifoaming chemicals they produced satisfactory results below 0.5% but the "experiments became increasingly time-consuming, limiting in turn the amount of data obtainable (9)."

In the confined suspension jet used in the present study the circulation loops along the tank walls promoted mixing of the fibers but were too slow to keep wood pulp fibers from settling out on the tank baseplate. The specific gravity of rayon is 1.5, of nylon-6 is 1.14, compared to wet wood pulp fiber at roughly 1.2. These commonly used synthetic fibers would also settle in the slow jet tank recirculation loops. Because of the large volume of fluid needed, no fluid except water was practical in the jet tank. Therefore, a fiber with a specific gravity close to 1.00 was required. The only fiber meeting this criterion was a new nylon called nylon-12 that had never been reported in a fiber suspension study before.

SUSPENSIONS OF NYLON-12 FIBERS

Nylon-12 is so named because of its straight chain structure of acid amide groups and the 12 carbon atoms in its monomer unit (32). Its properties are similar to those of other polyamides (nylons) except that nylon-12

has a specific gravity of 1.01. Nylon-12 has a modulus of elasticity of 170,000 compared to 212,000 psi for nylon-6. When water-soaked for 1000 hours, it absorbs 1.5% of water, compared to about 10.5% for nylon-6. Its linear swelling in water is 0.2%, compared to 2.5% for nylon-6.

Nylon-12 proved to be an excellent fiber for the turbulent suspension flow studies but there were two drawbacks to its use. Little nylon-12 has been extruded into monofilament and no nylon-12 had been made at all in this country. It is much more expensive to produce than are regular nylons and offers no advantages as a commercial fiber. Therefore, its availability will continue to be limited. The fiber used in this study was produced as a monofilament by Grilon, SA., in Switzerland, and was cut by Cellusuede Products, Inc., in Rockford, Illinois. The other problem was that it was difficult to disperse the nylon-12 in water. The long hydrocarbon chain of nylon-12 (nearly a paraffin structure) is responsible for the low specific gravity and water absorption but also makes the fiber extremely hydrophobic.

Only about 25 kg of 6 denier ($\underline{D}$ = 29.1 microns) nylon-12 could be obtained. It was cut to a uniform length of 3 mm. This gave a fiber ratio of $\underline{L}/\underline{D}$ = 103. A longer fiber might have flocculated excessively; shorter fibers might not have shown the characteristics of a wood fiber suspension.

The untreated fibers did not disperse in water. When forced to disperse by agitation, they carried air bubbles with them and returned immediately to the surface. The addition of a small amount of wetting agent called Triton X-100 (alkyl phenoxy polyethoxy ethanol), dissolved in ethanol, immediately removed the air and dispersed the fibers. Much of the TRX-100 apparently stayed on the fiber surfaces when the water was drained from the suspension. Only a small amount of makeup TRX-100 — ethanol solution was required each

time the fibers were put back into suspension once they were initially treated unless they were rinsed in water.

A consistency sampling study showed that dip samples of the nylon-12 suspension taken at the top of the jet tank were of the same consistency as those from the mixing tank at the same time. This sampled consistency was equal to the calculated bulk consistency based on the weight of dry fiber added to the system. All of the fibers that could be seen through the Plexiglas baseplate were in motion. Thus, it is probable that all of the nylon-12 fiber was in the suspension and well mixed.

Three jet flow rates were used in jet measurements in the tank. At the two higher flow rates the nylon-12 from the tank baseplate dispersed into a flowing suspension immediately after the pump was first turned on. The lowest flow rate, however, would not bring all of the fiber off the baseplate after any length of time. If the suspension was initially mixed at higher flow rates, the low flow rate did keep the fibers in suspension for many hours afterward (at least). Initial experiments with wood pulp showed that there were always wood fibers on the baseplate at all flow rates.

The nylon-12 fibers were nearly transparent in water. As expected, a preliminary investigation revealed that the amount of light reflected by the nylon-12 in suspension was much less than that from an equal consistency suspension of wood fibers.

RESULTS

Local time-mean velocities and consistencies were measured in the submerged fiber suspension jet at various transverse distances at four axial distances in a single vertical plane containing the jet axis. They are presented as profiles of velocity or consistency across the jet flow. An analysis of the velocity profiles resulted in values for the empirical parameters characterizing the profiles. No analysis of the consistency distributions were required since they were found to be uniform.

JET VELOCITY DISTRIBUTIONS

Each of three different jets was studied both in water and at a nylon-12 fiber consistency of 0.75%. One of the jets was also investigated at several intermediate consistencies. The three jets were formed through the same nozzle ($\underline{d}_o$ = 2.27 cm) at different average initial velocities of 383, 475, and 538 cm/sec. The three velocities were chosen arbitrarily except that the lowest was at the minimum pump speed. The initial jet momentum values (actually momentum rate divided by water density), were $\underline{M}_o = \pi\, \underline{u}_o^{\,2}\, \underline{r}_o^{\,2}$, are 5.94×10^5, 9.13×10^5, and 11.71×10^5 cm^4/sec^2, for the low, medium, and high speed jets, respectively. Traditional jet theory predicts that this initial momentum should be the single experimental variable necessary to characterize a given pure fluid jet issuing into an infinite volume of the stationary fluid.

The two important empirical constants, $\bar{\underline{u}}_m$ and $\underline{r}_c$, were determined from the experimental velocity distribution, $\bar{\underline{u}}(\underline{r})$. They could have been found graphically with reasonable accuracy by drawing a curve (or by fitting one of the three analytical curves of Fig. 2) through the data. The accuracy of this procedure would have depended on the accuracy of the determination

of the axis of symmetry of the data. The experimental scatter of the data would have made precision in this step difficult to obtain.

If one of the approximate analytical expressions for the velocity distributions were assumed, the best values of $\bar{u}_m$ and r_c for each profile could be determined statistically. The reduced data were most accurately represented by the error curve Equation (18) which is repeated here:

$$\bar{u}/\bar{u}_m = \exp[-0.694(r/r_c)^2] \qquad (18)$$

The data for each profile were fitted to this expression by least-squares analysis. Although the error curve did not represent the data perfectly, the values of r_c and $\bar{u}_m$ computed in this way, were usually as accurate as the best that could have been obtained graphically.

For all of the velocity distribution data, the computed $\bar{u}_m$ and r_c values were inspected graphically for reasonableness by plotting the reduced profiles as $\bar{u}/\bar{u}_m = g(r/r_c)$. The reduced profiles, in turn, permitted a visual inspection of the fit of the data to the error curve and a test of the similarity of the profiles. In this form the data could also be compared to the other semiempirical curves of Fig. 2 and to published data.

Once the value of r_c was obtained for the profiles of a given jet, it was possible to check its predicted proportionality to the distances of the profiles from the jet origin. This law of linear spread of the jet could be evaluated with the values of the measured axial distances from the nozzle, z, by rewriting Equation (19):

$$r_c/(z+a) = C_r, \qquad (77)$$

where the constant, C_r, was predicted to be $1.82/\sigma$ in the Abramovich analysis. The empirical jet constant, σ, can thus be obtained immediately. As described earlier, a is the distance from the plane of the nozzle to the virtual origin of the jet flow pattern. A value of a was determined for each jet.

The analysis that led to the proportionality of r_c and z also led to Equation (22) which can be rewritten simply as

$$\bar{u}_m/u_o = C_u/(z+a), \tag{78}$$

where $C_u = 0.645\ \sigma\ r_o$ in the Abramovich analysis.

If the experimental jet fitted the theory exactly, then the value of a that made Equation (77) correct for a given jet would be identical to that determined from Equation (78). In general, however, two different values are usually found. The magnitude of the discrepancy might be a rough measure of the nonideality of the specific experimental jet. If the location of the virtual origin determined from the axial velocities were called a_u, then the distance to that virtual origin from the profile would be $z + a_u$. Similarly, the location of the origin as determined from the values of r_c can be called a_r and that origin is then a distance $z + a_r$ from the profile.

WATER JETS

Velocity distribution measurements were made at four axial distances (z = 25, 35, 45, and 55 cm) in each of the three jets in water. The water jet profiles permitted comparison of the experimental jet with previously reported jets of Newtonian fluids. The complete set of results for the jet with an initial velocity of u_o = 475 cm/sec is presented here; those for the other two are in Appendix VI.

Figure 17 shows the four measured profiles as $\bar{u}(r)$. The four profiles in reduced form are given in Fig. 18 along with the error curve.

Figure 19 is an illustration of a graphical analysis of the lines represented by the two equations

$$z = [(1/C_r)(r_c)] - a_r, \tag{79}$$

$$z = [C_u/(u_m/u_o)] - a_u. \tag{80}$$

A simple linear least-squares analysis of the four points for each line establishes the constant slope values (which could give σ) and the intercepts, a_r and a_u.

Table I gives numerical results for the three water jets. The Abramovich formulas of Equation (19) and Equation (22) were used to determine the values of σ. If it is assumed that the differences in the values of a_r for the three jets are due to experimental error, than a mean value of $a_r = 6.0$ cm is a meaningful result. A mean value of σ_r (based on the r_c analysis) is 22.3. Similarly, the mean value for a_u is 1.5 cm and for σ_u (from the u_m analysis) is 19.5. The values of the empirical jet constant are in good agreement with the range of values reported in the literature.

SUSPENSION JETS

Velocity distribution measurements were made at four axial distances in the three jets at a suspension consistency of 0.75%. This was the highest consistency possible in the jet tank with the quantity of nylon-12 fibers available. The complete results for the jet with $u_o = 475$ cm/sec are presented here; those for the other two are in Appendix VII.

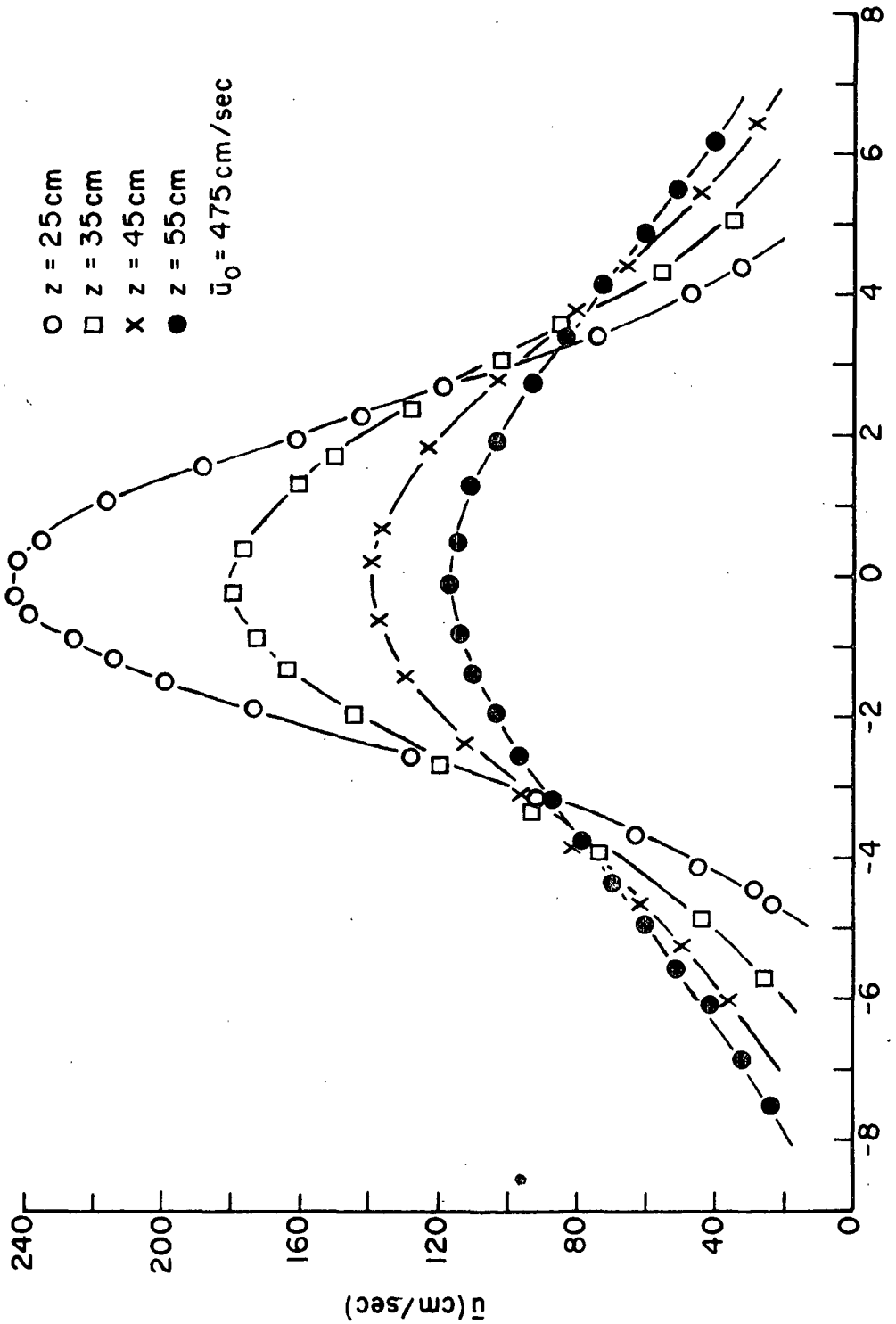

Figure 17. Velocity Profiles, Water

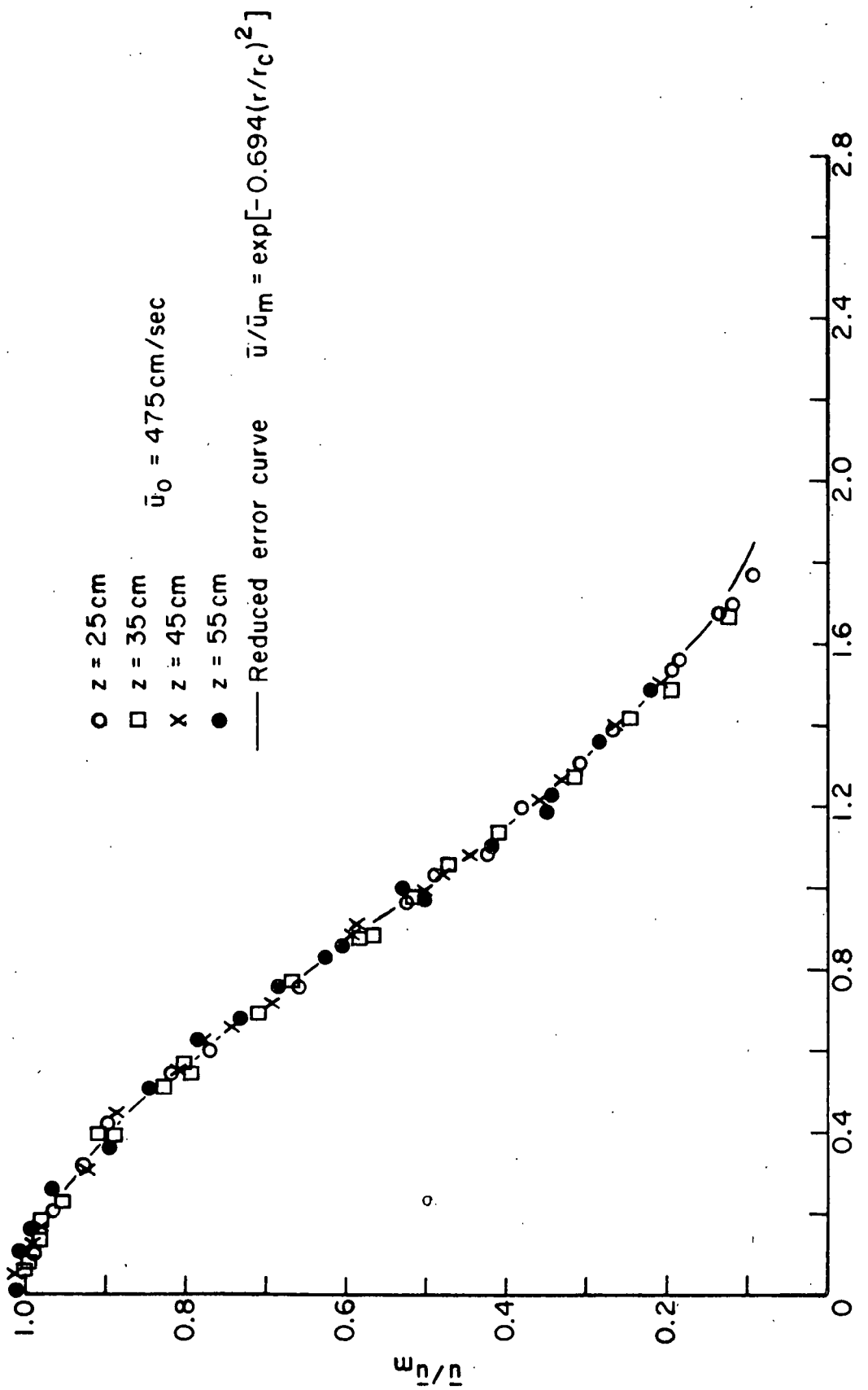

Figure 18. Reduced Velocity Profiles, Water

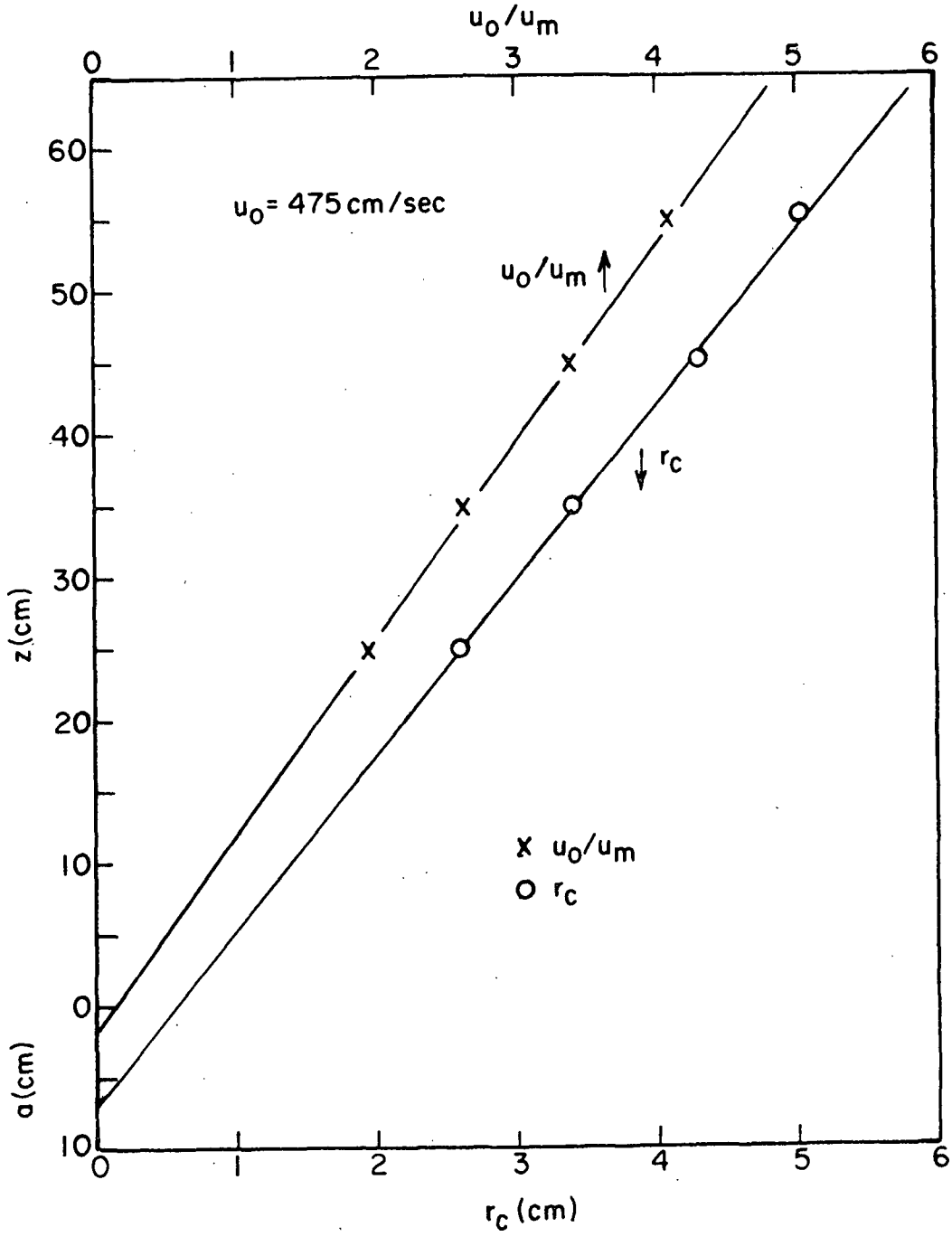

Figure 19. Graphical Determination of $\underline{a_r}$ and $\underline{a_u}$ for Water

TABLE I

SUBMERGED WATER JET

Basic Data			Analysis with a_r				Analysis with a_u				Momentum Flux	
z, cm	r_c, cm	u_m, cm/sec	r_c/z	a_r, cm	$z+a_r$, cm	C_r	$z(u_m/u_o)$, cm	a_u, cm	$z+a_u$, cm	C_u, cm	$r_c u_m$, cm^2/sec	M/M_o
						u_o = 383 cm/sec						
25.0	2.59	202	0.103		30.6	0.0846	13.2		27.0	14.3	524	1.05
35.0	3.38	149	0.097	5.6	40.6	0.0833	13.6	2.0	37.0	14.4	504	0.97
45.0	4.24	116	0.094		50.6	0.0838	13.5		47.0	14.3	492	0.91
55.0	5.10	96	0.093		60.6	0.0842	13.6		57.0	14.3	490	0.91
						0.0839 mean				14.3 mean		
						σ_r = 21.6				σ_u = 19.6		
						u_o = 475 cm/sec						
25.0	2.62	244	0.105		32.2	0.0814	12.9		26.8	13.8	640	1.01
35.0	3.41	180	0.098	7.2	42.2	0.0808	13.3	1.8	36.8	13.9	614	0.93
45.0	4.30	140	0.095		52.2	0.0824	13.3		46.8	13.8	602	0.89
55.0	5.03	116	0.092		62.2	0.0809	13.4		56.8	13.9	583	0.84
						0.0814 mean				13.9 mean		
						σ_r = 22.3				σ_u = 19.1		
						u_o = 538 cm/sec						
25.0	2.39	302	0.096		30.2	0.0791	14.0		25.7	14.4	722	1.01
35.0	3.16	220	0.090	5.2	40.2	0.0786	14.3	0.7	35.7	14.6	695	0.93
45.0	3.96	172	0.088		50.2	0.0789	14.3		45.7	14.6	681	0.90
55.0	4.75	140	0.087		60.2	0.0789	14.3		55.7	14.5	666	0.85
						0.0788 mean				14.5 mean		
						σ_r = 23.0				σ_u = 19.9		
				a_r(mean)= 6.0		σ_r(mean)=22.3		a_u(mean)= 1.5		σ_u(mean)=19.5		

Figure 20 shows the four measured profiles as $\bar{u}(r)$. Figure 21 gives the four profiles in reduced form along with the error curve. The suspension profiles show profile similarity and fall on the reduced error curve exactly as do Newtonian jet profiles. Comparison of Fig. 20 with Fig. 17, however, shows a significant difference between the suspension jet and the water jet. The two jets have identical initial momentum values but the velocity at a given point in the suspension jet profile is lower than that in the corresponding water jet profile. The reason for this difference is discussed in the following section.

Figures 22-25 show the four suspension profiles plotted below the corresponding water profiles. The difference between the water jet velocities and the suspension jet velocities is nearly uniform across the jet width.

Table II shows the results for the suspension jets presented in the same form as for the water jets. The values of a_r and a_u are not equal and are larger than the corresponding water jet values. Figure 26 shows the lines of Equations (79) and (80). The differences between σ_r and σ_u are greater than for the water jet. In fact, σ_r (mean) = 25.3 is slightly greater than the highest values of σ reported in the literature, and σ_u (mean) = 18.2 is slightly less than the lowest. The theory that requires a constant value of σ (and, in fact allows its calculation) assumes momentum conservation in the z-direction.

JET MOMENTUM ANALYSIS

If momentum flux is conserved in an experimental jet so that

$$M(z) = M_o = \pi u_o^2 r_o^2, \tag{81}$$

is valid, a formula for $M(z)$ can be obtained from Equation (24):

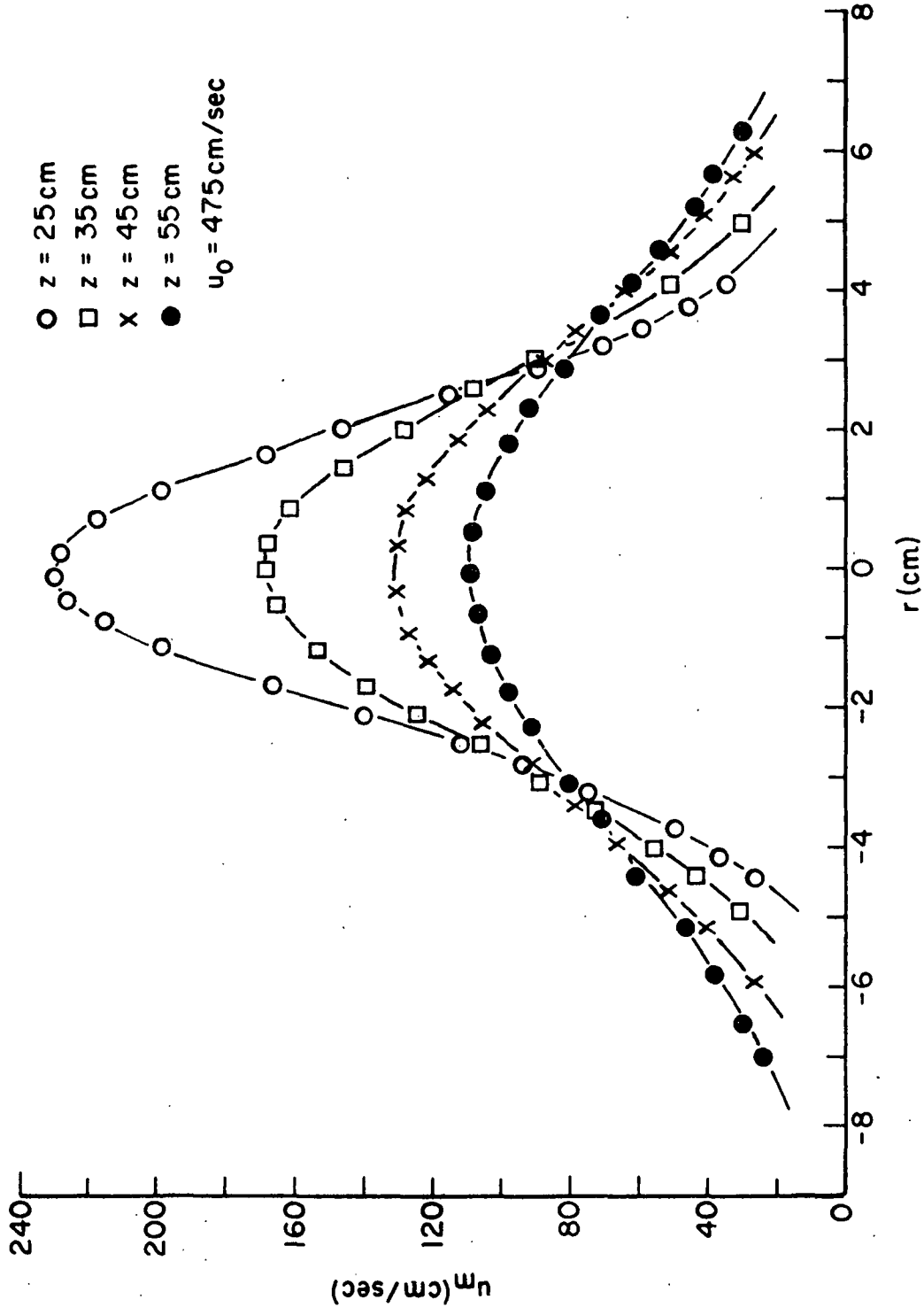

Figure 20. Velocity Profiles, 0.75% Consistency

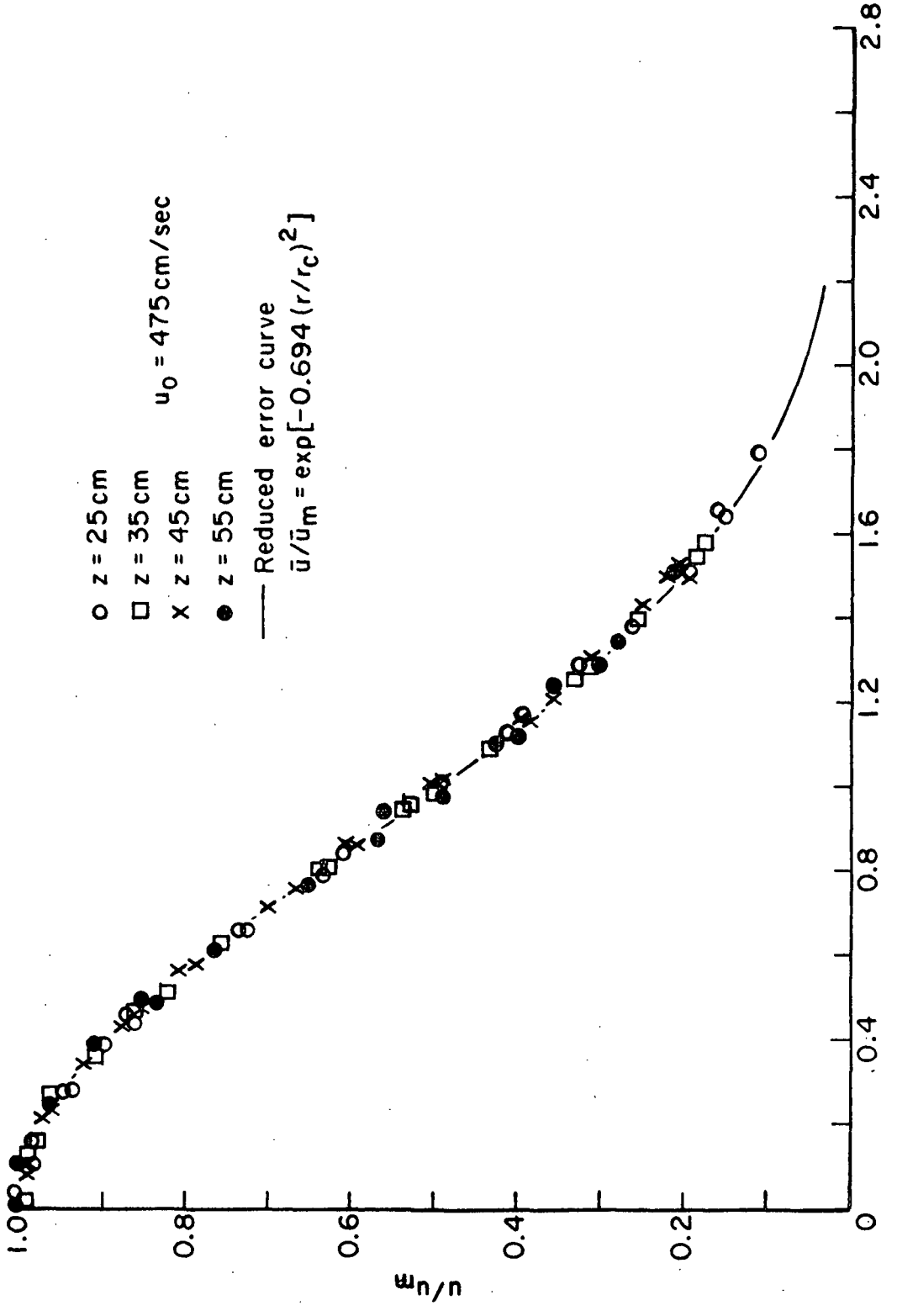

Figure 21. Reduced Velocity Profiles, 0.75% Consistency

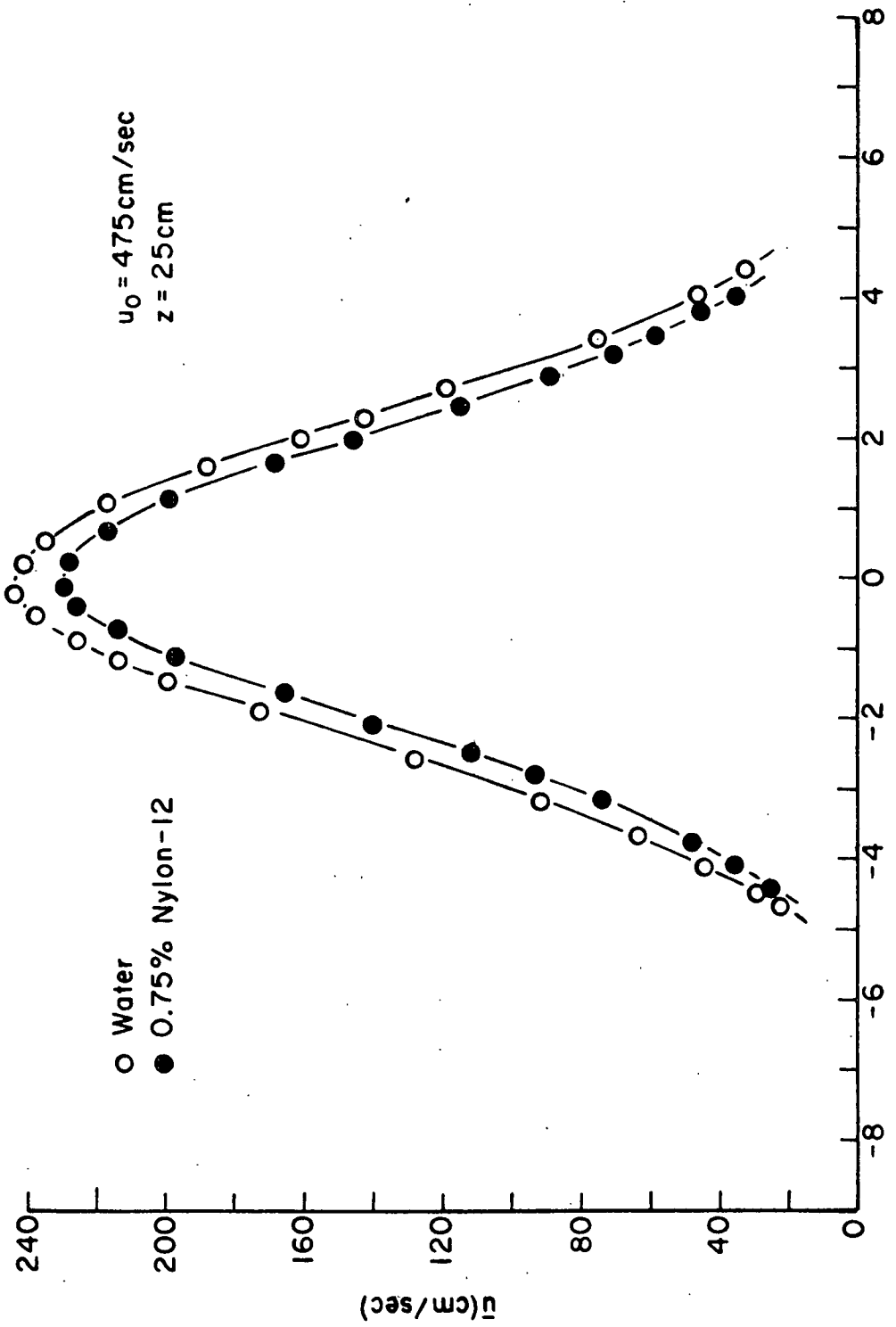

Figure 22. Velocity Profiles

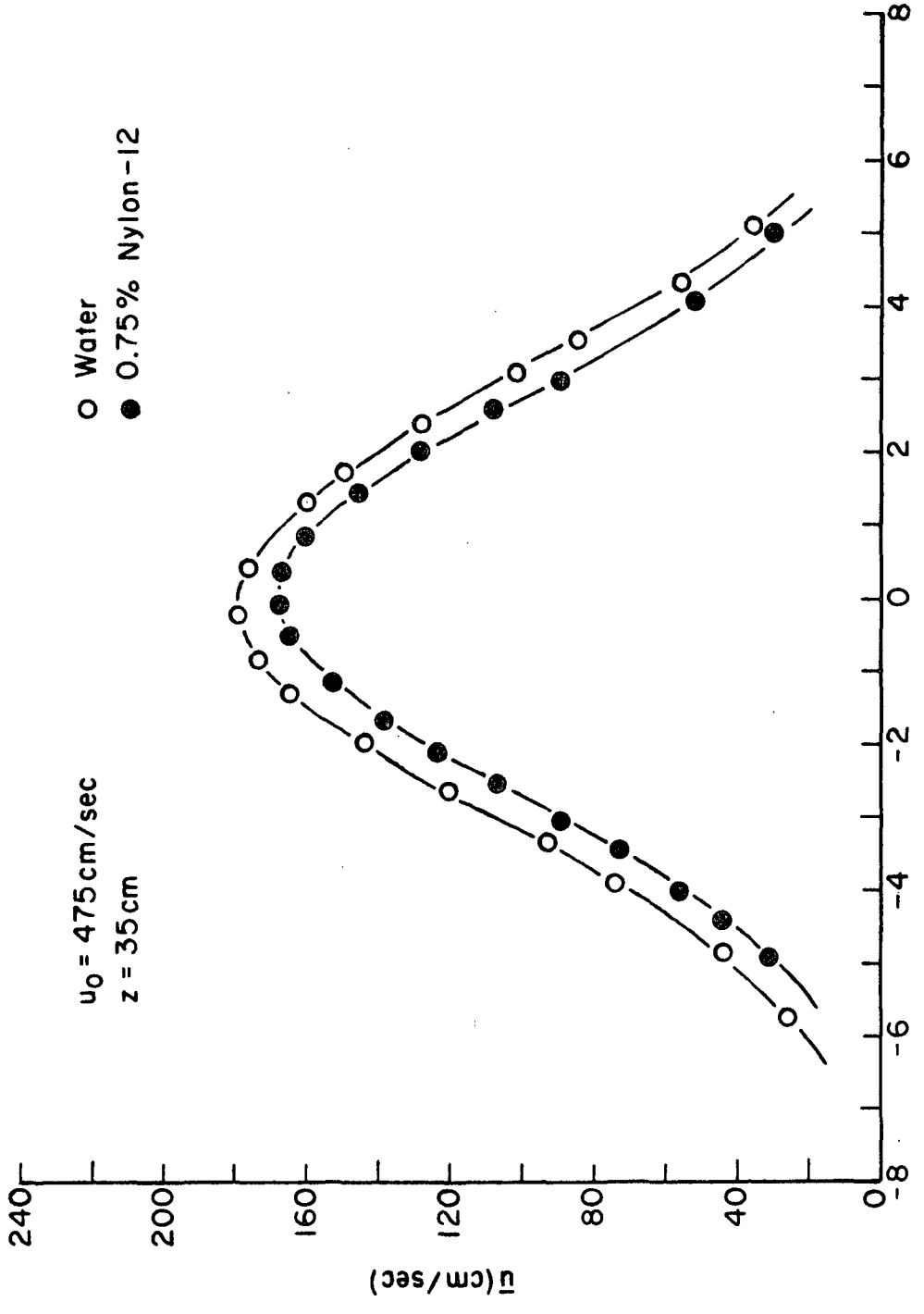

Figure 23. Velocity Profiles

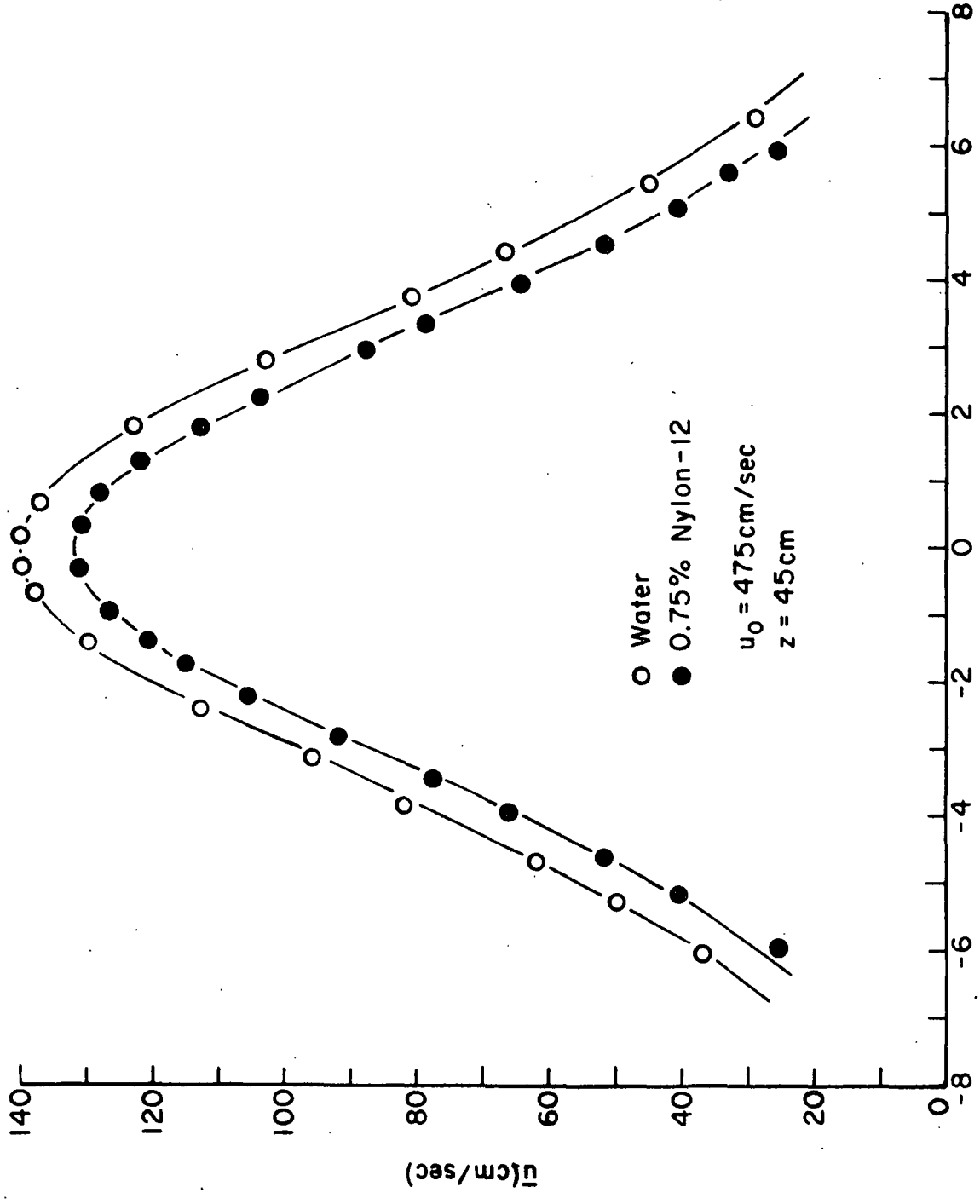

Figure 24. Velocity Profiles

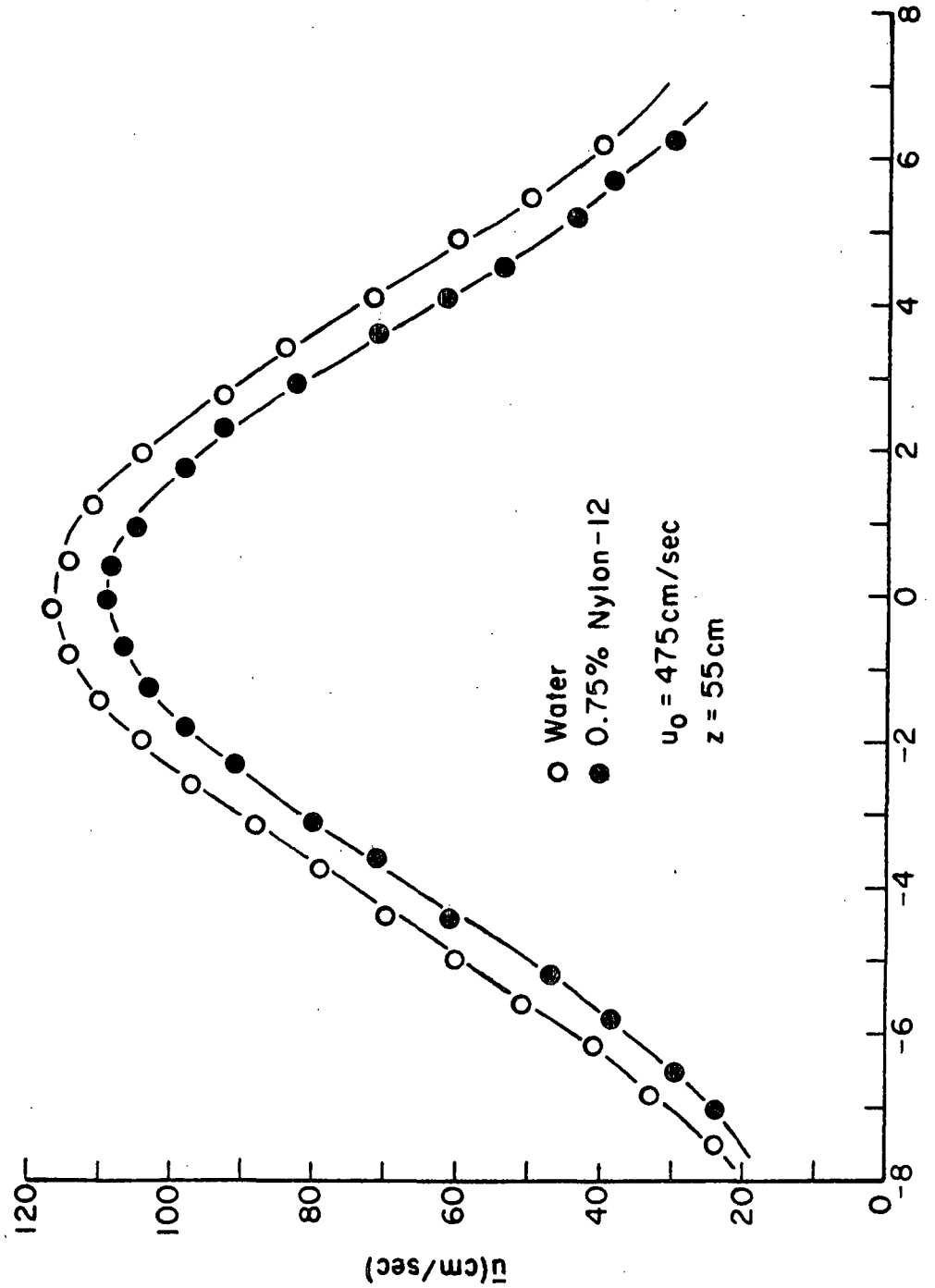

Figure 25. Velocity Profiles

TABLE II

SUBMERGED SUSPENSION JET
0.75% Nylon-12

Basic Data			Analysis with a_r				Analysis with a_u				Momentum Flux	
z, cm	r_c, cm	u_m, cm/sec	r_c/z	a_r, cm	$z+a_r$, cm	C_r	$z(u_m/u_o)$, cm	a_u, cm	$z+a_u$, cm	C_u, cm	$r_c u_m$, cm²/sec	M/M_o
						u_o = 383 cm/sec						
25.0	2.52	180	0.101		35.1	0.0719	11.8		26.9	12.6	454	0.79
35.0	3.28	131	0.094	10.1	45.1	0.0727	12.0	1.9	36.9	12.6	430	0.70
45.0	3.94	103	0.087		55.1	0.0715	12.1		46.9	12.6	405	0.63
55.0	4.70	85	0.085		65.1	0.0722	12.2		56.9	12.6	402	0.61
						0.0721 mean				12.6 mean		
						σ_r = 25.2				σ_u = 17.3		
						u_o = 475 cm/sec						
25.0	2.49	229	0.100		33.9	0.0734	12.1		27.3	13.2	570	0.80
35.0	3.17	168	0.091	8.9	43.9	0.0722	12.4	2.3	37.3	13.2	532	0.70
45.0	3.95	132	0.088		53.9	0.0733	12.5		47.3	13.2	521	0.67
55.0	4.66	109	0.085		63.9	0.0730	12.6		57.3	13.2	508	0.64
						0.0730 mean				13.2 mean		
						σ_r = 24.9				σ_u = 18.1		
						u_o = 538 cm/sec						
25.0	2.46	274	0.098		34.7	0.0709	12.7		25.9	13.2	674	0.88
35.0	3.14	200	0.090	9.7	44.7	0.0702	13.0	0.9	35.9	13.3	628	0.76
45.0	3.82	157	0.085		54.7	0.0698	13.1		45.9	13.4	600	0.70
55.0	4.58	127	0.083		64.7	0.0706	13.1		55.9	13.3	581	0.65
						0.0704 mean				13.3 mean		
				a_r(mean)=		σ_r = 25.8		a_u(mean)=		σ_u = 18.2		
				9.6		σ_r(mean)=25.3		1.7		σ_u(mean)=17.9		

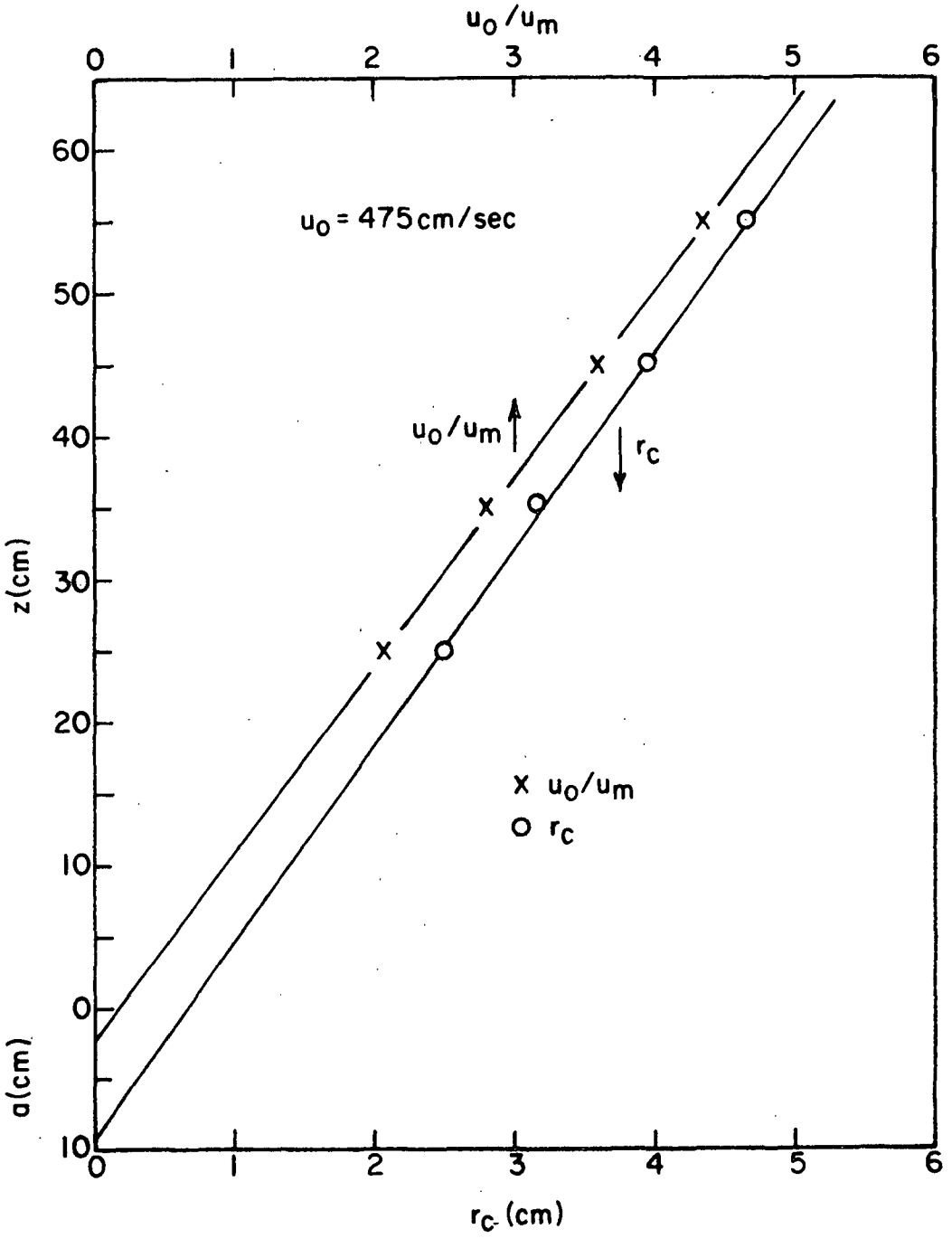

Figure 26. Graphical Determination of $\underline{a}_{\underline{r}}$ and $\underline{a}_{\underline{u}}$ for a Suspension Jet (0.75% Nylon-12)

$$M(z) = \pi(u_m^2\, r_c^2)/1.178^2 \tag{82}$$

Equation (82) is written in terms of the two empirical constants for each velocity profile of any experimental jet. If this same formula were used with the $\bar{u}_m$ and r_c values from a particular nonideal submerged jet where z-direction momentum flux was not constant, an $M(z)$ would be obtained that differed from $M_o = \pi\, u_o^2\, r_o^2$. The ratio $M(z)/M_o$ and the extent of its variation with z would indicate the degree of the nonideality:

$$M/M_o = [(\bar{u}_m/u_o)/(1.178\; r_o/r_c)] \tag{83}$$

Values of M/M_o (and of $\bar{u}_m r_c$) determined from Equation (83) are listed in Tables I and II. In the water jet they decrease from near unity with increasing z. In the suspension jet they decrease with increasing z at a level well below unity. The jet momentum balance that follows shows that the z-dependence can be caused by recirculating flows in the confined experimental jet tank.

The analysis leading to Equation (83) assumed a good fit of the experimental data to the error curve, Equation (18), for the jet profile at which the momentum is to be calculated. It also assumed that all profiles in a given jet fit Equation (18), that is, that the profiles are all similar. The decrease in M/M_o with increasing z, calculated from Equation (83) might not be real, then, if the profiles were not nearly similar or if the data were not actually a good fit to the error curve.

It is possible to check the calculated values of M/M_o by graphical integration of actual measured velocity profiles to determine $m(z)$. Since $m(z) = 2\pi \int u^2 r\,dr$, it is also true that $m(z) = \pi \int u^2 d(r^2)$ and the momentum is the area under the curve of u^2 plotted against r^2, multiplied by π. This

analysis (Simpson's rule) was made for the four water jet profiles in the jet with u_o = 475 cm/sec. At z = 25, 35, 45, and 55 cm the measured M/M_o values were 1.00, 0.91, 0.86, and 0.83. These are all slightly lower than the corresponding calculated values in Table I but the momentum decrease is certainly verified.

Confined Jet Momentum Balance

The momentum conservation assumption is valid if external forces do not act on the ideal submerged jet issuing into fluid which is otherwise at constant velocity. A receiving body of fluid at constant velocity (or motionless in the simplest such case) is difficult to achieve, especially in liquid submerged jets where confining walls are necessary. It was impossible to insure a zero z-direction momentum in the surrounding fluid in the jet tank.

A momentum balance can be written for the submerged jet with confining walls. Consider cylindrical walls with radius, r_i, and an axis coinciding with the jet axis. Figure 27 schematically illustrates the jet shape and velocity profile, along with streamlines for the ideal case. Actually the fluid entrained by the jet may have a z-direction velocity component. The size of the jet flow area is shown out of proportion to the size of the confining jet tank. The area of jet flow is actually small in comparison to the area between the jet and the tank wall where a counterflow exists, generally in the negative z-direction.

The flux of z-direction momentum is through the control surfaces I and II (both circular) and III (cylindrical). The radius, r_1, of surface III is chosen much larger than the jet half-width so that, at that radius, the counterflow has a z-direction velocity component in the amount of $u_s(r_1, z)$. This feature is unique to the confined submerged jet where continuity requires a

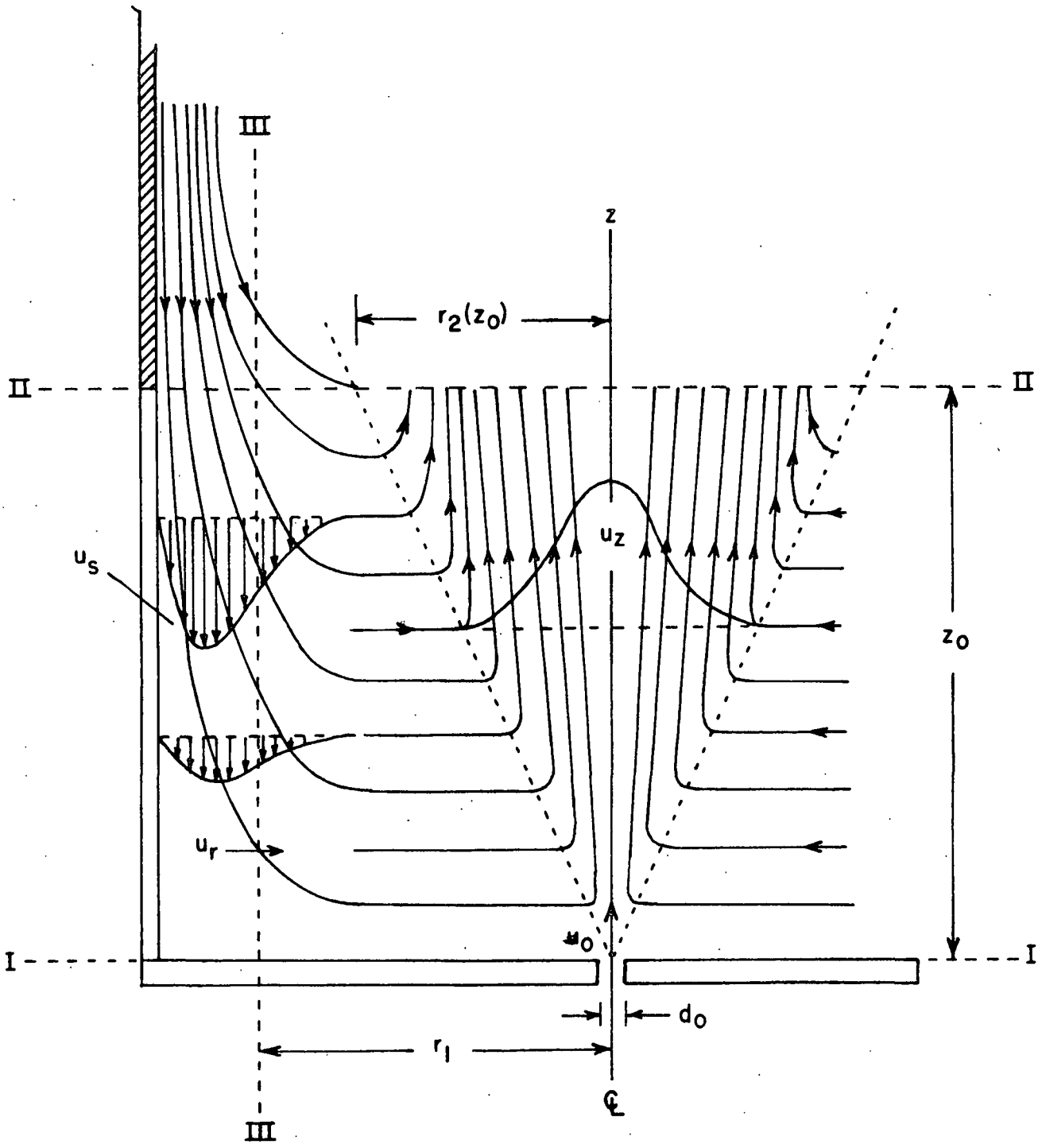

Figure 27. Steamlines in Confined Submerged Jet

counterflow near the wall to provide for the volume of fluid entrained by the jet. At control surface III the flow is complex and u_s at a given point might be positive or negative. No attempt is made to illustrate these flows in Fig. 27.

The z-direction momentum flux (omitting the fluid density, ρ, which remains constant) through surface I is

$$M.F.(I) = \pi/4\ d_o^2\ u_o^2 \tag{84}$$

At surface II, z-direction momentum leaves with the jet flow and enters with the counterflow. The momentum flux is

$$M.F.(II) = 2\pi \int_o^{r_2(z_o)} u_z^2\ r dr = 2\pi \int_{r_2(z_o)}^{r_1} u_s^2\ r dr \tag{85}$$

There is an inward transport of fluid through the cylindrical surface III of differential length dz:

$$2\pi\ r_1\ u_r\ dz, \tag{86}$$

where u_r is the r-direction velocity of the fluid outside of the jet. The z-direction momentum flux at surface III is in the direction of the negative z-axis, so the total flux through surface III is

$$M.F.(III) = -\ 2\pi\ r_1 \int_o^{z_o} u_s(r_1,z)\ u_r(r_1,z)\ dz \tag{87}$$

The value of this integral might be positive or negative.

If the flow is steady and if no external forces act on the fluid within the control surfaces, momentum influx must equal momentum out-flux. This yields

$$\pi/4\ d_o^2 u_o^2 - 2\pi\ r_1 \int_o^{z_o} u_s u_r dz = 2\pi \int_o^{r_2(z_o)} u_z^2 r dr - 2\pi \int_{r_2(z_o)}^{r_1} u_s^2 r dr \tag{88}$$

The momentum in the central jet, where velocity measurements are made, is

$$M(z_o) = 2\pi \int_o^{r_2(z_o)} u_z^2 r dr = \pi/4\ d_o^2 u_o^2 + 2\pi \int_{r_2(z_o)}^{r_1} u_s^2 r dr - 2\pi\ r_1 \int_o^{z_o} u_s u_r dz \quad (89)$$

Although momentum is conserved in the flow within the confining walls, $\underline{M(z)}$ will equal $\underline{M_o}$ only if $\underline{u_s} = 0$. The momentum ratio, $\underline{M(z_o)/M_o}$, will not necessarily equal unity in any experiment where confining walls exist and counterflow is necessary.

A momentum balance similar to Equation (88) may also be derived from Equation (64) for the suspension jet. It is possible, however, that the underlying assumptions of the boundary layer type of equation may not all prove to be valid for the complete flow in the jet tank. After consideration of Fig. 27, Equation (64) is multiplied through by $2\pi\underline{r}$ and integrated with respect to $\underline{r}$ from 0 to $\underline{r_1}$

$$2\pi \left(d/dz \int_o^{r_2(z)} \overline{U^2} r dr - d/dz \int_{r_2(z)}^{r_1} \overline{u_s^2} r dr \right) - 2\pi \int_o^{r_1} R r dr - 2\pi r_1 \overline{UV}(r_1, z) = 0 \quad (90)$$

If Equation (90) is now integrated with respect to $\underline{z}$

$$2\pi \int_o^{r_2(z)} \overline{U^2} r dr = \frac{\pi d^2}{4} U_o^2 + 2\pi \int_{r_2(z)}^{r_1} \overline{u_s^2} r dr - 2\pi r_1 \int_o^z \overline{UV} dz +$$

$$2\pi \int_o^z \int_o^{r_1} R r dr dz, \quad (91)$$

which is Equation (89) with one additional term. For the confined jet, therefore, the two-phase suspension theory also predicts a dependence of the jet momentum on $\underline{z}$, and suggests a dependence on $\underline{R}$, if $\underline{R}$ were nonzero.

In the confined jet there is a definite reason to keep the $\underline{R}$ term, even if it were true that the relative velocity was zero and that ε was constant. Because $\underline{r_1}$ is not known, it might be of interest to set it equal to the inside

jet tank radius, r_i. This can be done only if R includes the viscous shear terms which were neglected when Equation (64) was derived. Near the wall the shear terms would become essential. At $r_1 = r_i$, $\overline{UV}$ is zero and Equation (91) becomes

$$M(z) = 2\pi \int_0^{r_2(z)} \overline{U^2} r dr = \frac{\pi d^2}{4} \overline{U^2} + 2\pi \int_{r_2(z)}^{r_i(z)} \overline{u_s^2} r dr - 2\pi r_i m \int_0^z \left|\frac{\partial u}{\partial r}\right|_{r_i} dz \qquad (92)$$

Again, the conclusion from both Equation (89) and Equation (92) is that the jet momentum in a confined submerged suspension jet does not necessarily equal the initial momentum. Thus, there is a theoretical prediction of the apparent momentum conservation inconsistency discussed earlier, although it is not possible to predict whether actual jet momentum would be larger or smaller than the initial momentum.

Measured Momentum Values

Figure 28 shows values of M/M_o from Table I and Table II plotted against measured distances from the axis for both the water jets and the suspension jets. The accuracy is sufficient so that the difference between the water jet values and the suspension jet values is significant. Also, at a given consistency, the difference between values of M/M_o at different axial distances in a jet is significant, but the difference between the points for the different jets at a given z-distance appears to be insignificant.

Velocity profiles were also measured in one jet (u_o = 475 cm/sec) at four consistencies between zero and 0.75%. These profiles fell between the water jet profiles and the 0.75% consistency jet profiles. The best way to characterize these profiles is with the plot of M/M_o against consistency. These curves indicate that the fibers began to affect the measurements at a consistency of about 0.2% (Fig. 29).

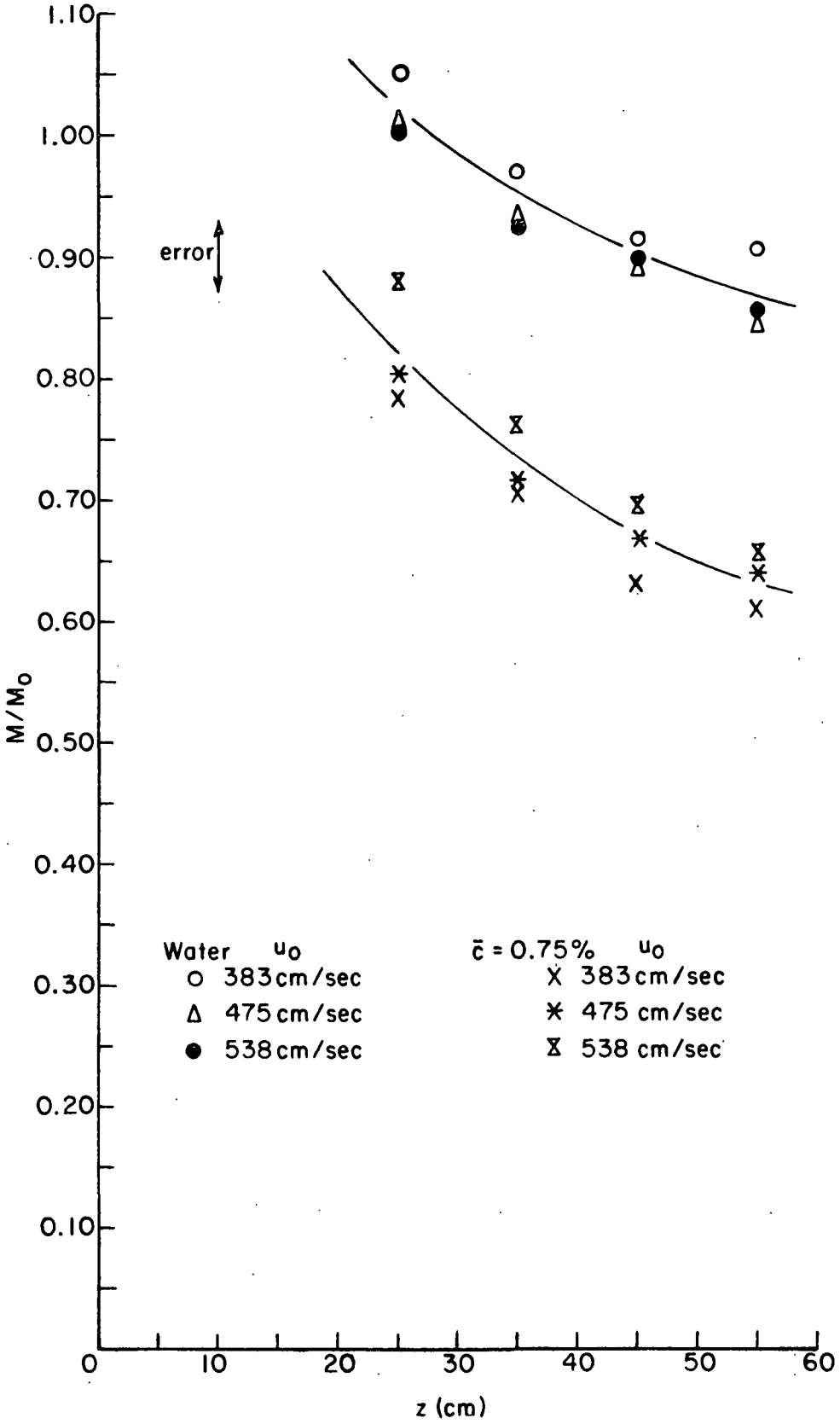

Figure 28. Momentum Ratio of Measured Profiles in Water and in a 0.75% Consistency Suspension of Nylon-12

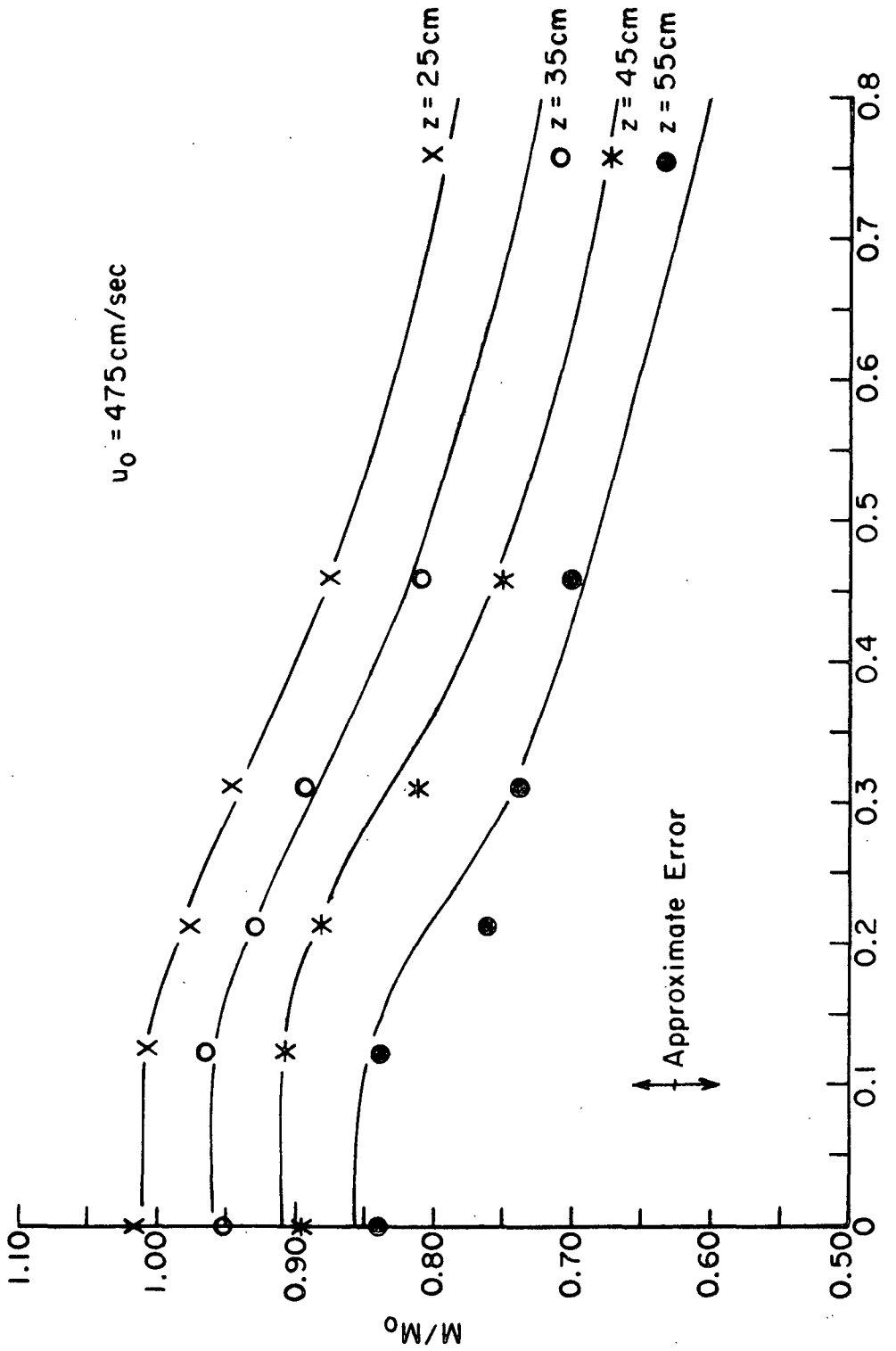

Figure 29. Momentum Ratios

JET CONSISTENCY DISTRIBUTIONS

Local consistency distributions were measured across the jet flow patterns at the four axial distances in the three experimental jets. The consistency distributions all proved to be uniform: the consistency was not a function of r. The magnitude of the fluctuations of the reflected light signal varied across a profile, and the fluctuations near the jet boundary (zero velocity) were too large for accurate readings, but, within the limits of the uncertainty of the measurements, the profiles were flat.

There was a slight increase in the consistency signal with increasing axial distance, and also with decreasing initial velocity. This signal increase appears to be significantly larger than could be attributed to experimental error. A systematic, undetected incongruity in the probe calibration (perhaps its response to changing conditions of turbulence) could have caused these departures from complete uniformity. The differences between points within a given profile (which diminish as z increases) are too small to be significant.

Consistency profiles at 0.73, 0.59, and 0.30% are shown in Fig. 30-32 for the three jets. Profiles measured at consistencies below about 0.3% were completely uniform and showed much smaller fluctuation magnitudes. As the consistency was reduced, the differences between the consistency signals at different axial distances and initial velocities became smaller.

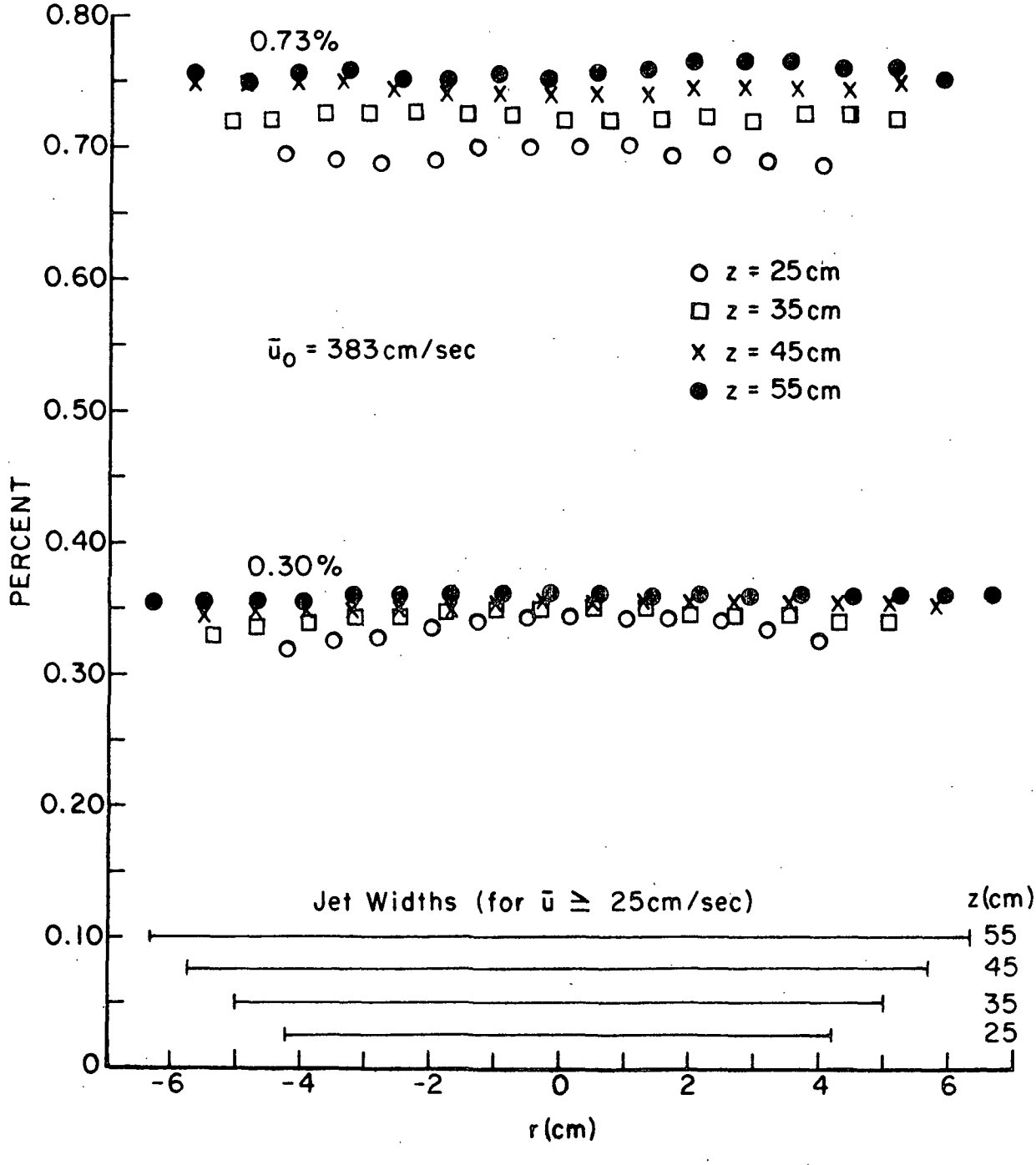

Figure 30. Consistency Distributions

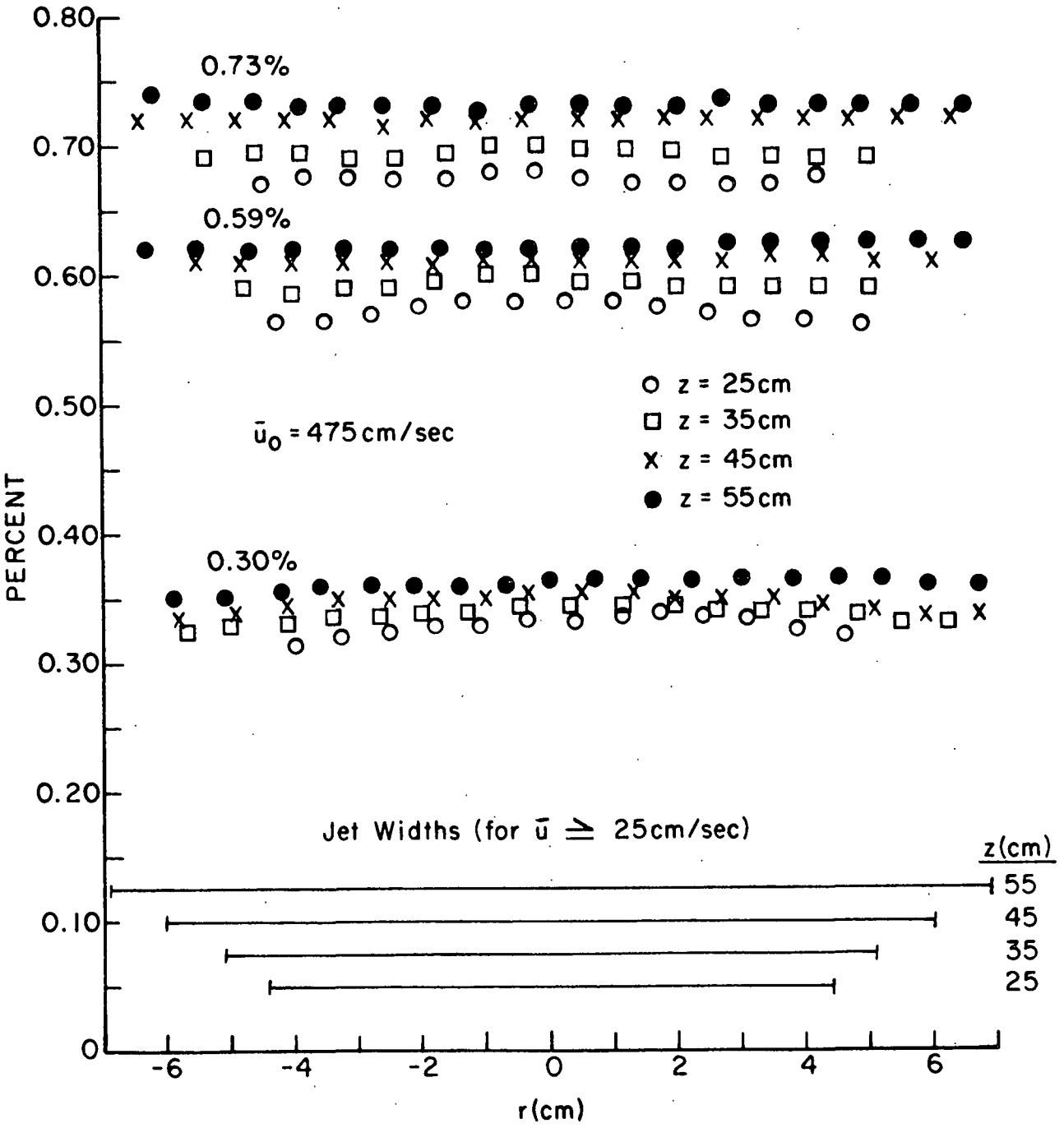

Figure 31. Consistency Distributions

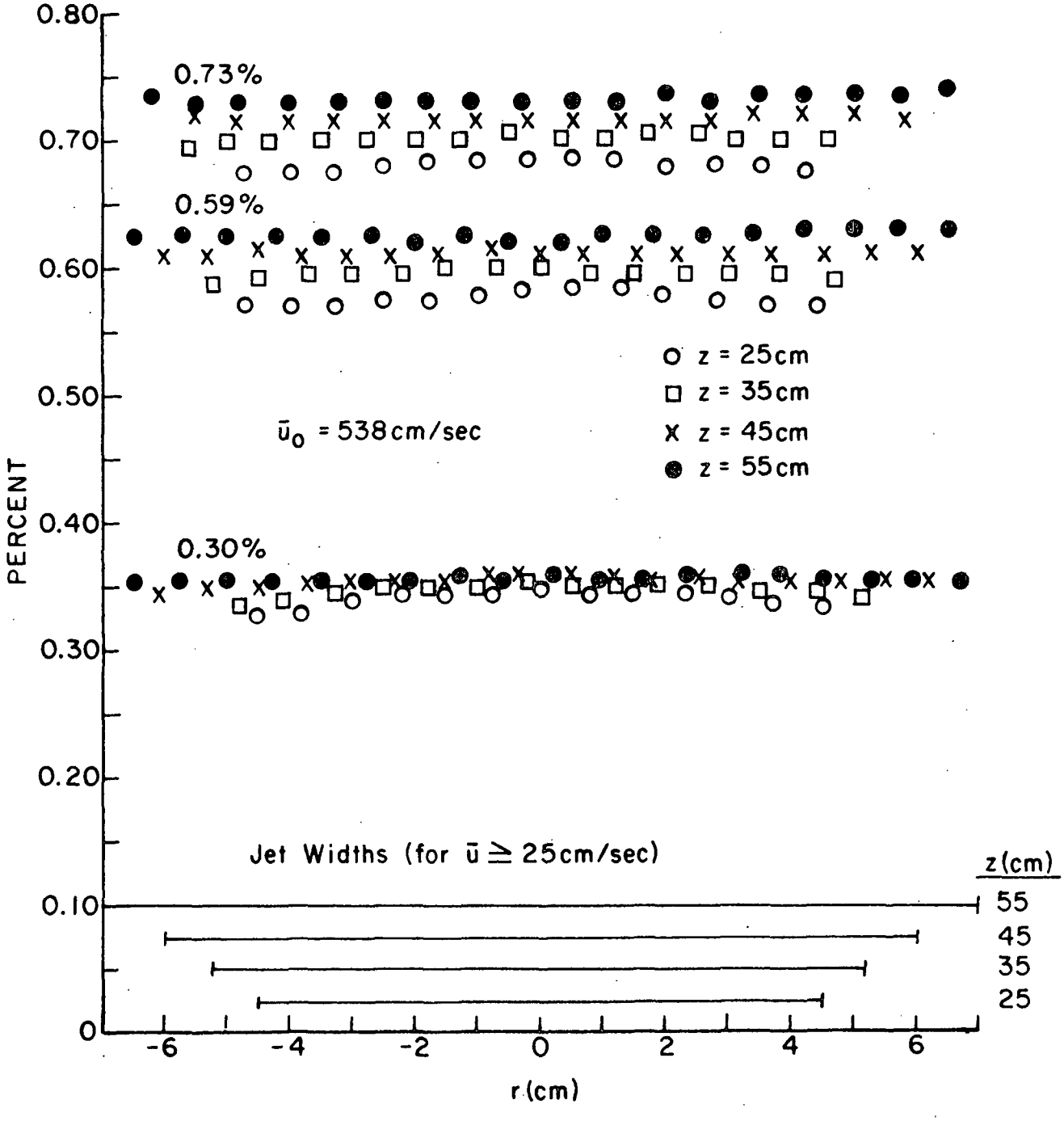

Figure 32. Consistency Distributions

DISCUSSION AND CONCLUSIONS

The suspension jet velocity distributions agree with the new semiempirical suspension jet analysis to the extent that a solution to the equations has been found. Some general characteristics of fiber suspension flow discovered in pipe flow were not found in the jet flow system. In the jet the fibers did not change the reduced shape of the velocity distributions. The momentum transfer was apparently not significantly affected. The measured suspension jet velocity distributions were different from water jet velocity distributions but, in reduced form, they exhibited the same characteristic jet shape that Newtonian fluids do. The distribution of fibers in the jet flow pattern was not dependent on the radial jet coordinate, indicating that the shear stress distribution alone cannot be responsible for nonuniform consistency distributions in turbulent fiber suspension flow.

A secondary conclusion that is important to the understanding of this study is that the confinement of the experimental jet produced a nonideal dependence of the total jet momentum on the axial jet coordinate.

THE EXPERIMENTAL WATER JET

Published experimental studies of water jets were limited in number and scope and did not provide a sufficient base of experimental information for the water-fiber suspension jet studies. Even for the air jets the published results were not consistent. It was necessary, therefore, to establish the properties of the submerged water jet and to test conventional jet assumptions. In particular, all air jet studies made the constant momentum flux assumption but none used their experimental results to attempt to determine the difference between the known initial momentum and the actual measured momentum. There were two possible reasons for this omission: neither of the semiempirical

curves appeared to fit the data well enough to give sufficient accuracy to a calculated momentum ratio, and the poor experimental accuracy at the outside of the jet may have appeared to make graphical integration unreliable. In fact, the present velocity data were used to determine actual momentum by both methods with good accuracy.

The only published jet investigation that did include an actual momentum determination was that by Gaylord (24). He used the error curve formula, Equation (18), and the values of $\bar{u}_m$, r_c, u_o, and d_o to determine M/M_o. The results from his dissertation are given in Table III. (All of Gaylord's basic velocity data were given as values of $\bar{u}/\bar{u}_m$ without ever stating $\bar{u}_m$, itself, so it is not possible to check the calculations of M/M_o.) Gaylord's jet was as confined as the one in this study and the results of the confined jet momentum balance are equally applicable to it.

It is possible to determine the values of M/M_o from other published jet data. Jet velocity results by Trupel, given in detail in the Abramovich text (23), can easily be used to determine M/M_o values in the same way that Gaylord did it, by Equation (83). The Rouse data can also be treated to show the relationship between M/M_o and z (26). Because of the way in which the original data were presented, however, the result is less precise than for the Trupel data. Reichardt did not give the absolute values for u_m (all velocity data are reduced) so only relative M/M_o ratios can be obtained (25). The various computations that led from the published data to the numbers in Table III assumed that either the error curve or the mixing length theory was a good fit to the data. The results in Table III are in general agreement with those presented in Table I and Fig. 28 and with the results of the graphical determination from actual velocity measurements in the present work. Because of their larger volumes of containing fluid, the air jets were generally less confined than the water jets.

TABLE III

JET VELOCITY DATA

Investigators	z/d_o	r_c/z	M/M_o
Gaylord (1/4-inch nozzle) (24)	9.45	0.113	1.360
	12.6	0.101	1.240
	17.3	0.091	1.040
	20.5	0.090	1.030
	30.0	0.092	1.110
Gaylord (3/8-inch nozzle) (24)	10.0	0.097	1.130
	15.0	0.089	1.090
Trupel-Abramovich (23)	6.67	0.110	1.12
	8.89	0.096	1.01
	11.11	0.092	0.96
	13.33	0.094	0.96
	17.78	0.093	0.95
Albertson, Dai, Jenson, and Rouse (26)	16.0	0.103	1.17
	32.0	0.101	1.13
	64.0	0.097	1.05
Reichardt (25)	13.3	0.084	1.10[a]
	17.4	0.084	1.01[a]
	30.0	0.084	0.89[a]

[a]Based on M/M_o = 1.10 at z/d_o = 13.3 as an arbitrary reference.

A simple analysis shows the dependence of M/M_o on the two apparent locations, a_u and a_r, of the pole of the main region of the jet. Equations (79) and (80) can be combined to give

$$u_m r_c = \frac{C_u u_o}{C_r} \left(\frac{z+a_r}{z+a_u} \right) \tag{93}$$

Substitution of Equation (93) into Equation (83) yields

$$M/M_o = \frac{C_u}{1.178\ r_o\ C_r} \left(\frac{z+a_r}{z+a_u} \right) \tag{94}$$

If $a_r = a_u$, or if a_r and a_u are negligibly small with respect to z, then M/M_o does not depend on z. In most experimental jets, however, a_r and a_u are not equal and are significantly larger than zero so that M/M_o does depend on z.

Gaylord determined a value for a_u from a least-squares fit to Equation (80). His average value was $a_u = 0.31\ d_o$. In comparison, the a_u values of Table I range from $0.30\ d_o$ to $0.85\ d_o$. Gaylord did not give a value for a_r, but an approximate mean value for his jet is $a_r/d_o = 4$. This compares to the values in Table I of $a_r/d_o = 2.26$, 2.42, and 3.12 for the three water jets.

Abramovich stated that "in an axially symmetric jet the position of the pole, found from the axial velocity, differs from the position determined from the radial line equal to half the axial velocity." He did not mention, however, that this implies a value of M/M_o that is dependent on z. Abramovich said that the best value from Trupel's data for the apparent pole location was $a_u = 1.9\ d_o$. This value falls between the a_u and a_r values for the water jets.

It is clear that the present experimental jet is much like those that have been investigated previously. The principle of conservation of jet momentum flux can hold only approximately within these real jet flows. As

total axial momentum decreased with increasing z, both u_m and r_c dropped below their ideal values. The dependence of M/M_o on z was caused by the velocity, u_s, of the return flow loops. Because the relationship between u_s and r is not known, the experimental values of $M(z)$ cannot be used to determine u_s from Equation (89). It is clear, however, that the last two terms of Equation (89) are not zero for the present experimental jet:

$$2\pi \left[\int_{r_2}^{r_1} u_s^2 r dr - r_1 \int_0^{z_o} u_s u_r dz \right] \neq 0 \qquad (95)$$

SUSPENSION JET VELOCITY PROFILES

As Fig. 21 shows, the suspension jet velocity profiles are similar, so that there should be a universal solution of Equation (71). To obtain such a solution two assumptions must be made to eliminate z-dependence from the equation. First, $\mathcal{L}(z+a)$ must be a linear function of $(z+a)$:

$$\mathcal{L} = \lambda(z+a) \qquad (96)$$

Then, R must either be an inverse function of $(z+a)^3$ or be set equal to zero. The first alternative does not make physical sense but the second is not appealing either because of the apparent importance of the terms of R in the suspension analysis. Therefore, R could be retained temporarily for a complete solution of Equation (71) and perhaps be set equal to zero later. For convenience, R is expressed

$$R = [-m_o^2 d_o^2 u_o^2/(z+a)^3]\ \phi, \qquad (97)$$

where ϕ is a constant.

Now Equation (71) can be integrated, yielding

$$f = (1-\phi/2)\ \exp(-1/2\lambda\ \eta^2) + \phi/2, \qquad (98)$$

which is a modification of the error law equation. Equation (70) can then be written using Equation (98)

$$\overline{U^2} = U^{*2} = \left(\frac{m_o u_o d_o}{(z+a)}\right)^2 [(1-\phi/2)\ \exp(-1/2\lambda\ \eta^2) + \phi/2], \qquad (99)$$

and the equation for $\underline{U}^*$ becomes

$$U^* = \frac{m_o u_o d_o}{(z+a)} [(1-\phi/2)\ \exp(-1/2\lambda\ \eta^2) + \phi/2]^{1/2} \qquad (100)$$

The velocity $\underline{U}^*$ must be zero at infinitely large radial distance. Inspection of Equation (100) shows that $\underline{U}^*$ cannot become zero as η becomes infinite unless ϕ is zero. This conclusion simply means that $\underline{R}$ should have been set equal to zero for the solution of Equation (71). For $\underline{R} = 0$, Equation (98) becomes

$$f = \exp(-1/2\lambda\ \eta^2), \qquad (101)$$

and the solution for $\underline{U}^*$ is

$$U^* = \frac{m_o u_o d_o}{(z+a)}\ \exp(-1/4\lambda\ \eta^2) \qquad (102)$$

Equation (60) defines the velocity, $\underline{U}^*$, approximately, as

$$U^* \approx \overline{\varepsilon}(\overline{u^2}+\overline{u'^2})^{1/2} + \overline{\varepsilon' u'}/(1+\overline{u'^2}/\overline{u^2})^{1/2} \qquad (103)$$

This velocity is to be compared to that determined from dynamic pressure measurements made in the jet flow. This dynamic pressure measured in a turbulent flow is $(\rho_\Lambda/2)[\overline{\varepsilon^2}(\overline{\underline{u}^2}+\overline{\underline{u}'^2})]$. Turbulence measurements in air jets showed that although the mean square fluctuation velocity, $\overline{\underline{u}'^2}$, was an order of magnitude smaller than $\overline{\underline{u}^2}$ near the center of the jet, it was commensurate with it near the jet boundary. Therefore, the measured velocity profiles represented the distribution of $\overline{\varepsilon}(\overline{\underline{u}^2}+\overline{\underline{u}'^2})^{1/2}$ across the jet. The factor $\overline{\varepsilon'\underline{u}'}$ in Equation (103) is not related to the dynamic pressure. It cannot be sensed by the pitot tube.

The velocity described by Equation (103) was derived from the equation for the change of total momentum. This includes momentum transport due to turbulent mass flux of the fiber phase, $\overline{\varepsilon' \underline{u}'}$. If this cannot be measured, an equation for the distribution of measured velocity must be

$$U = \overline{\varepsilon}(\overline{u^2+u^{\cdot 2}})^{1/2} = \frac{m_o u_o d_o}{(z+a)} \exp(-1/4\lambda\ \eta^2) - \overline{\varepsilon' u'}/(1+\overline{u'^2}/\overline{u^2})^{1/2} \qquad (104)$$

The probable sign of $\overline{\varepsilon' \underline{u}'}$ can be predicted if certain physical hypotheses about ε' and $\underline{u}_\lambda'$ are accepted. Consider the solid fraction, $\underline{c} = 1 - \varepsilon$. At any point in the suspension, if $\underline{c}$ drops below the mean solid fraction, $\overline{\underline{c}}$, then $\underline{c}'$ is negative. At this same point in the flow, the velocity, $\underline{u}_\lambda$, should be higher than its mean value, $\overline{\underline{u}}_\lambda$, because a low local consistency develops by local concentration of the water phase. The velocity fluctuation, $\underline{u}_\lambda'$, is then positive and the correlation, $\overline{\underline{c}' \underline{u}_\lambda'}$, is negative. In the opposite case, a positive $\underline{c}'$ should occur simultaneously with a negative $\underline{u}_\lambda'$ and $\overline{\underline{c}' \underline{u}_\lambda'}$ is again negative. Therefore,

$$\overline{\varepsilon' u_\lambda'} = -\left(-\left|\overline{c' u_\lambda'}\right|\right) = \left|\overline{c' u_\lambda'}\right| \qquad (105)$$

might well usually be positive when these assumptions are roughly correct. The value of $\overline{\varepsilon' u_\lambda'}$ remains unpredictable.

The two constants, $\underline{m_o}$ and λ, are not functions of ε and could be determined from water jet results. It is possible to determine values for the term $\overline{\varepsilon' \underline{u}'}/(1+\overline{\underline{u}'^2}/\overline{\underline{u}^2})^{1/2}$ from the data and Equation (104) and to observe the dependence of the function on $\underline{r}$ and $(\underline{z}+\underline{a})$.

Since

$$m_o u_o d_o/(z+a) = \overline{u}_m,$$

as determined in Table I, a value of $\underline{m_o}$ would be easily obtained. It is convenient, however, to revert to the general form

$$\bar{u}/\bar{u}_m = \exp(-1/4\lambda\ \eta^2) \tag{106}$$

Because the experimental water jets fitted the curve described by Equation (18), it is possible now to express λ in those terms:

$$\lambda = \frac{1}{4(0.694)}\,[r_c/(z+a)]^2 \tag{107}$$

Values of the constant, $[\underline{r_c}/(\underline{z}+\underline{a})]$, are determined for the jets in Table I and λ can be calculated directly.

Equation (104) is finally written in terms of these measured variables

$$U = u_m[\exp(-0.694(r/r_c)^2)] - \overline{\varepsilon' u'}/(1+\overline{u'^2}/\overline{u^2})^{1/2}, \tag{108}$$

where $\underline{u_m}$ is the centerline velocity of the water jet. If $\overline{\varepsilon' \underline{u}'}$ and $\overline{\underline{u}'^2}$ were known by theory or experiment, then Equation (108) would predict suspension velocity distributions.

Table IV shows calculated values of the reduced form

$$\varepsilon = (\overline{\varepsilon' u'}/\bar{u}_m)/(1+\overline{u'^2}/\overline{u^2})^{1/2}$$

from Equation (108) for the jet with $\underline{u_o}$ = 475 cm/sec at 0.75% consistency. Figure 33 illustrates these values as a function of $\underline{r}/\underline{r_o}$. Because $\overline{\underline{u}'^2}/\underline{u}^2$ cannot be measured with the velocity probe, it is not possible to determine $\overline{\varepsilon' \underline{u}'}$, either.

In conclusion, the measured velocities in the suspension jet are lower than the corresponding velocities in the water jet with equal initial momentum. Suspension flow theory shows that this difference is due to a turbulent mass flux term, $\overline{\varepsilon' \underline{u}'}$. Because of the resulting unmeasured contribution to the total jet momentum, the momentum flux at a suspension jet profile is smaller than that in the corresponding water jet.

TABLE IV

EXPERIMENTAL VALUES OF $\varepsilon = (\overline{\varepsilon' u'}/u_m)/(1+\overline{u'^2}/\overline{u^2})^{1/2}$

FOR SUSPENSION JET WITH 0.75% CONSISTENCY

s = 25 cm, u_m = 244 cm/sec		s = 35 cm, u_m = 180 cm/sec		s = 45 cm, u_m = 140 cm/sec		s = 55 cm, u_m = 116 cm/sec	
r/r_c	ε	r/r_c	ε	r/r_c	ε	r/r_c	ε
-1.79	0.001	1.58	0.010	-1.50	0.024	1.35	0.023
-1.65	0.003	1.29	0.026	-1.30	0.016	1.22	0.020
-1.51	0.004	0.95	0.030	-1.16	0.022	1.12	0.040
-1.29	0.008	0.81	0.034	-1.00	0.029	0.98	0.047
-1.13	0.027	0.63	0.048	-0.86	0.042	0.88	0.050
-1.01	0.034	0.46	0.052	-0.71	0.048	0.77	0.051
-0.84	0.039	0.27	0.057	-0.56	0.047	0.62	0.050
-0.66	0.059	0.11	0.064	-0.43	0.059	0.49	0.045
-0.44	0.063	-0.02	0.067	-0.34	0.059	0.39	0.047
-0.28	0.066	-0.16	0.065	-0.23	0.057	0.24	0.055
-0.16	0.056	-0.36	0.064	-0.08	0.060	0.11	0.052
-0.04	0.056	-0.52	0.057	0.09	0.058	0.01	0.060
0.12	0.056	-0.66	0.050	0.21	0.066	-0.14	0.064
0.28	0.058	-0.81	0.040	0.33	0.056	-0.27	0.063
0.46	0.047	-0.96	0.034	0.47	0.051	-0.39	0.055
0.66	0.050	-1.09	0.032	0.58	0.049	-0.49	0.063
0.80	0.043	-1.26	0.021	0.76	0.041	-0.66	0.049
0.99	0.036	-1.39	0.018	0.86	0.035	-0.77	0.051
1.17	0.018	-1.55	0.017	1.01	0.029	-0.94	0.016
1.29	0.024			1.16	0.022	-1.10	0.027
1.39	0.020			1.29	0.022	-1.24	0.008
1.53	0.008			1.43	0.006	-1.39	0.003
1.65	0.008			1.52	0.015	-1.50	0.003

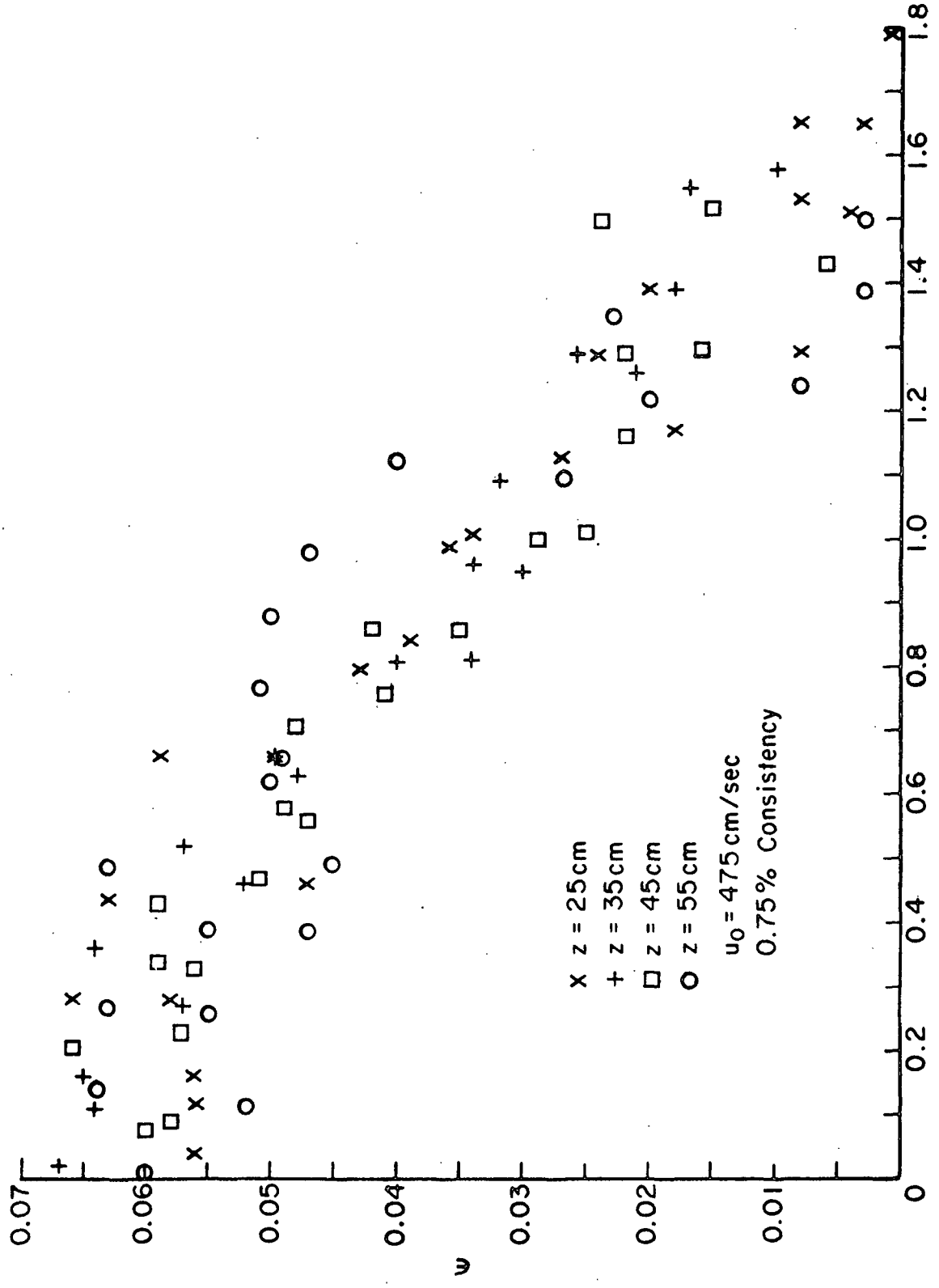

Figure 33. Dependence of $\frac{\overline{\varepsilon' u'}/\bar{u}_m}{(\overline{1+u'^2}/\overline{u^2})^{1/2}} = \varepsilon$ on r/r_c

Over the lower range of measured values, however, $\underline{M}/\underline{M}_o$ has the same relationship to $\underline{z}$ that it does in the experimental water jet. The momentum ratio of the suspension jet decreases steadily as $\underline{z}$ increases. Again, this phenomenon is due to return flow loops in the confining tank and can be characterized with the two apparent locations of the virtual pole of the main jet region. The value of $\underline{a}_u$ from Fig. 26 (and found in Table II) is not significantly different from that for the corresponding water jet. This indicates that $\underline{a}_u$ is a valuable parameter with which to characterize the experimental jet flow system itself, as previous investigators suggest. The value of $\underline{a}_r$, however, is significantly larger in the suspension jet than in the corresponding water jet. The difference between $\underline{a}_r$ and $\underline{a}_u$ is directly related to the magnitude of the measured momentum "loss," the momentum contribution of $\overline{\varepsilon' \underline{u}'}$.

Finally, it is found that the shape of the reduced jet velocity profiles are not affected by the fibers in the suspension. This lack of difference in the shape of the profiles makes the difference in momentum flux especially important for without it the profiles would be indistinguishable.

SUSPENSION JET CONSISTENCY PROFILES

The consistency measurements showed that the correct solution to a consistency distribution equation for the jet would have been $\underline{\bar{c}}$ = constant. This solution is consistent with Equations (72)-(75).

There are apparent incongruities in the measured consistency signal profiles. The probe signal increased as axial distance increased. At high bulk consistency the signals in the slowest jet ($\underline{u}_o$ = 383 cm/sec) indicated a consistency higher than the known bulk consistency.

Since there would not be an axial consistency gradient unless there was a radial gradient, or perhaps an extremely large relative velocity, these inconsistencies must be attributed to a systematic experimental error. The consistency probe is not well enough understood for the effect of turbulence (or other flow variables) on the signal to be entirely known. The evidence here suggests that a lower turbulence intensity (declining as $\underline{z}$ increases) might have produced higher signals. The consistency calibration system flow was probably highly turbulent. Note that it is at $\underline{u_o}$ = 538 cm/sec and $\underline{z}$ = 25 cm that the consistency probe signal and bulk system consistency agree with the consistency calibration curve (Fig. 16). There are slightly low consistency signals near the boundary of some profiles. It is likely that the probe does not function well at high consistency and very low velocity. As Fig. 15 shows, the purge water plateau disappears at low velocities. Also at the jet boundary the suspension velocity vector is at a slight angle to the probe which could cause the purge jet water to come directly into the sensing volume of the probe.

Time-mean fiber distributions in suspension flow are not made nonuniform by the action of the shear stresses as they may have been in pipe flow experiments. The two-phase theoretical treatment of turbulent pipe flow led to an equation that supports these results found in the system. There was nothing in the theory, however, to suggest physical mechanisms for the influences of shear rate on the fiber distribution. The jet results indicate that, in fact, shear rate does not influence fiber distribution.

The jet consistency distributions show that, in general, the presence of shear stresses (a nonuniform mean velocity distribution) alone does not create a nonuniform mean consistency distribution. It is possible that particular velocity distributions (for example, that of pipe flow) or the influences of

solid walls are necessary for a nonuniform fiber distribution. These conclusions will be important in future study and design of fiber suspension flow systems where fiber distribution are of interest.

SUGGESTIONS FOR FUTURE WORK

Any future work in this field must be postponed until an exhaustive scientific study is made of the purged optical consistency probe. It must be analyzed theoretically and experimentally. The calibration loop used in the present study provides a starting point for this work, although it would require extensive design improvements. A truly scientific understanding of the flow of water and fibers around the probe tip and of the optical behavior of the light reflected from the suspension must be realized.

The present jet tank flow system could be used to study suspensions of other sizes of nylon-12 fibers if more nylon-12 is ever available. Measurements of jet momentum loss could be used to characterize suspensions of fibers with different diameters and lengths. Some information might be obtained from wood fiber suspensions in the jet if the experiments were designed to tolerate a vertical consistency gradient and a bed of fibers on the tank baseplate. If the jet tank system is ever used again, I recommend that the mixing tank be moved up to the level of the top surface of the jet tank. This would eliminate a free dropleg, and a valve, and make continuous operation of the system by one person practical.

I repeat Sanders' suggestion that fibers of different substances in different sizes be studied in suspension flow, specifically in tube flow where settling will not occur. The importance of wall effects on the consistency distribution could be determined by using pipe loops of different diameters.

The continuous chart recording of impact pressures, for velocity profiles, and of the consistency signals is an advancement in suspension flow research. It is valuable for accurate measurements of local mean quantities and should be used in future suspension flow investigations unless measurement of turbulent fluctuations is necessary.

NOMENCLATURE

A_t = Boussinesq turbulent viscosity (L^2T^{-1})

a = viscous flow resistance coefficient (L^{-2})

a = distance from plane of jet nozzle to pole of main jet region (L)

a_u = value of a (pole distance) based on values of u_m (L)

a_r = value of a (pole distance) based on values of r_c (L)

B, B_* = dimensionless constants in universal logarithmic pipe flow equation

b = jet width, often r at which $\bar{u} = 0.01\ \bar{u}_m$ (L)

C_λ = dimensionless constant of integration for two-phase pipe flow

C_u = jet constant relating $z+a_u$ to u_m/u_o (L)

C_r = jet constant relating $z+a_r$ to r_c, dimensionless

c = volume fraction of fibers in suspension, dimensionless

D = cylindrical fiber diameter, wood fiber width (L)

D_i = drag force between fibers and water in suspension $(ML^{-2}T^{-2})$

d_o = initial jet (nozzle exit) diameter (L)

$F_{\lambda i}$ = interaction force exerted by fibers on water $(ML^{-2}T^{-2})$

f = dimensionless velocity function for suspension jet flow

f, g = arbitrary dimensionless distribution functions

g = gravitational acceleration (LT^{-2})

H = manometer meniscus level difference (L)

h = depth of suspension in mixing tank (L)

L = fiber length (L)

M = total jet momentum rate divided by fluid density (L^4T^{-2})

M_o = initial jet momentum rate divided by fluid density (L^4T^{-2})

m_o = dimensionless empirical jet constant, $m_o = (U_m/U_o d_o)(z+a)$

m = empirical jet constant, $m = \bar{u}_m(z+a)$ (L^2T^{-1})

n = normal probability density, dimensionless

$\underline{p}$ = total pure fluid (or mixture) pressure $(ML^{-1}T^{-2})$

$\underline{p}_\Lambda$ = true water pressure, measured by static tube $(ML^{-1}T^{-2})$

$\underline{p}_\lambda$ = apparent water pressure in suspension $(ML^{-1}T^{-2})$

$\underline{p}_\Phi$ = true fiber pressure $(ML^{-1}T^{-2})$

$\underline{p}_\phi$ = apparent fiber pressure in suspension $(ML^{-1}T^{-2})$

$\underline{p}_s$ = total mean suspension stagnation pressure $(ML^{-1}T^{-2})$

$\Delta\underline{p}$ = impact pressure at probe tip $(ML^{-1}T^{-2})$

$\underline{R}$ = pipe radius (L)

$\underline{R}$ = $\underline{r}/\underline{r}_c$, dimensionless

$\underline{R}$ = right hand side of Equations (57) and (64) (LT^{-2})

$\underline{Re}$ = Reynolds number, dimensionless

$\underline{r}$ = jet radial coordinate, jet radial distance

$\underline{r}_1$ = distance from axis to plane III — confined jet analysis (L)

$\underline{r}_2$ = distance from axis to jet boundary at plane II in confined jet (L)

$\underline{r}_o$ = jet nozzle radius, initial jet radius (L)

$\underline{r}_c$ = radial distance at which $\bar{\underline{u}}/\bar{\underline{u}}_m = 0.5$ (L)

$\underline{r}_i$ = inside radius of jet tank (L)

$\underline{s}$ = radial distance from tube wall (L)

$\underline{s}_o$ = fiber-free boundary thickness in a pipe (L)

$\underline{s}^+$ = dimensionless pipe wall distance, $\underline{s}^+ = \underline{s}\rho\underline{v}_*/\mu$

$\underline{t}$ = time (T)

$\underline{T}$ = time duration of time-smoothing in turbulent flow analysis (T)

$\underline{U}$ = $\overline{\varepsilon U}$, superficial suspension velocity (LT^{-1})

$\underline{U}^*$ = root-mean-square of superficial velocity, $\underline{U}$ (LT^{-1})

$\underline{u}$ = pure fluid or mixture longitudinal jet velocity (LT^{-1})

$\underline{u}_o$ = initial jet velocity (LT^{-1})

$\underline{u}_m$ = centerline longitudinal (axial) jet velocity (LT^{-1})

$\underline{u}_r$ = velocity of return flow in confined jet perpendicular to axis (LT^{-1})

$\underline{u}_s$ = velocity of return flow in confined jet parallel to axis (LT^{-1})

$\underline{u}_{rel}$ = relative velocity between fiber and water (LT^{-1})

$\underline{u}_z$ = axial velocity in confined jet analysis (LT^{-1})

$\underline{V}$ = $\overline{\varepsilon V}$, superficial suspension radial velocity (LT^{-1})

$\underline{v}_i$, $\underline{v}_j$ = local velocities in a general orthogonal system (LT^{-1})

$\underline{v}_{\lambda i}$ = average of microscopic water velocities (LT^{-1})

$\underline{v}_{\phi i}$ = average of microscopic fiber velocities (LT^{-1})

$\underline{v}_{rel}$ = relative velocity between water and fibers (LT^{-1})

$\underline{v}^+$ = pipe flow dimensionless velocity, $\underline{v}^+ = \underline{v}/\underline{v}_*$

$\underline{v}_*$ = pipe flow friction velocity, $\sqrt{\tau_o/\rho}$ (LT^{-1})

$\underline{w}'$ = angular jet velocity fluctuation (LT^{-1})

$\underline{x}_i$, $\underline{x}_j$ = general orthogonal coordinates (L)

$\underline{x},\underline{y},\underline{z}$ = general variables, rectangular coordinates (L)

$\underline{z}$ = jet axis, axial distance from jet orifice (L)

$\underline{z}_o$ = distance from plane II to plane I in confined jet analysis (L)

$\underline{\ell}$ = Prandtl's mixing length (L)

$\mathcal{L}$ = mass transfer length in suspension velocity distribution (L)

$\mathscr{D}$ = constant diffusivity coefficient (L^2T^{-1})

$\mathscr{D}_t$ = a semiempirical "turbulent diffusivity" (L)

ε = $(\overline{\varepsilon'\underline{u}'})/(1+\overline{\underline{u}'^2}/\overline{\underline{u}^2})^{1/2}$, dimensionless

ε = volume fraction of water in suspension, dimensionless

η = independent dimensionless jet variable, $\eta = \underline{r}/(\underline{z}+\underline{a})$

κ = von Karman constant, dimensionless

κ_* = apparent von Karman constant for suspensions, dimensionless

κ' = dimensionless constant in Prandlt free turbulence theory

κ_ϕ, κ_λ = pipe flow mixing length distribution parameters, dimensionless

Λ, λ = subscripts, denoting true and apparent water quantities

λ = constant in solution of suspension jet equation, dimensionless

μ = viscosity for pure fluid $(ML^{-1}T^{-1})$

ξ = radial jet variable, $\xi = \sigma \underline{r}/(\underline{z}+\underline{a})$, dimensionless

$\xi_{\underline{c}}$ = $\sigma \underline{r}_{\underline{c}}/(\underline{z}+\underline{a})$, dimensionless

ρ = pure fluid or suspension density (ML^{-3})

ρ_{Λ} = true water density (ML^{-3})

ρ_{λ} = apparent water density in fiber suspension (ML^{-3})

ρ_{Φ} = true fiber density (ML^{-3})

ρ_{ϕ} = apparent fiber density (ML^{-3})

σ = empirical jet constant, $\xi = \sigma \underline{r}/(\underline{z}+\underline{a})$, dimensionless

τ = laminar shear stress $(ML^{-1}T^{-2})$

τ_{λ} = apparent laminar water shear stress in suspension $(ML^{-1}T^{-2})$

τ_{ϕ} = apparent laminar fiber shear stress in suspension $(ML^{-1}T^{-2})$

$\tau_{\underline{o}}$ = pipe flow wall shear stress $(ML^{-1}T^{-2})$

Φ , ϕ = subscripts, denoting true and apparent fiber quantities

ϕ = empirical coefficient for suspension jet velocity profiles, dimensionless

Note: The use of an overbar in the text denotes the time-mean value of a fluctuating turbulent variable. The use of a prime denotes the time-dependent fluctuations of the variable.

ACKNOWLEDGMENTS

Mr. Heribert Meyer, the Chairman of my Thesis Advisory Committee, was the instigator of, and counselor during, this research experience. The theoretical treatment is his. Without his help there would be no thesis. I also wish to acknowledge the advice and help of the other members of my advisory committee, Dr. Richard W. Nelson and Dr. Thomas M. Grace.

The engineering of the large-scale equipment was in large part done by Mr. Robert Rae, and it was built under his direction by the Institute Millwright shop. The Institute Machine Shop designed and built much of the rest of the equipment. The creative talents of Mr. Filz and Mr. Van Rossum made possible the continuous refinements of the apparatus that finally permitted its successful operation.

Mr. Keith Hardacker designed the optical and electronic equipment for the consistency measurements. Mr. Bruce Andrews and Mr. Orlin Kuehl were the invaluable sources of information about the experimental details of the work of preceeding students. Mr. Andrews also contributed the flowmeter, TRX-100, the pressure transducers, and the chart recorder at times in the work where failure had seemed imminent.

I wish to thank Dr. Glen A. Nesty of the International Paper Company for his successful search of Europe for my precious nylon-12 monofilament.

Finally, I acknowledge the help of my wife and laboratory assistant, Judy. There were many times when the overgrown jet flow system could not be controlled by one person. Together we did control it and with the help of many others, forced the jet to grudgingly release the information I sought.

LITERATURE CITED

1. Sanders, H. T., Jr. and Meyer, H., Tappi 54:722(1971).

2. Meyer, H., Tappi 54:1426(1971).

3. Nelson, R. W., Tappi 47:752(1964).

4. Emmons, H. W., Tappi 48:679(1965).

5. Sanders, H. T., Jr. An investigation of fiber consistency distributions in turbulent tube flow. Doctoral Dissertation. Appleton, Wisconsin, The Institute of Paper Chemistry, 1970.

6. Baldwin, P. C. and Van den Acker, J. A., Paper Trade J. 109(12)(Sept. 21, 1939).

7. Robertson, A. A. and Mason, S. G., Pulp Paper Mag. Can., Convention Issue: 263(1957).

8. Hubley, C. E., Robertson, A. A., and Mason, S. G., Can. J. Res. 28, section B:770(1950).

9. Daily, J. W. and Bugliarello, G., Tappi 44:497, 881(1961).

10. Ippen, A. T., Daily, J. W., and Bugliarello, G., Tappi 40:478(1957).

11. Mih, W. and Parker, J., Tappi 50:237(1967).

12. Robertson, A. A. and Mason, S. G., Tappi 40:326(1957).

13. Forgacs, O. L., Robertson, A. A., and Mason, S. G., Pulp Paper Mag. Can. 59(5):117(1958).

14. Seely, T. L. Turbulent tube flow of dilute fiber suspensions. Doctoral Dissertation. Appleton, Wisconsin, The Institute of Paper Chemistry, 1968.

15. Daily, J. W., Bugliarello, G., and Troutman, W. W., M.I.T. Hydrodynamics Report No. 35. Cambridge, Massachusetts, Mass. Inst. Tech., 1959.

16. Bobkowicz, A. J. and Gauvin, W. H., Can. J. Chem. Eng. 43:87(1965).

17. Bobkowicz, A. J. and Gauvin, W. H., Chem. Eng. Sci. 22:229(1967).

18. Norman, B., Nerelius, L., and Wahren, D. Measurement of flocculation characteristics by light reflection, I. Paper presented at the 26th TAPPI Engineering Conf., 1971.

19. Appel, D. W. Measurement of flocculation characteristics by light reflection, II. Paper presented at the 26th TAPPI Engineering Conf., 1971.

20. Persinger, W. H. Scale of flocculation for fully developed turbulent tube flow of dilute fiber suspensions. Doctoral Dissertation. Appleton, Wisconsin, The Institute of Paper Chemistry, 1974.

21. Schlichting, H. Boundary layer theory. 4th ed. Trans. J. Kestin. New York, McGraw-Hill, 1960.

22. Townsend, A. A. The structure of turbulent shear flow. Cambridge, University Press, 1956.

23. Abramovich, G. W. The theory of turbulent jets (trans. scripta technica). Cambridge, Mass., The M.I.T. Press, Mass. Inst. Tech., 1963.

24. Gaylord, E. W. Momentum and mass transfer in water for a submerged axially symmetric jet. Doctoral Dissertation. Pittsburg, PA, Carnegie Inst. Tech., 1953.

25. Reichardt, H. VDI — Forschungsheft, 1942:414.

26. Albertson, M. L., Dai, Y. B., Jensen, R. A., and Rouse, H., Trans. ASCE 115(2409):639-97(1950).

27. Citrini, D., Trans. ASCE 115:671-5(1950).

28. Kiser, K. M., AIChE J. 9(3):387(1963).

29. Bird, R. B., Stewart, W. E., and Lightfoot, E. N. Transport phenomena. New York, John Wiley and Sons, 1960.

30. Hinze, J. O. Turbulence. New York, McGraw-Hill, 1959.

31. Carrasquilla, A. B. Flow of suspensions of rigid, nonspherical particles. Masters Dissertation. Cambridge, Mass., Mass. Inst. Tech., 1965.

32. Griehl, W. and Ruestem, D., Ind. Eng. Chem. 62(3):16-22(1970).

APPENDIX I

PUBLISHED AIR JET DATA

These submerged air jet results selected from the literature show the fit of the error curve to the data and give an idea of the scatter of the experimental points. All points had to be read from graphical presentations and some then had to be transformed into compatible terms of u/u_m and r/r_c (see Fig. 34-36).

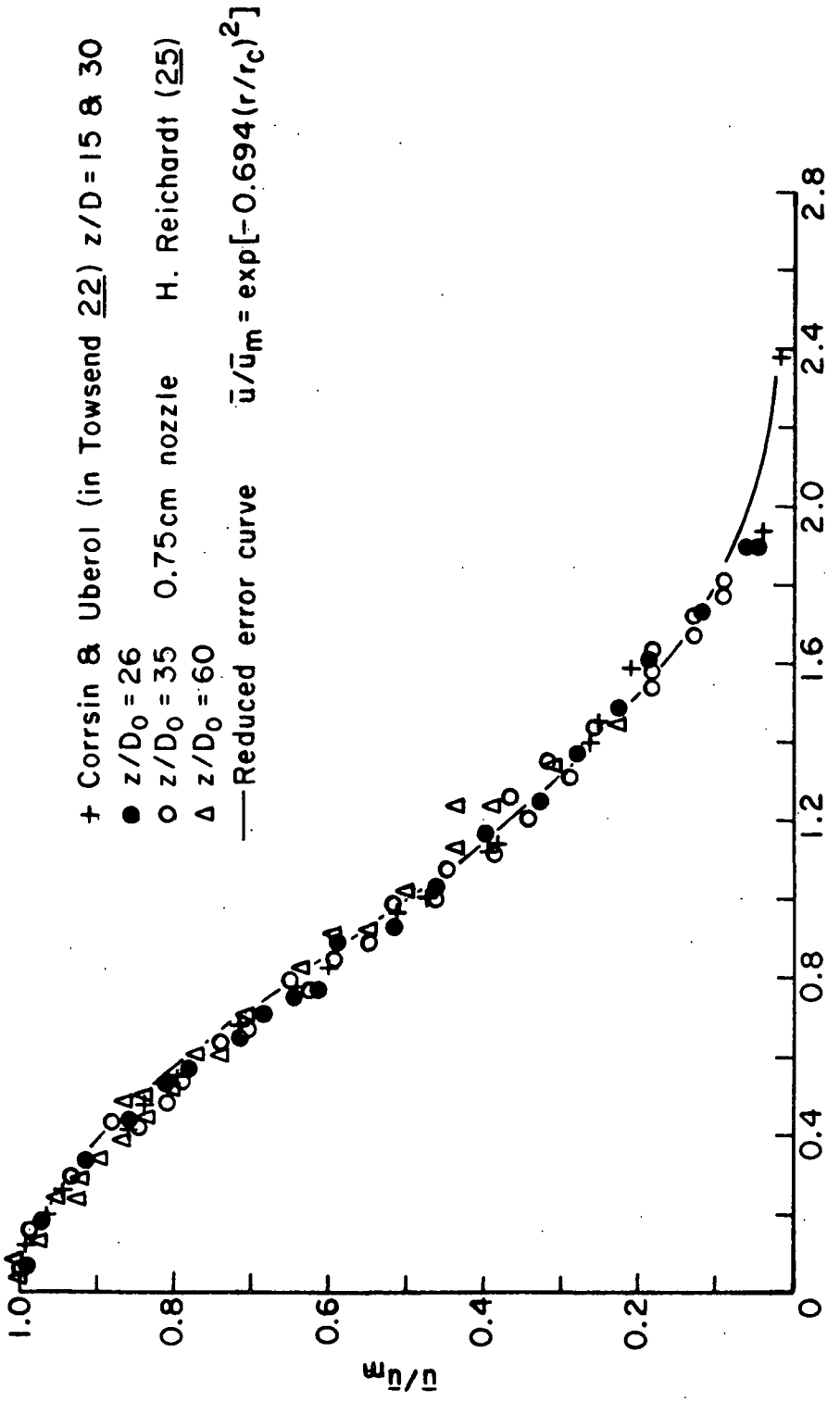

Figure 34. Experimental Air Jet Velocity Profiles

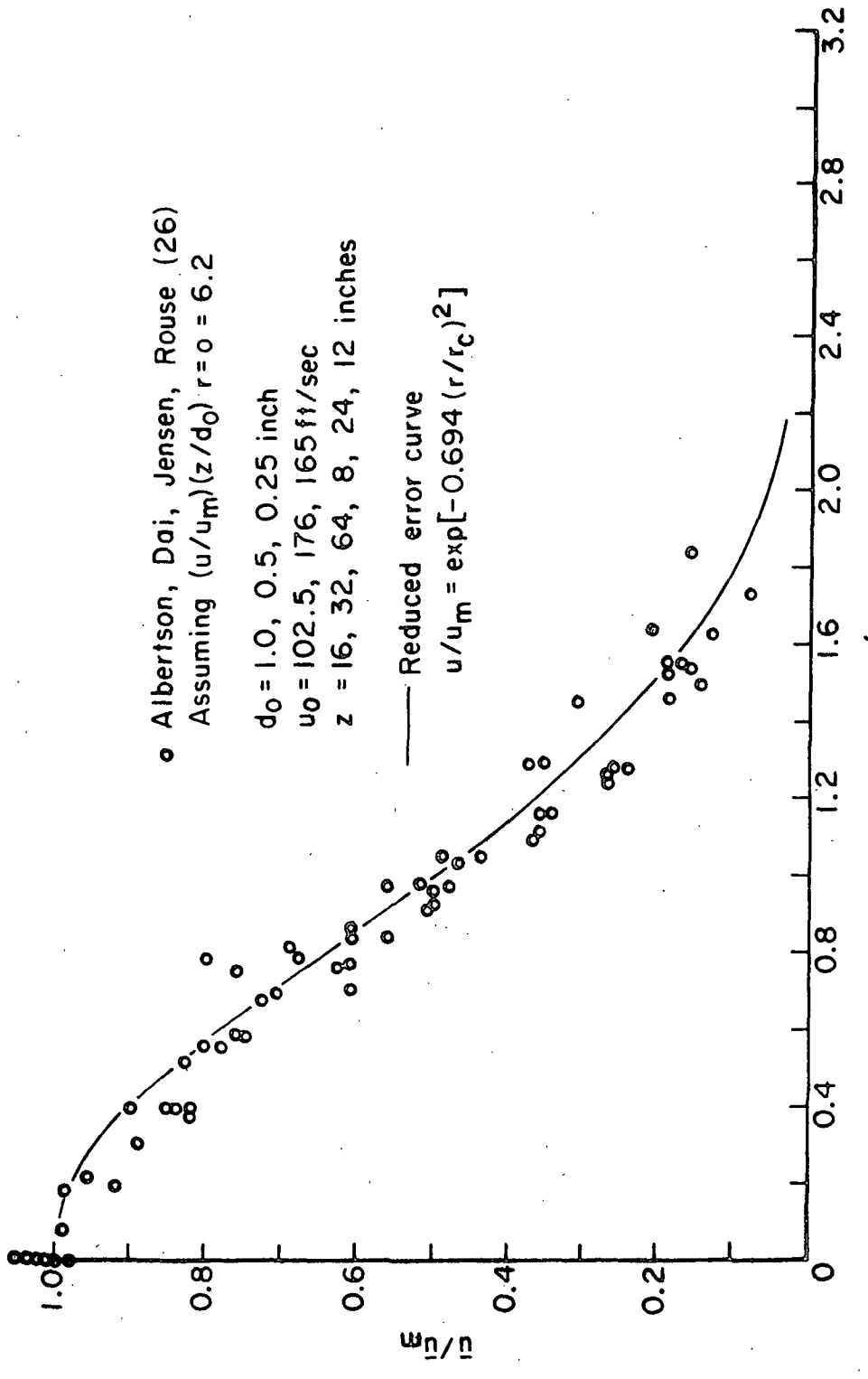

Figure 35. Experimental Air Jet Velocity Profiles

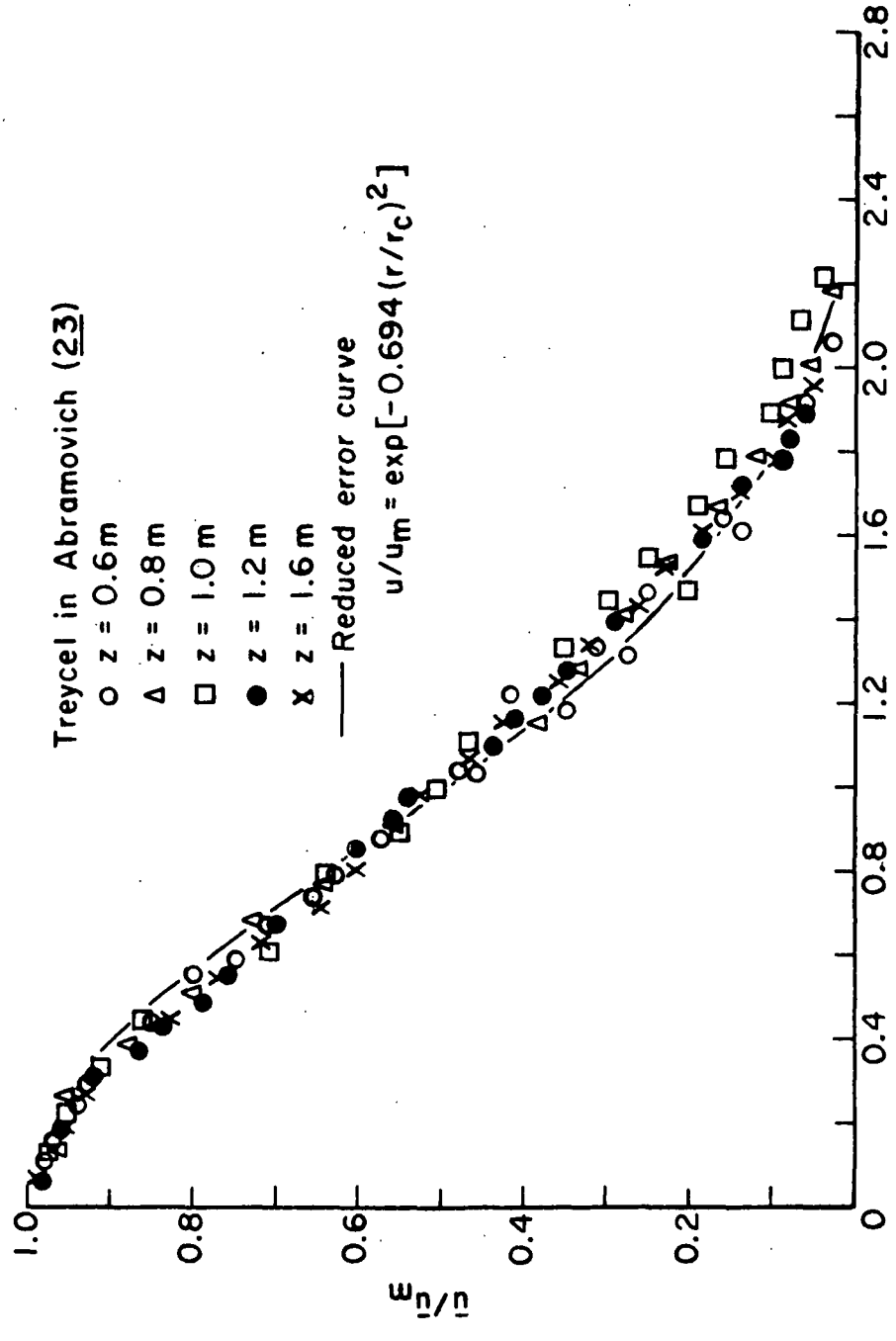

Figure 36. Experimental Air Jet Velocity Profiles

APPENDIX II

DETAILS OF PROBE SUPPORT, NOZZLE, AND SCREEN

Appendix II consists of Fig. 37-39 illustrating the cable and pulley system for probe positioning (exploded view), jet nozzle shape, and screen and nozzle baseplate.

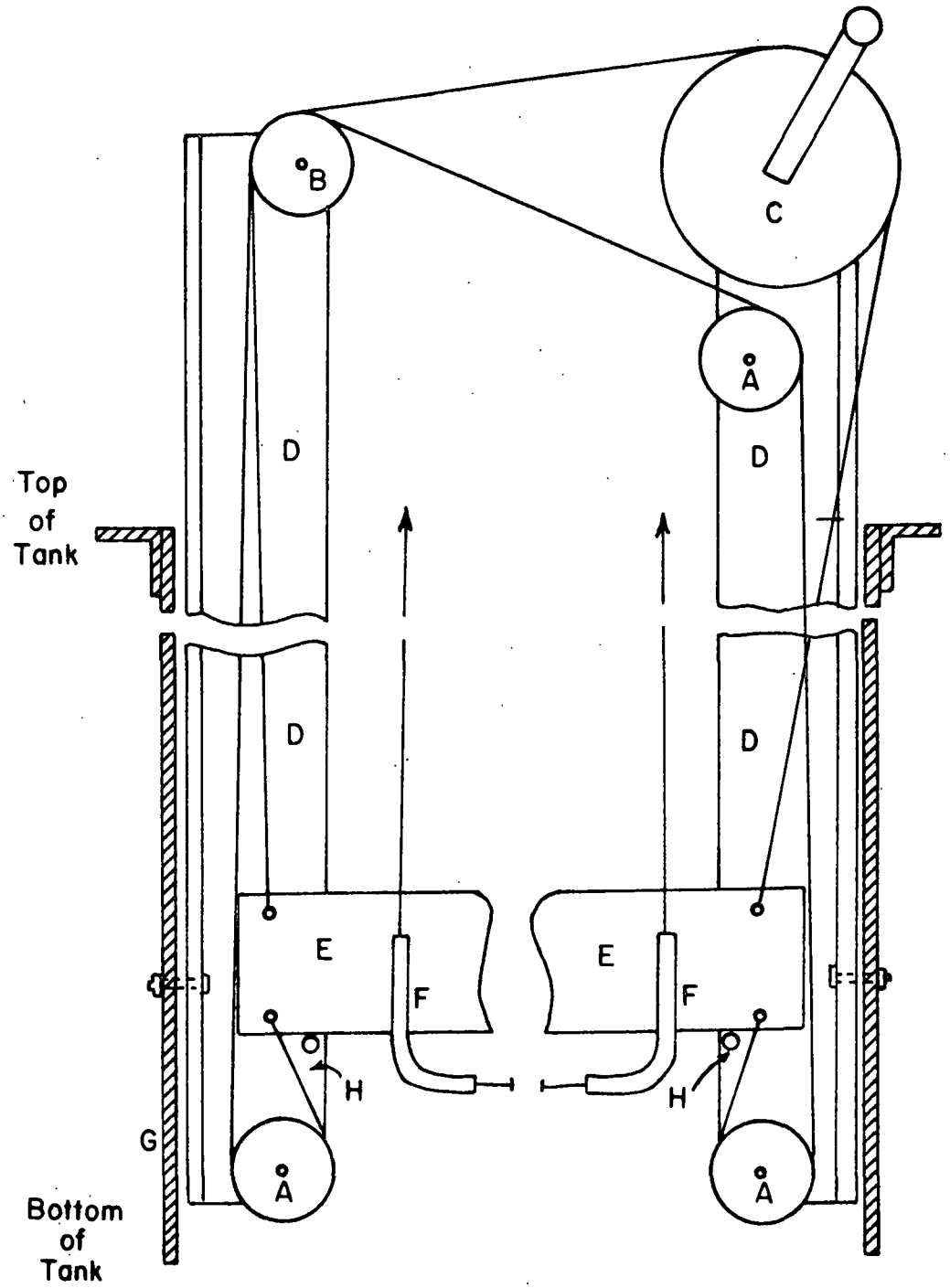

Figure 37. Cable and Pulley System for Probe Positioning (Exploded View)

A. Single brass pulley
B. Double brass pulley on single axle
C. Drive pulley with operating handle
D. Aluminum angles (3-m long)
E. Brass probe support beam (1.1-m long)
F. Guides radial movement cables
G. Jet tank wall
H. Stops for support beam

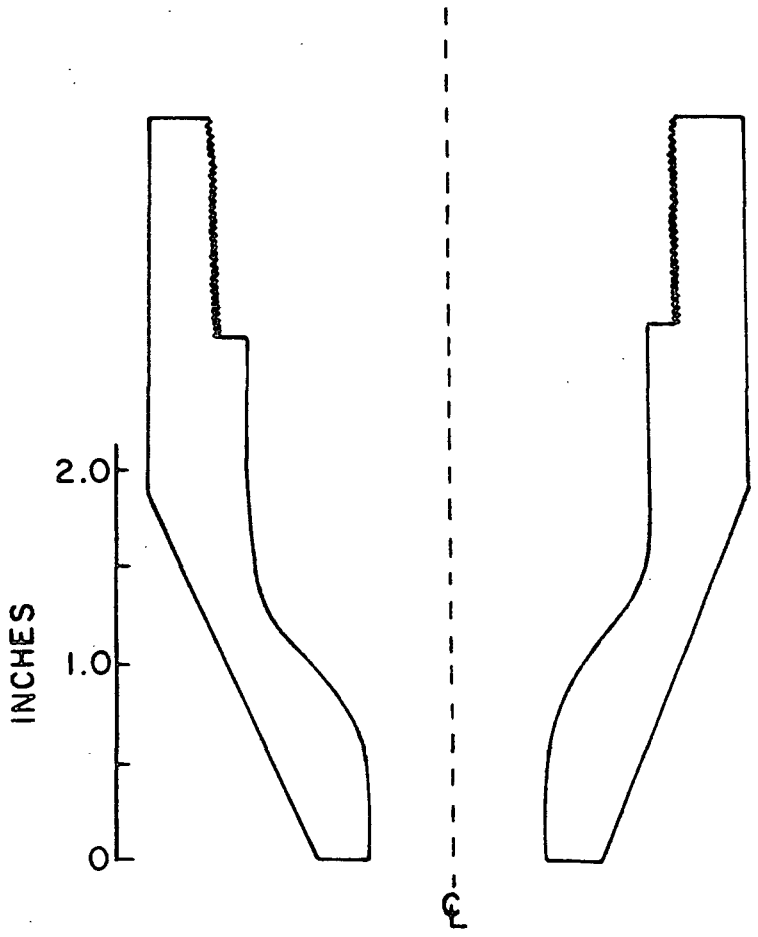

Height, in	Diameter, in
2.0	1.99
1.8	1.99
1.7	1.96
1.6	1.90
1.5	1.82
1.4	1.69
1.3	1.55
1.2	1.39
1.1	1.22
1.0	1.07
0.9	0.98
0.8	0.93
0.7	0.91
0.6	0.89
0.5	0.89
0.2	0.89
0	0.89

Figure 38. Jet Nozzle Shape

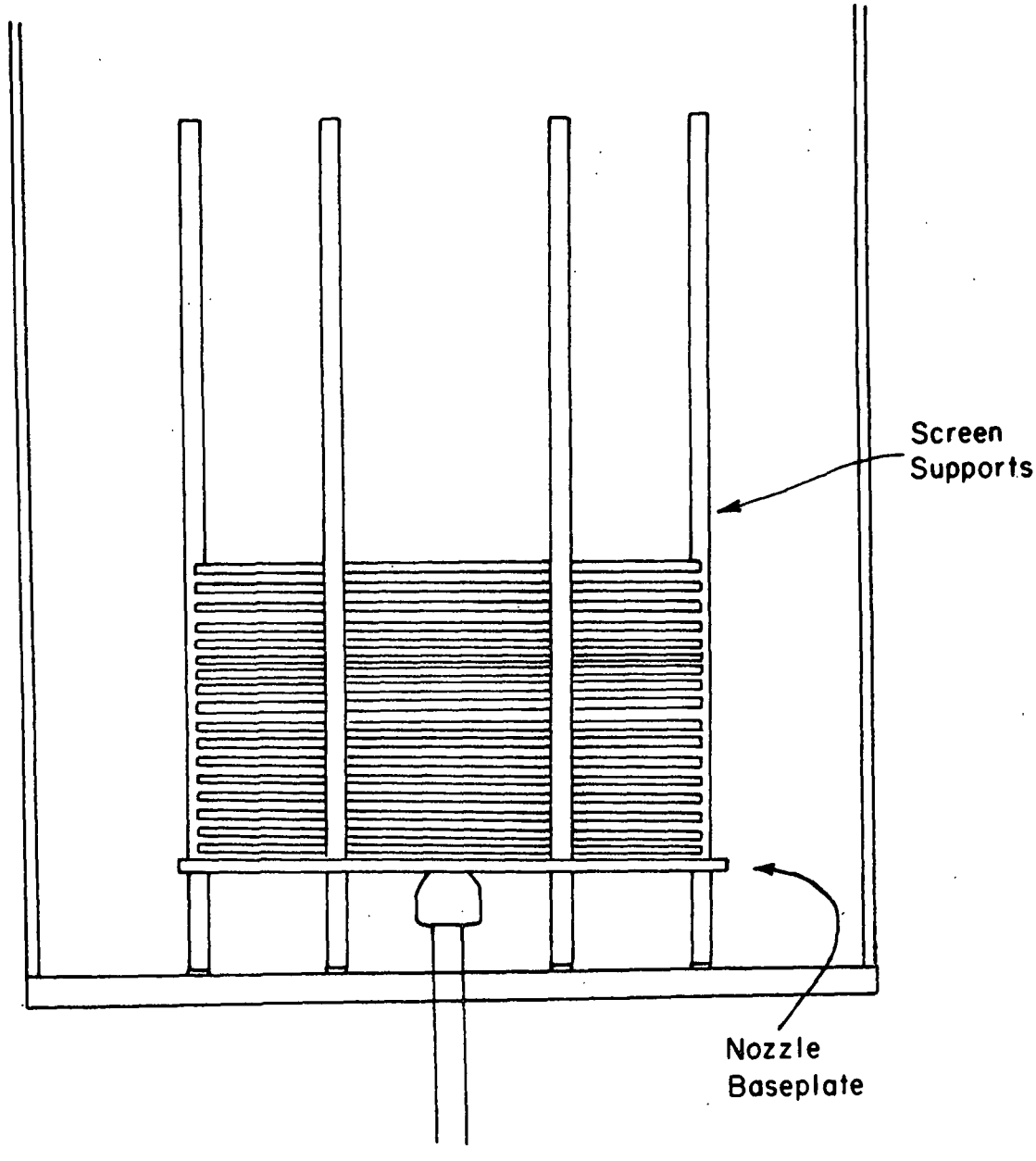

Figure 39. Screen and Nozzle Baseplate

APPENDIX III

IMPACT PRESSURE MEASUREMENT

The differential pressure transducers used were PACE Engineering Model KP15-1577 variable reluctance transducer. They contain a thin stainless steel diaphragm separating two chambers of water. Each chamber is connected through water-filled instrument tubing to one of the pressure sensing tubes in the jet tank. The slight deflection of the diaphragm due to the pressure difference creates an electronic signal. The signal is amplified and displayed on a PACE Indicator and can be recorded continuously.

From the chart recording a reliable mean pressure difference can be determined. The chart scale (0 to 100 units) is either 0 to 14 cm of water or 0 to 50 cm of water, depending on which transducer is connected to the recorder (the two were identical transducer bodies with different diaphragms). The velocity (cm/sec) is

$$\overline{U} = 16.6 \sqrt{\text{chart reading}}$$

for the 0 to 14 cm of water transducer, and

$$\overline{U} = 31.3 \sqrt{\text{chart reading}}$$

for the 0 to 50 cm of water transducer. The maximum velocity measured in the low range is 166 cm/sec and on the high range, 313 cm/sec.

PURGE EFFECT ON JET VELOCITY MEASUREMENTS

The following two figures show the effect of purge water velocity on the velocity measurements in the water jet, and the suspension jet, respectively (see Fig. 40 and 41).

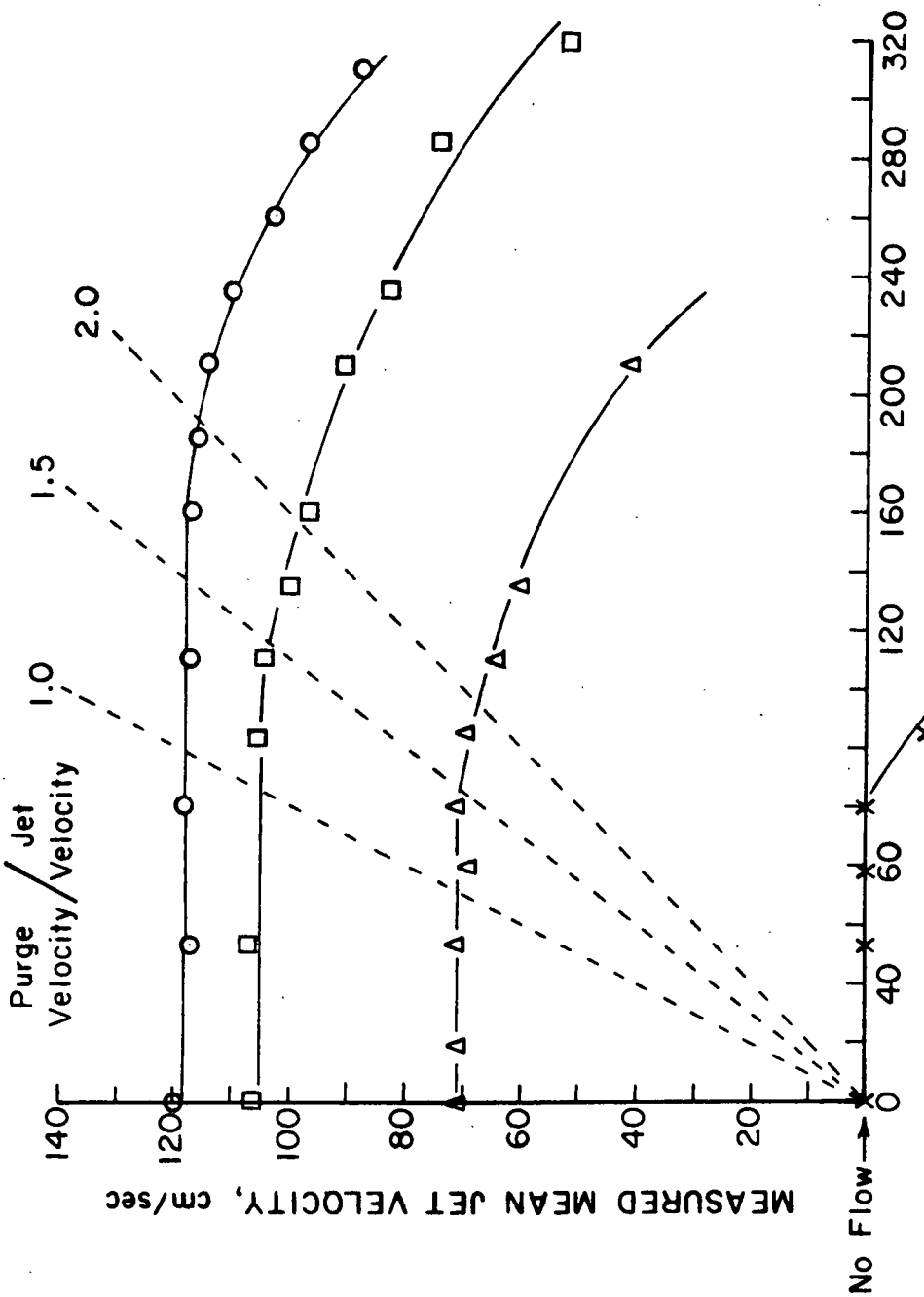

Figure 40. Purge Effect on Water Jet

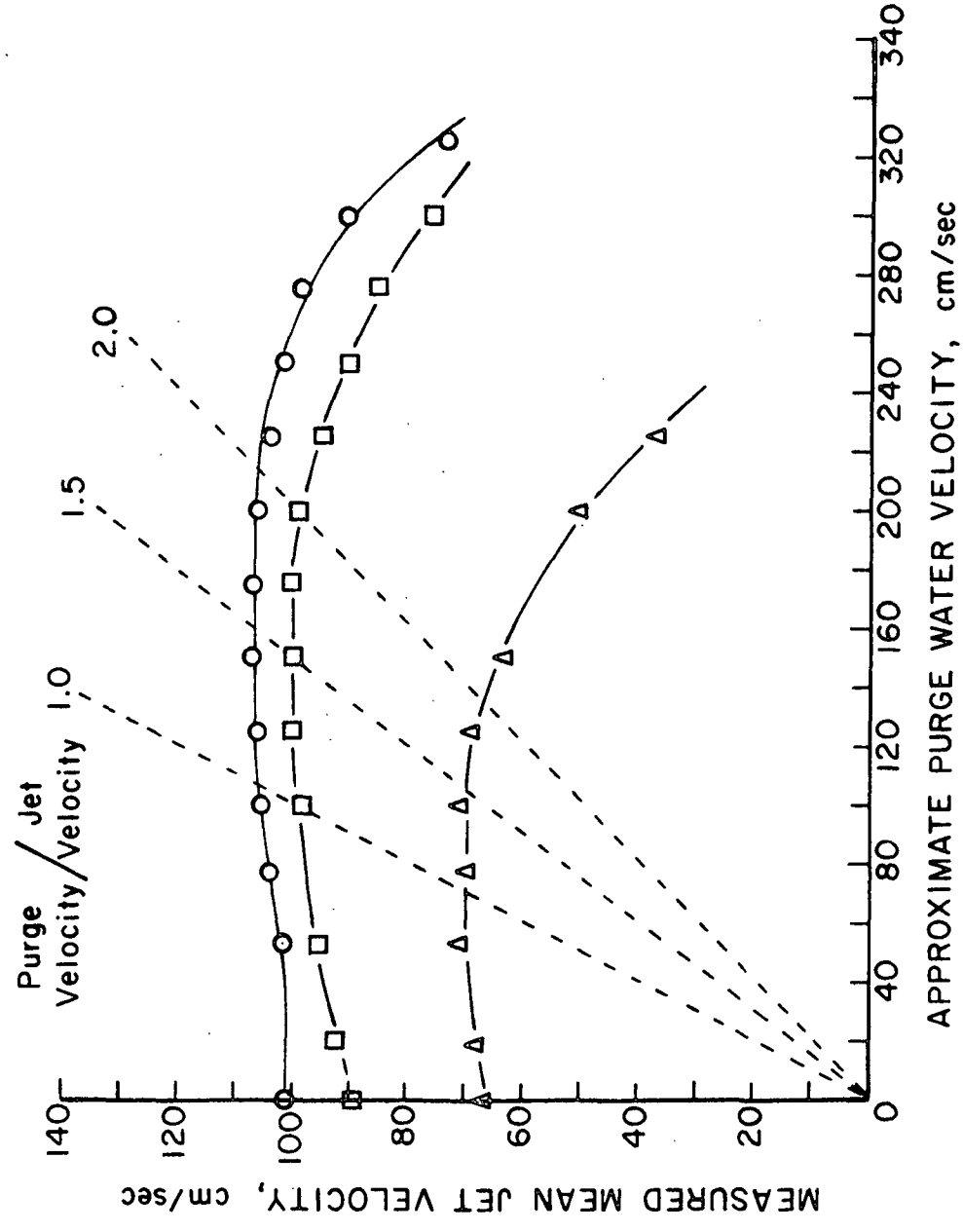

Figure 41. Purge Effect on Suspension Jet

APPENDIX IV

LIGHT SOURCE AND DETECTION SYSTEM DETAILS

LIGHT SOURCE

The light source was a quartz-iodine lamp powered by a regulated dc power supply. The lamp was housed in a small, blackened, cylindrical chamber. The end of one branch of the light guide was cemented in a length of brass tubing (20-cm long and 2.5 mm in diameter); its clad tip protruded 2 mm from one end of the tubing. A 7-cm length of 1.6-cm diameter brass rod was screw tightened perpendicular to the side of the lamp housing. The tubing containing the light guide fitted snugly through a hole along the axis of the brass rod. The light guide branch tip was thus held at a fixed angle to the lamp but the distance of the light guide tip from the lamp was variable for flexibility during the preliminary calibration experiments.

DETECTION SYSTEM

The photoconductive cell was purchased mounted in a plastic casing to which the light guide branch lead was fixed. The distance and angle between the light guide tip and the photocell surface had to be constant. They were kept immobile with the light guide tip in contact with the glass covering over the sensitive surface of the photocell.

The photoconductive cell was one element of the resistance bridge shown in Fig. 42. Normally, the bridge would be balanced for a particular value of the photocell resistance with a known variable resistance, R, at the galvanometer null. The variation from the galvanometer null reading due to variations in the photocell resistance was an indication of reflected light intensity fluctuations. The galvanometer signal was slightly unsteady and the accuracy

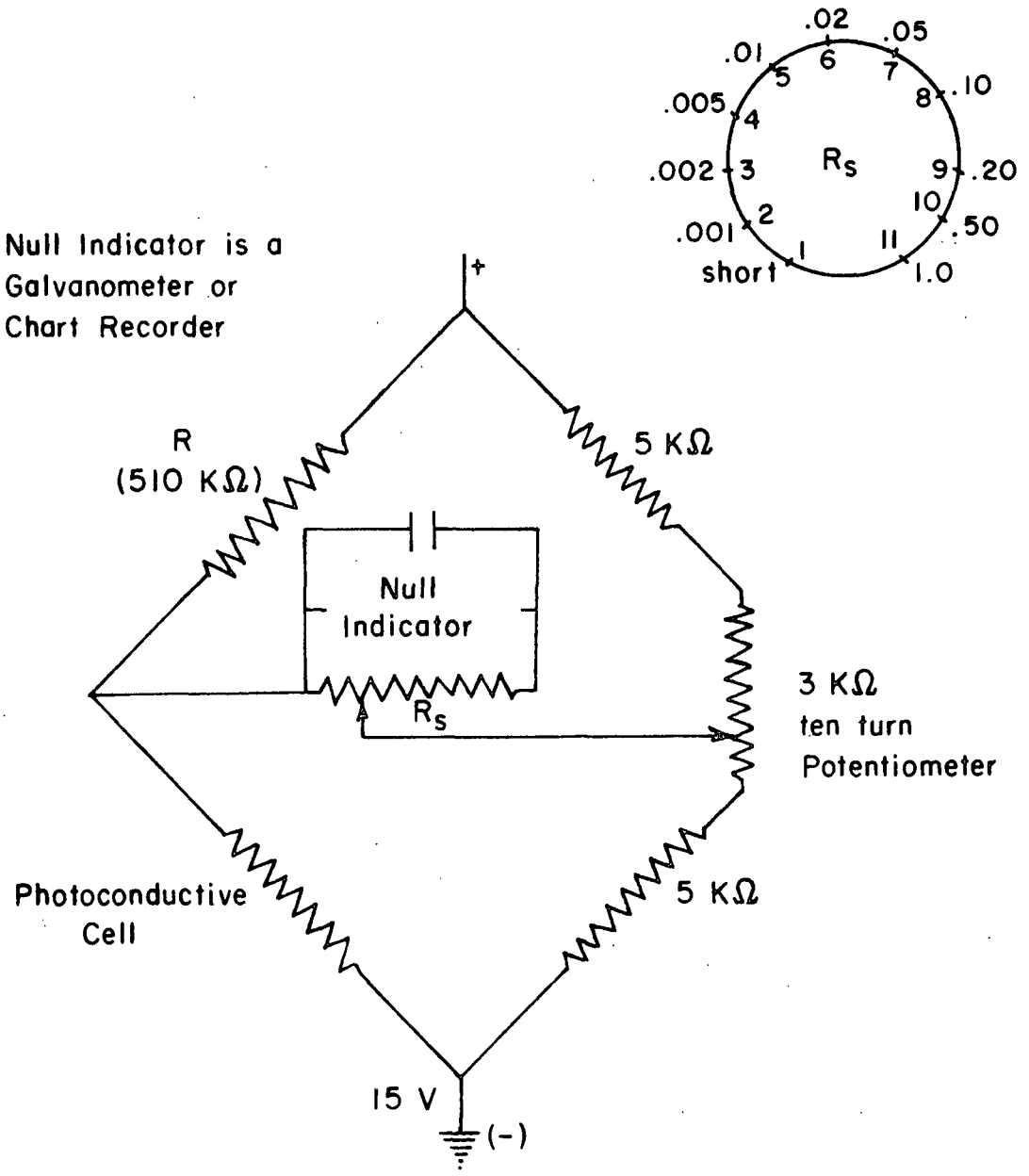

Figure 42. Resistance Bridge Circuit

of the measurements was greatly increased by substituting a continuous chart recorder (Esterline Angus) for the galvanometer. The recorder zero was turned to 50% of the recorder scale and the instrument acted as a recording null imbalance indicator.

One side of the resistance bridge contained the photocell and a known (but interchangeable) resistor, $\underline{R}$. In preliminary calibration work this resistance was changed repeatedly to find the best calibration curve for the range of nylon-12 consistencies of interest. For recalibration with a different suspension, $\underline{R}$ would be changed again. The resistance, $\underline{R}$, would be of the same order of magnitude as that of the photocell; that actually used in the consistency measurements is $\underline{R}$ = 510 KΩ.

The ten proportional resistance values of $\underline{R_s}$ allowed the voltage imbalance indicated by the recorder to be reduced to as little as 1/100 of the actual imbalance. The measurements were taken at setting number 4 (0.005) and a recorder half scale of 0.50 mv.

The photocell was a Clairex cadmium-sulfide cell (Cell No. CL705L). According to the Clairex published performance data (Fig. 43) the photocell is also slightly sensitive to temperature. A temperature rise of 1° at 25°C and a light intensity of about 0.01-ft candles should cause a 0.25% decrease in the resistance. In operation the photocell was insulated against large, sudden ambient temperature changes. A possible source of temperature changes was the heat built up by current flow through the high resistance photocell. A circuit analysis showed that only about 10^{-4} watts were generated since most of the current passes through the low resistance side of the bridge. The photocell casing was designed to dissipate 1250×10^{-4} watts. No problem of temperature sensitivity was experienced.

TYPE 5 of Cadmium Sulfide peaks at 5500 A. This material matches the response of the human eye. Its high sensitivity and good temperature characteristics also render it useful for precision light measuring devices. Several fields having applications for this particular sensitive material include light meters, cameras, automatic street light switches and color measuring equipment.

RESPONSE TIME VERSUS LIGHT LEVEL

Light Level (Foot Candles)	.01	0.1	1	10	100
Response time (to 1-1/e of final reading)					
Rise (seconds)	2.3	.30	.07	.02	.007
Decay (seconds)	1.3	.22	.06	.02	.014

CONDUCTANCE VERSUS LIGHT LEVEL

Light Level (Foot Candles)	.01	0.1	1	10	100
Temperature C					
-25°C	115%	97%	93%	90%	94%
0°C	103%	97%	95%	94%	96%
25°C	100%	100%	100%	100%	100%
50°C	107%	109%	114%	115%	106%
75°C	114%	126%	131%	138%	105%

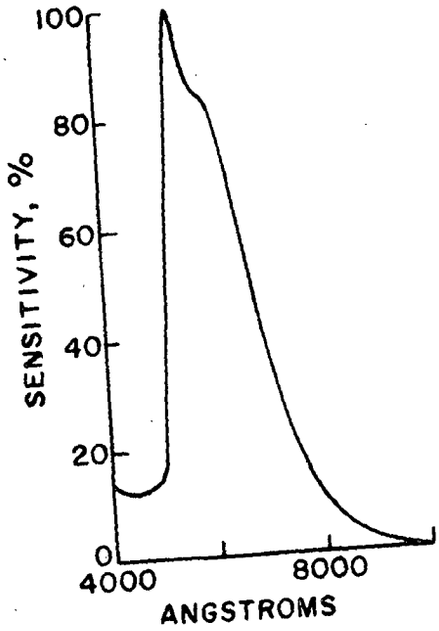

Cell #CL705L
(Type 5)

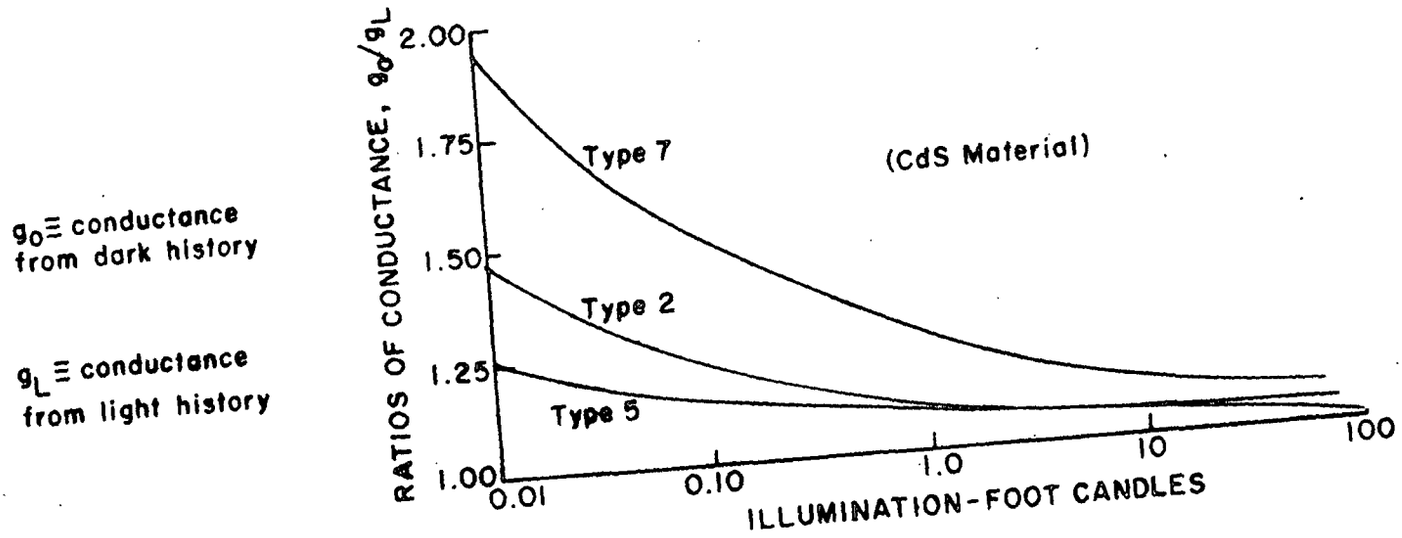

Figure 43. Clairex Published Performance Data

APPENDIX V

PROBE SUPPORT UNDER CALIBRATION NOZZLE

A support platform for the probe was connected below the nozzle on three long brass bolts equally spaced around the nozzle. The unused areas of the platform were cut away from the circular area to improve the mixing action in the lower half of the vessel. The platform could be raised or lowered easily by changing the positions of the nuts on the support bolts. A 2.5-cm long brass plug fitted in a 1.9-cm diameter hole cut in the center of the platform. The plug was held in place by three horizontal set screws equally spaced around the platform.

A length of approximately 3 cm at the back end of the stainless steel capping on the light guide was not covered by the purge jacket. This part of the light guide fitted through a 5-mm hole in the center of the brass plug so that the purge jacket rests on top of the plug. The light guide fits tightly in this support and is immobile in the oncoming flow. The tip of the probe is directly under the axis of the nozzle. If the set screws are loosened, the plug and probe can be moved together, either to a slightly different vertical position or out of the calibration vessel for inspection. A second plug had its 5-mm hole for the light guide 4.5 mm off the center of the plug. It made possible a check of the uniformity of the reflected light signal across the nozzle exit area in the plane of the flow loop.

APPENDIX VI

JET VELOCITY PROFILE DATA

The original velocity profile data are presented as they were tabulated by the computer program that determined the parameters r_c and u_m from the original data.

Each profile was recorded on a separate numbered recorder chart, at a given axial distance (Z), initial velocity (UO), and consistency. The parameters calculated by the least-squares program are the axial velocity (UM), the jet axis position (RZ), and the jet half-width, r_c (RC).

The original data are the relative position of the probe tip measured on the meter stick above the tank (RELPOS) and the velocity at that point (U).

The other numbers in each table are the actual position determined by comparing RELPOS with RZ (ACTPOS), the reduced radial position, r/r_c (R/RC), and the reduced velocity, u/u_m (U/UM).

The program also calculated the momentum ratio, M/M_o (M/MO) by the method described in the text with Equation (100).

JET VELOCITY PROFILE DATA CHARTS

CHART 5 Z= 25 CM UO= 383 CM/SEC CONSISTENCY=0.0 PERCENT

UM=202.3 RZ= 41.44 RC= 2.59

RELPOS (CM)	U (CM/SEC)	ACTPOS (CM)	R/RC	U/UM
36.80	22	-4.64	-1.79	0.109
37.20	32	-4.24	-1.63	0.158
37.50	41	-3.94	-1.52	0.203
38.00	60	-3.44	-1.32	0.297
38.35	76	-3.09	-1.19	0.376
38.85	102	-2.59	-1.00	0.504
39.30	125	-2.14	-0.82	0.618
39.80	152	-1.64	-0.63	0.751
40.25	176	-1.19	-0.46	0.870
40.80	195	-0.64	-0.25	0.964
41.00	198	-0.44	-0.17	0.979
41.60	202	0.16	0.06	0.999
41.85	198	0.41	0.16	0.979
42.30	188	0.86	0.33	0.929
42.80	167	1.36	0.53	0.826
43.20	147	1.76	0.68	0.727
43.50	129	2.06	0.80	0.638
43.95	106	2.51	0.97	0.524
44.40	82	2.96	1.14	0.405
44.80	63	3.36	1.30	0.311
45.20	47	3.76	1.45	0.232
45.55	35	4.11	1.59	0.173
46.10	21	4.66	1.80	0.104

M/MO= 1.047

CHART 11 Z= 35 CM UO= 383 CM/SEC CONSISTENCY=0.0 PERCENT

UM=149.4 RZ= 31.50 RC= 3.38

RELPOS (CM)	U (CM/SEC)	ACTPOS (CM)	R/RC	U/UM
25.95	23	-5.55	-1.64	0.154
26.35	33	-5.15	-1.52	0.221
26.80	42	-4.70	-1.39	0.281
27.20	47	-4.30	-1.27	0.315
27.75	64	-3.75	-1.11	0.428
28.55	86	-2.95	-0.87	0.576
28.95	101	-2.55	-0.75	0.676
29.50	117	-2.00	-0.59	0.783
29.85	126	-1.65	-0.49	0.844
30.50	141	-1.00	-0.29	0.944
31.10	148	-0.40	-0.12	0.991
31.65	150	0.15	0.05	1.004
32.35	144	0.85	0.25	0.964
33.00	131	1.50	0.45	0.877
33.55	114	2.05	0.61	0.763
34.15	98	2.65	0.79	0.656
34.70	80	3.20	0.95	0.536
35.15	64	3.65	1.08	0.428
35.60	53	4.10	1.21	0.355
36.35	36	4.85	1.44	0.241

M/MO= 0.969

CHART 12 Z= 45 CM UO= 383 CM/SEC CONSISTENCY=0.0 PERCENT

UM=115.6 RZ= 21.00 RC= 4.24

RELPOS (CM)	U (CM/SEC)	ACTPOS (CM)	R/RC	U/UM
15.60	39	-5.40	-1.27	0.337
16.20	48	-4.80	-1.13	0.415
16.95	61	-4.05	-0.96	0.528
17.75	77	-3.25	-0.77	0.666
18.45	88	-2.55	-0.60	0.761
19.10	98	-1.90	-0.45	0.847
19.95	111	-1.05	-0.25	0.960
20.90	116	-0.10	-0.02	1.003
21.50	116	0.50	0.12	1.003
22.15	110	1.15	0.27	0.951
22.85	102	1.85	0.44	0.882
23.45	92	2.45	0.58	0.796
24.20	78	3.20	0.75	0.675
24.85	66	3.85	0.91	0.571
25.45	54	4.45	1.05	0.467
26.00	44	5.00	1.18	0.380
26.75	33	5.75	1.36	0.285
27.30	23	6.30	1.49	0.199

M/MO= 0.914

CHART 55 Z= 55 CM UO= 383 CM/SEC CONSISTENCY=0.0 PERCENT

UM= 95.9 RZ= 26.44 RC= 5.10

RELPOS (CM)	U (CM/SEC)	ACTPOS (CM)	R/RC	U/UM
20.20	33	-6.24	-1.22	0.344
20.95	44	-5.49	-1.08	0.459
21.55	50	-4.89	-0.96	0.522
22.15	59	-4.29	-0.84	0.615
22.95	68	-3.49	-0.68	0.709
23.70	78	-2.74	-0.54	0.814
24.35	85	-2.09	-0.41	0.887
25.00	90	-1.44	-0.28	0.939
25.65	94	-0.79	-0.16	0.980
26.15	96	-0.29	-0.06	1.001
26.85	96	0.41	0.08	1.001
27.55	93	1.11	0.22	0.970
28.30	87	1.86	0.36	0.907
29.00	81	2.56	0.50	0.845
29.65	72	3.21	0.63	0.751
30.30	69	3.86	0.76	0.720
30.85	56	4.41	0.86	0.584
31.70	45	5.26	1.03	0.469
32.25	39	5.81	1.14	0.407
33.00	30	6.56	1.29	0.313
33.65	25	7.21	1.41	0.261

M/MO= 0.910

CHART 6 Z= 25 CM UO= 475 CM/SEC CONSISTENCY=0.0 PERCENT

UM=243.6 RZ= 41.35 RC= 2.62

RELPOS (CM)	U (CM/SEC)	ACTPOS (CM)	R/RC	U/UM
45.75	33	4.40	1.68	0.135
45.40	47	4.05	1.54	0.193
44.80	75	3.45	1.31	0.308
44.05	119	2.70	1.03	0.488
43.65	143	2.30	0.88	0.587
43.35	161	2.00	0.76	0.661
42.95	188	1.60	0.61	0.772
42.45	216	1.10	0.42	0.887
41.90	235	0.55	0.21	0.965
41.60	242	0.25	0.10	0.993
41.15	243	-0.20	-0.08	0.997
40.85	238	-0.50	-0.19	0.977
40.50	226	-0.85	-0.32	0.928
40.25	214	-1.10	-0.42	0.878
39.90	199	-1.45	-0.55	0.817
39.50	173	-1.85	-0.70	0.710
38.80	128	-2.55	-0.97	0.525
38.20	92	-3.15	-1.20	0.378
37.70	64	-3.65	-1.39	0.263
37.25	45	-4.10	-1.56	0.185
36.90	29	-4.45	-1.70	0.119
36.70	23	-4.65	-1.77	0.094

M/MO= 1.011

CHART 10 Z= 35 CM UO= 475 CM/SEC CONSISTENCY=0.0 PERCENT

UM=180.2 RZ= 31.30 RC= 3.41

RELPOS (CM)	U (CM/SEC)	ACTPOS (CM)	R/RC	U/UM
36.40	35	5.10	1.49	0.194
35.65	56	4.35	1.27	0.311
34.90	85	3.60	1.06	0.472
34.40	102	3.10	0.91	0.566
33.70	128	2.40	0.70	0.710
33.05	150	1.75	0.51	0.833
32.65	160	1.35	0.40	0.888
31.75	177	0.45	0.13	0.982
31.10	180	-0.20	-0.06	0.999
30.50	173	-0.80	-0.23	0.960
30.00	164	-1.30	-0.38	0.910
29.35	144	-1.95	-0.57	0.799
28.65	120	-2.65	-0.78	0.666
27.95	93	-3.35	-0.98	0.516
27.40	74	-3.90	-1.14	0.411
26.45	44	-4.85	-1.42	0.244
25.60	26	-5.70	-1.67	0.144

M/MO= 0.935

CHART 13 Z= 45 CM UO= 475 CM/SEC CONSISTENCY=0.0 PERCENT

UM=139.7 RZ= 21.10 RC= 4.30

RELPOS (CM)	U (CM/SEC)	ACTPOS (CM)	R/RC	U/UM
27.55	29	6.45	1.50	0.208
26.55	45	5.45	1.27	0.322
25.55	67	4.45	1.04	0.480
24.90	81	3.80	0.88	0.580
23.95	103	2.85	0.66	0.737
22.95	123	1.85	0.43	0.880
21.85	137	0.75	0.17	0.981
21.35	140	0.25	0.06	1.002
20.50	138	-0.60	-0.14	0.988
19.75	130	-1.35	-0.31	0.931
18.75	113	-2.35	-0.55	0.809
18.00	96	-3.10	-0.72	0.687
17.30	82	-3.80	-0.88	0.587
16.45	62	-4.65	-1.08	0.444
15.85	50	-5.25	-1.22	0.358
15.10	37	-6.00	-1.40	0.265

M/MO= 0.892

CHART 53 Z= 55 CM UO= 475 CM/SEC CONSISTENCY=0.0 PERCENT

UM=115.9 RZ= 26.40 RC= 5.03

RELPOS (CM)	U (CM/SEC)	ACTPOS (CM)	R/RC	U/UM
18.90	24	-7.50	-1.49	0.207
19.55	33	-6.85	-1.36	0.285
20.30	41	-6.10	-1.21	0.354
20.85	51	-5.55	-1.10	0.440
21.45	60	-4.95	-0.98	0.518
22.05	70	-4.35	-0.86	0.604
22.65	79	-3.75	-0.74	0.682
23.25	88	-3.15	-0.63	0.759
23.85	97	-2.55	-0.51	0.837
24.45	104	-1.95	-0.39	0.897
25.00	110	-1.40	-0.28	0.949
25.60	114	-0.80	-0.16	0.983
26.30	117	-0.10	-0.02	1.009
26.90	115	0.50	0.10	0.992
27.70	111	1.30	0.26	0.958
28.35	104	1.95	0.39	0.897
29.15	93	2.75	0.55	0.802
29.80	84	3.40	0.68	0.725
30.55	72	4.15	0.83	0.621
31.30	60	4.90	0.97	0.518
31.90	50	5.50	1.09	0.431
32.60	40	6.20	1.23	0.345

M/MO= 0.841

CHART 16 Z= 25 CM UO= 538 CM/SEC CONSISTENCY=0.0 PERCENT

UM=302.2 RZ= 41.25 RC= 2.39

RELPOS (CM)	U (CM/SEC)	ACTPOS (CM)	R/RC	U/UM
36.90	30	-4.35	-1.82	0.099
37.35	47	-3.90	-1.63	0.156
37.55	57	-3.70	-1.55	0.189
37.85	75	-3.40	-1.42	0.248
38.40	114	-2.85	-1.19	0.377
38.90	154	-2.35	-0.98	0.510
39.40	198	-1.85	-0.77	0.655
39.85	236	-1.40	-0.59	0.781
40.15	259	-1.10	-0.46	0.857
40.50	282	-0.75	-0.31	0.933
40.90	299	-0.35	-0.15	0.989
41.05	303	-0.20	-0.08	1.003
41.45	302	0.20	0.08	0.999
41.75	294	0.50	0.21	0.973
42.15	274	0.90	0.38	0.907
42.55	243	1.30	0.54	0.804
42.85	221	1.60	0.67	0.731
43.25	186	2.00	0.84	0.616
43.60	158	2.35	0.98	0.523
44.05	122	2.80	1.17	0.404
44.20	98	2.95	1.23	0.324
44.60	79	3.35	1.40	0.261
45.10	52	3.85	1.61	0.172
45.80	26	4.55	1.90	0.086

M/MO= 1.007

CHART 9 Z= 35 CM UO= 538 CM/SEC CONSISTENCY=0.0 PERCENT

UM=219.7 RZ= 31.45 RC= 3.16

RELPOS (CM)	U (CM/SEC)	ACTPOS (CM)	R/RC	U/UM
25.65	17	-5.80	-1.83	0.077
26.00	29	-5.45	-1.72	0.132
26.50	42	-4.95	-1.56	0.191
26.95	55	-4.50	-1.42	0.250
27.55	73	-3.90	-1.23	0.332
28.15	104	-3.30	-1.04	0.473
28.75	134	-2.70	-0.85	0.610
29.10	150	-2.35	-0.74	0.683
29.60	173	-1.85	-0.58	0.787
30.20	197	-1.25	-0.40	0.897
30.70	212	-0.75	-0.24	0.965
31.05	217	-0.40	-0.13	0.988
31.60	219	0.15	0.05	0.997
32.15	212	0.70	0.22	0.965
32.65	198	1.20	0.38	0.901
33.00	185	1.55	0.49	0.842
33.60	161	2.15	0.68	0.733
34.25	131	2.80	0.88	0.596
34.65	106	3.20	1.01	0.482

M/MO=0.932

CHART 14 Z= 45 CM UO= 538 CM/SEC CONSISTENCY=0.0 PERCENT

UM=172.4 RZ= 21.00 RC= 3.96

RELPOS (CM)	U (CM/SEC)	ACTPOS (CM)	R/RC	U/UM
14.40	23	-6.60	-1.67	0.133
15.20	39	-5.80	-1.47	0.226
15.90	55	-5.10	-1.29	0.319
16.50	72	-4.50	-1.14	0.418
17.05	87	-3.95	-1.00	0.505
17.60	100	-3.40	-0.86	0.580
18.00	117	-3.00	-0.76	0.679
18.60	133	-2.40	-0.61	0.772
19.10	147	-1.90	-0.48	0.853
19.70	160	-1.30	-0.33	0.928
20.25	168	-0.75	-0.19	0.975
20.75	171	-0.25	-0.06	0.992
21.30	171	0.30	0.08	0.992
21.90	166	0.90	0.23	0.963
22.30	160	1.30	0.33	0.928
22.90	148	1.90	0.48	0.859
23.55	131	2.55	0.64	0.760
24.00	116	3.00	0.76	0.673
24.75	94	3.75	0.95	0.545
25.30	75	4.30	1.09	0.435
25.85	60	4.85	1.23	0.348
26.40	47	5.40	1.36	0.273
27.20	31	6.20	1.57	0.180

M/MO= 0.897

CHART 54 Z= 55 CM UO= 538 CM/SEC CONSISTENCY=0.0 PERCENT

UM=139.9 RZ= 26.40 RC= 4.75

RELPOS (CM)	U (CM/SEC)	ACTPOS (CM)	R/RC	U/UM
33.55	27	7.15	1.50	0.193
32.75	41	6.35	1.34	0.293
32.05	52	5.65	1.19	0.372
31.25	68	4.85	1.02	0.486
30.65	80	4.25	0.89	0.572
29.95	94	3.55	0.75	0.672
29.25	108	2.85	0.60	0.772
28.50	122	2.10	0.44	0.872
27.85	132	1.45	0.31	0.944
27.30	136	0.90	0.19	0.972
26.50	139	0.10	0.02	0.994
25.70	138	-0.70	-0.15	0.987
25.05	132	-1.35	-0.28	0.944
24.10	119	-2.30	-0.48	0.851
23.15	103	-3.25	-0.68	0.736
22.35	86	-4.05	-0.85	0.615
21.55	69	-4.85	-1.02	0.493
20.75	52	-5.65	-1.19	0.372
20.05	41	-6.35	-1.34	0.293

M/MO= 0.852
STOP 00000

CHART 52 Z= 25 CM UO= 475 CM/SEC CONSISTENCY=0.12 PERCENT

UM=243.1 RZ= 56.50 RC= 2.62

RELPOS (CM)	U (CM/SEC)	ACTPOS (CM)	R/RC	U/UM
60.50	44	4.00	1.53	0.181
59.85	73	3.35	1.28	0.300
59.30	105	2.80	1.07	0.432
58.75	140	2.25	0.86	0.576
58.10	181	1.60	0.61	0.744
57.60	212	1.10	0.42	0.872
57.15	233	0.65	0.25	0.958
56.85	243	0.35	0.13	0.999
56.40	246	-0.10	-0.04	1.012
55.95	237	-0.55	-0.21	0.975
55.50	220	-1.00	-0.38	0.905
55.10	201	-1.40	-0.53	0.827
54.50	164	-2.00	-0.76	0.675
54.00	131	-2.50	-0.95	0.539
53.30	92	-3.20	-1.22	0.378
52.80	70	-3.70	-1.41	0.288
52.10	39	-4.40	-1.68	0.160

M/MO= 1.003

CHART 51 Z= 35 CM UO= 475 CM/SEC CONSISTENCY=0.12 PERCENT

UM=180.3 RZ= 46.50 RC= 3.46

RELPOS (CM)	U (CM/SEC)	ACTPOS (CM)	R/RC	U/UM
40.95	30	-5.55	-1.60	0.166
41.55	44	-4.95	-1.43	0.244
42.10	61	-4.40	-1.27	0.338
42.65	78	-3.85	-1.11	0.433
43.40	105	-3.10	-0.89	0.582
43.95	126	-2.55	-0.74	0.699
44.40	139	-2.10	-0.61	0.771
45.00	159	-1.50	-0.43	0.882
45.40	169	-1.10	-0.32	0.937
46.05	181	-0.45	-0.13	1.004
46.65	182	0.15	0.04	1.009
47.30	174	0.80	0.23	0.965
47.90	157	1.40	0.40	0.871
48.40	144	1.90	0.55	0.799
49.10	119	2.60	0.75	0.660
49.75	94	3.25	0.94	0.521
50.40	73	3.90	1.13	0.405
50.90	61	4.40	1.27	0.338
51.50	43	5.00	1.44	0.238

M/MO= 0.964

CHART 50 Z= 45 CM UO= 475 CM/SEC CONSISTENCY=0.12 PERCENT

UM=140.9 RZ= 36.60 RC= 4.30

RELPOS (CM)	U (CM/SEC)	ACTPOS (CM)	R/RC	U/UM
42.70	33	6.10	1.42	0.234
42.20	43	5.60	1.30	0.305
41.55	56	4.95	1.15	0.398
40.85	71	4.25	0.99	0.504
40.25	85	3.65	0.85	0.603
39.70	98	3.10	0.72	0.696
39.00	113	2.40	0.56	0.802
38.40	123	1.80	0.42	0.873
37.65	133	1.05	0.24	0.944
37.15	139	0.55	0.13	0.987
36.85	141	0.25	0.06	1.001
36.30	141	-0.30	-0.07	1.001
35.70	138	-0.90	-0.21	0.980
35.10	130	-1.50	-0.35	0.923
34.55	121	-2.05	-0.48	0.859
33.85	107	-2.75	-0.64	0.760
33.00	87	-3.60	-0.84	0.618
32.35	73	-4.25	-0.99	0.518
31.55	54	-5.05	-1.17	0.383
30.85	41	-5.75	-1.34	0.291
30.35	33	-6.25	-1.45	0.234

M/MO= 0.906

CHART 49 Z= 55 CM UO= 475 CM/SEC CONSISTENCY=0.12 PERCENT

UM=114.8 RZ= 26.60 RC= 5.06

RELPOS (CM)	U (CM/SEC)	ACTPOS (CM)	R/RC	U/UM
19.65	33	-6.95	-1.37	0.287
20.20	39	-6.40	-1.26	0.340
20.90	46	-5.70	-1.13	0.401
21.55	58	-5.05	-1.00	0.505
22.15	67	-4.45	-0.88	0.584
22.95	79	-3.65	-0.72	0.688
23.65	90	-2.95	-0.58	0.784
25.10	106	-1.50	-0.30	0.923
24.40	101	-2.20	-0.43	0.880
25.60	112	-1.00	-0.20	0.976
26.20	115	-0.40	-0.08	1.002
26.75	115	0.15	0.03	1.002
27.45	113	0.85	0.17	0.984
28.15	107	1.55	0.31	0.932
28.85	101	2.25	0.44	0.880
29.40	93	2.80	0.55	0.810
30.05	84	3.45	0.68	0.732
30.60	75	4.00	0.79	0.653
31.35	63	4.75	0.94	0.549
32.25	47	5.65	1.12	0.409
32.75	41	6.15	1.21	0.357
33.15	35	6.55	1.29	0.305

M/MO= 0.835
STOP 00000

CHART 45 Z= 25 CM UO= 475 CM/SEC CONSISTENCY-0.21 PERCENT

UM=238.8 RZ= 56.50 RC= 2.63

RELPOS (CM)	U (CM/SEC)	ACTPOS (CM)	R/RC	U/UM
51.50	24	-5.00	-1.90	0.100
52.00	39	-4.50	-1.71	0.163
52.45	52	-4.05	-1.54	0.218
53.05	76	-3.45	-1.31	0.318
53.55	104	-2.95	-1.12	0.435
54.00	129	-2.50	-0.95	0.540
54.45	157	-2.05	-0.78	0.657
54.85	182	-1.65	-0.63	0.762
55.25	205	-1.25	-0.47	0.858
55.75	228	-0.75	-0.28	0.955
56.25	243	-0.25	-0.09	1.018
56.70	239	0.20	0.08	1.001
57.50	212	1.00	0.38	0.888
58.05	185	1.55	0.59	0.775
58.45	156	1.95	0.74	0.653
59.05	121	2.55	0.97	0.507
59.50	94	3.00	1.14	0.394
60.05	62	3.55	1.35	0.260
60.60	37	4.10	1.56	0.155

M/MO= 0.975

CHART 46 Z= 35 CM UO= 475 CM/SEC CONSISTENCY-0.21 PERCENT

UM=179.4 RZ= 46.60 RC= 3.42

RELPOS (CM)	U (CM/SEC)	ACTPOS (CM)	R/RC	U/UM
51.90	30	5.30	1.55	0.167
51.10	50	4.50	1.32	0.279
50.45	72	3.85	1.13	0.401
49.65	104	3.05	0.89	0.580
49.05	126	2.45	0.72	0.702
48.50	145	1.90	0.56	0.808
48.10	157	1.50	0.44	0.875
47.65	168	1.05	0.31	0.937
47.30	174	0.70	0.20	0.970
46.95	180	0.35	0.10	1.003
46.50	180	-0.10	-0.03	1.003
46.10	178	-0.50	-0.15	0.992
45.70	169	-0.90	-0.26	0.942
45.15	156	-1.45	-0.42	0.870
44.45	136	-2.15	-0.63	0.758
43.90	115	-2.70	-0.79	0.641
43.25	93	-3.35	-0.98	0.518
42.75	77	-3.85	-1.13	0.429
42.05	57	-4.55	-1.33	0.318
41.45	41	-5.15	-1.51	0.229
41.00	27	-5.60	-1.64	0.151

M/MO= 0.929

CHART 47 Z= 45 CM UO= 475 CM/SEC CONSISTENCY=0.21 PERCENT

UM=143.5 RZ= 36.60 RC= 4.14

RELPOS (CM)	U (CM/SEC)	ACTPOS (CM)	R/RC	U/UM
29.75	21	-6.85	-1.65	0.146
30.25	27	-6.35	-1.53	0.188
31.00	41	-5.60	-1.35	0.286
31.65	52	-4.95	-1.19	0.362
32.40	72	-4.20	-1.01	0.502
33.05	87	-3.55	-0.86	0.606
33.70	104	-2.90	-0.70	0.725
34.30	117	-2.30	-0.55	0.815
35.05	129	-1.55	-0.37	0.899
35.55	138	-1.05	-0.25	0.961
35.95	142	-0.65	-0.16	0.989
36.40	143	-0.20	-0.05	0.996
36.90	143	0.30	0.07	0.996
37.45	139	0.85	0.21	0.968
37.90	132	1.30	0.31	0.920
38.35	126	1.75	0.42	0.878
38.90	117	2.30	0.56	0.815
39.60	100	3.00	0.72	0.697
40.25	83	3.65	0.88	0.578
40.80	70	4.20	1.01	0.488
41.30	58	4.70	1.13	0.404
41.80	49	5.20	1.25	0.341
42.35	37	5.75	1.39	0.258

M/MO= 0.875

CHART 48 Z= 55 CM UO= 475 CM/SEC CONSISTENCY=0.21 PERCENT

UM=116.7 RZ= 26.60 RC= 4.77

RELPOS (CM)	U (CM/SEC)	ACTPOS (CM)	R/RC	U/UM
33.00	35	6.40	1.34	0.300
32.10	46	5.50	1.15	0.394
31.55	57	4.95	1.04	0.488
30.75	70	4.15	0.87	0.600
30.25	80	3.65	0.76	0.685
29.75	86	3.15	0.66	0.737
29.10	98	2.50	0.52	0.840
28.60	104	2.00	0.42	0.891
28.00	111	1.40	0.29	0.951
27.35	115	0.75	0.16	0.985
26.60	117	-0.00	-0.00	1.003
26.00	115	-0.60	-0.13	0.985
25.30	110	-1.30	-0.27	0.943
24.60	103	-2.00	-0.42	0.883
23.95	92	-2.65	-0.56	0.788
23.50	86	-3.10	-0.65	0.737
22.95	76	-3.65	-0.77	0.651
22.35	66	-4.25	-0.89	0.566
21.70	56	-4.90	-1.03	0.480
21.00	44	-5.60	-1.17	0.377
20.25	33	-6.35	-1.33	0.283

M/MO= 0.765

CHART 44 Z= 25 CM UO= 475 CM/SEC CONSISTENCY=0.31 PERCENT

UM=236.7 RZ= 56.47 RC= 2.61

RELPOS (CM)	U (CM/SEC)	ACTPOS (CM)	R/RC	U/UM
61.00	21	4.53	1.74	0.089
60.50	39	4.03	1.55	0.165
59.90	66	3.43	1.32	0.279
59.40	94	2.93	1.12	0.397
58.75	132	2.28	0.88	0.558
58.25	165	1.78	0.68	0.697
57.75	190	1.28	0.49	0.803
57.35	216	0.88	0.34	0.913
56.70	237	0.23	0.09	1.001
56.15	240	-0.32	-0.12	1.014
55.60	225	-0.87	-0.33	0.951
55.10	197	-1.37	-0.53	0.832
54.60	169	-1.87	-0.72	0.714
54.10	136	-2.37	-0.91	0.575
53.60	109	-2.87	-1.10	0.461
53.10	80	-3.37	-1.29	0.338
52.65	59	-3.82	-1.47	0.249
52.00	37	-4.47	-1.71	0.156
51.50	24	-4.97	-1.91	0.101

M/MO= 0.941

CHART 43 Z= 35 CM UO= 475 CM/SEC CONSISTENCY=0.31 PERCENT

UM=177.9 RZ= 46.70 RC= 3.38

RELPOS (CM)	U (CM/SEC)	ACTPOS (CM)	R/RC	U/UM
40.95	24	-5.75	-1.70	0.135
41.55	35	-5.15	-1.52	0.197
41.95	47	-4.75	-1.40	0.264
42.55	62	-4.15	-1.23	0.349
43.00	79	-3.70	-1.09	0.444
43.40	90	-3.30	-0.98	0.506
43.95	110	-2.75	-0.81	0.618
44.45	128	-2.25	-0.67	0.720
44.90	143	-1.80	-0.53	0.804
45.30	155	-1.40	-0.41	0.871
45.70	165	-1.00	-0.30	0.928
46.05	172	-0.65	-0.19	0.967
46.35	176	-0.35	-0.10	0.989
46.90	181	0.20	0.06	1.018
47.30	177	0.60	0.18	0.995
47.85	166	1.15	0.34	0.933
48.45	149	1.75	0.52	0.838
49.00	131	2.30	0.68	0.736
49.65	107	2.95	0.87	0.602
50.25	85	3.55	1.05	0.478
50.65	68	3.95	1.17	0.382
51.05	57	4.35	1.29	0.320
51.80	37	5.10	1.51	0.208

M/MO= 0.895

CHART 42 Z= 45 CM UO= 475 CM/SEC CONSISTENCY=0.31 PERCENT

UM=140.3 RZ= 36.60 RC= 4.09

RELPOS (CM)	U (CM/SEC)	ACTPOS (CM)	R/RC	U/UM
42.20	37	5.60	1.37	0.264
41.60	49	5.00	1.22	0.349
41.10	62	4.50	1.10	0.442
40.55	75	3.95	0.97	0.535
39.95	89	3.35	0.82	0.634
39.35	103	2.75	0.67	0.734
38.75	117	2.15	0.53	0.834
38.35	123	1.75	0.43	0.877
37.85	132	1.25	0.31	0.941
37.25	139	0.65	0.16	0.991
36.80	141	0.20	0.05	1.005
36.30	140	-0.30	-0.07	0.998
35.80	135	-0.80	-0.20	0.962
35.15	127	-1.45	-0.35	0.905
34.40	114	-2.20	-0.54	0.813
33.70	97	-2.90	-0.71	0.691
33.05	83	-3.55	-0.87	0.592
32.50	71	-4.10	-1.00	0.506
31.90	57	-4.70	-1.15	0.406
31.25	41	-5.35	-1.31	0.292

M/MO= 0.814

CHART 41 Z= 55 CM UO= 475 CM/SEC CONSISTENCY-0.31 PERCENT

UM=113.8 RZ= 26.70 RC= 4.78

RELPOS (CM)	U (CM/SEC)	ACTPOS (CM)	R/RC	U/UM	NORMAL
20.00	30	-6.70	-1.40	0.264	
20.50	37	-6.20	-1.30	0.325	
20.95	43	-5.75	-1.20	0.378	
21.45	49	-5.25	-1.10	0.430	
21.90	58	-4.80	-1.00	0.510	
22.30	64	-4.40	-0.92	0.562	
22.80	73	-3.90	-0.81	0.641	
23.25	79	-3.45	-0.72	0.694	
23.90	89	-2.80	-0.58	0.782	
24.50	98	-2.20	-0.46	0.861	
25.00	105	-1.70	-0.35	0.922	
25.45	108	-1.25	-0.26	0.949	
25.90	112	-0.80	-0.17	0.984	
26.45	114	-0.25	-0.05	1.001	
26.80	114	0.10	0.02	1.001	
27.20	113	0.50	0.10	0.993	
27.70	111	1.00	0.21	0.975	
28.25	106	1.55	0.32	0.931	
28.75	100	2.05	0.43	0.878	
29.35	90	2.65	0.55	0.791	
29.85	84	3.15	0.66	0.738	
30.35	77	3.65	0.76	0.676	
30.80	68	4.10	0.86	0.597	
31.30	59	4.60	0.96	0.518	
31.85	50	5.15	1.08	0.439	
32.40	41	5.70	1.19	0.360	
32.80	35	6.10	1.28	0.307	

M/MO= 0.733

CHART 37 Z= 25 CM UO= 475 CM/SEC CONSISTENCY-0.46 PERCENT

UM=231.0 RZ= 56.57 RC= 2.57

RELPOS (CM)	U (CM/SEC)	ACTPOS (CM)	R/RC	U/UM
52.20	33	-4.37	-1.70	0.143
52.55	43	-4.02	-1.56	0.186
53.00	63	-3.57	-1.39	0.273
53.50	84	-3.07	-1.19	0.364
53.80	101	-2.77	-1.08	0.437
54.10	122	-2.47	-0.96	0.528
54.45	144	-2.12	-0.82	0.623
54.80	166	-1.77	-0.69	0.719
55.10	186	-1.47	-0.57	0.805
55.45	199	-1.12	-0.43	0.862
55.75	215	-0.82	-0.32	0.931
56.15	228	-0.42	-0.16	0.987
56.45	233	-0.12	-0.05	1.009
57.05	228	0.48	0.19	0.987
57.65	204	1.08	0.42	0.883
58.05	182	1.48	0.58	0.788
58.45	155	1.88	0.73	0.671
58.80	135	2.23	0.87	0.585
59.20	110	2.63	1.03	0.476
59.45	99	2.88	1.12	0.429
59.75	81	3.18	1.24	0.351
60.15	62	3.58	1.40	0.268
60.50	44	3.93	1.53	0.191

M/MO= 0.869

CHART 38 Z= 35 CM UO= 475 CM/SEC CONSISTENCY=0.46 PERCENT

UM=173.0 RZ= 46.68 RC= 3.32

RELPOS (CM)	U (CM/SEC)	ACTPOS (CM)	R/RC	U/UM
51.80	33	5.12	1.54	0.191
51.40	43	4.72	1.42	0.249
51.00	54	4.32	1.30	0.312
50.50	68	3.82	1.15	0.393
50.10	82	3.42	1.03	0.474
49.65	99	2.97	0.90	0.572
49.30	111	2.62	0.79	0.642
48.90	125	2.22	0.67	0.723
48.55	138	1.87	0.57	0.798
48.35	145	1.67	0.50	0.838
47.80	159	1.12	0.34	0.919
47.30	169	0.62	0.19	0.977
47.00	172	0.32	0.10	0.994
46.70	174	0.02	0.01	1.006
46.35	171	-0.33	-0.10	0.988
45.95	167	-0.73	-0.22	0.965
45.30	154	-1.38	-0.41	0.890
44.90	143	-1.78	-0.53	0.827
44.35	125	-2.33	-0.70	0.723
44.05	113	-2.63	-0.79	0.653
43.55	93	-3.13	-0.94	0.538
43.10	78	-3.58	-1.08	0.451
42.80	67	-3.88	-1.17	0.387

CHART 39 Z= 45 CM UO= 475 CM/SEC CONSISTENCY=0.46 PERCENT

UM=138.9 RZ= 36.72 RC= 3.97

RELPOS (CM)	U (CM/SEC)	ACTPOS (CM)	R/RC	U/UM
31.20	37	-5.52	-1.39	0.266
31.50	43	-5.22	-1.31	0.309
32.00	54	-4.72	-1.19	0.389
32.55	65	-4.17	-1.05	0.468
32.90	73	-3.82	-0.96	0.525
33.30	84	-3.42	-0.86	0.605
33.80	96	-2.92	-0.74	0.691
34.30	107	-2.42	-0.61	0.770
34.80	119	-1.92	-0.48	0.856
35.30	128	-1.42	-0.36	0.921
35.95	135	-0.77	-0.19	0.972
36.50	139	-0.22	-0.06	1.000
37.00	139	0.28	0.07	1.000
37.45	135	0.73	0.18	0.972
38.15	127	1.43	0.36	0.914
38.45	122	1.73	0.44	0.878
38.90	111	2.18	0.55	0.799
39.20	105	2.48	0.62	0.756
39.65	94	2.93	0.74	0.677
40.10	85	3.38	0.85	0.612
40.65	70	3.93	0.99	0.504
41.20	58	4.48	1.13	0.417
41.60	49	4.88	1.23	0.353
42.05	39	5.33	1.34	0.281
42.55	27	5.83	1.47	0.194

M/MO= 0.753

CHART 40 Z= 55 CM UO= 475 CM/SEC CONSISTENCY=0.46 PERCENT

UM=111.7 RZ= 26.80 RC= 4.76

RELPOS (CM)	U (CM/SEC)	ACTPOS (CM)	R/RC	U/UM
32.55	39	5.75	1.21	0.349
32.10	47	5.30	1.11	0.421
31.65	54	4.85	1.02	0.484
31.20	61	4.40	0.92	0.546
30.65	70	3.85	0.81	0.627
29.90	83	3.10	0.65	0.743
29.35	91	2.55	0.54	0.815
28.90	97	2.10	0.44	0.869
28.25	105	1.45	0.31	0.940
27.80	108	1.00	0.21	0.967
27.35	111	0.55	0.12	0.994
26.90	112	0.10	0.02	1.003
26.45	111	-0.35	-0.07	0.994
26.05	110	-0.75	-0.16	0.985
25.65	107	-1.15	-0.24	0.958
24.80	100	-2.00	-0.42	0.896
24.30	91	-2.50	-0.52	0.815
23.85	86	-2.95	-0.62	0.770
23.35	78	-3.45	-0.72	0.699
22.65	67	-4.15	-0.87	0.600
22.05	57	-4.75	-1.00	0.510
21.35	46	-5.45	-1.14	0.412
20.60	35	-6.20	-1.30	0.313

M/MO= 0.699

CHART 36 Z= 25 CM UO= 383 CM/SEC CONSISTENCY=0.75 PERCENT

UM=180.4 RZ= 56.47 RC= 2.52

RELPOS (CM)	U (CM/SEC)	ACTPOS (CM)	R/RC	U/UM
60.60	24	4.13	1.64	0.133
60.25	39	3.78	1.50	0.216
59.95	49	3.48	1.38	0.272
59.55	61	3.08	1.22	0.338
59.15	81	2.68	1.06	0.449
58.90	101	2.43	0.96	0.560
58.60	109	2.13	0.85	0.604
57.95	140	1.48	0.59	0.776
57.60	156	1.13	0.45	0.865
57.30	168	0.83	0.33	0.931
56.95	177	0.48	0.19	0.981
56.50	183	0.03	0.01	1.014
55.90	173	-0.57	-0.23	0.959
55.40	157	-1.07	-0.43	0.870
55.10	144	-1.37	-0.54	0.798
54.80	134	-1.67	-0.66	0.743
54.40	113	-2.07	-0.82	0.626
54.00	94	-2.47	-0.98	0.521
53.60	75	-2.87	-1.14	0.416
53.05	49	-3.42	-1.36	0.272

M/MO= 0.785

CHART 24 Z= 35 CM UO= 383 CM/SEC CONSISTENCY=0.75 PERCENT

UM=131.3 RZ= 48.31 RC= 3.28

RELPOS (CM)	U (CM/SEC)	ACTPOS (CM)	R/RC	U/UM
43.50	29	-4.81	-1.47	0.221
44.00	39	-4.31	-1.32	0.297
44.35	48	-3.96	-1.21	0.366
44.75	58	-3.56	-1.09	0.442
45.45	78	-2.86	-0.87	0.594
46.05	94	-2.26	-0.69	0.716
46.75	109	-1.56	-0.48	0.830
47.10	119	-1.21	-0.37	0.906
47.70	128	-0.61	-0.19	0.975
48.30	131	-0.01	-0.00	0.998
49.00	130	0.69	0.21	0.990
49.50	121	1.19	0.36	0.922
50.10	107	1.79	0.54	0.815
50.40	98	2.09	0.64	0.747
51.40	71	3.09	0.94	0.541
51.95	55	3.64	1.11	0.419
52.60	41	4.29	1.31	0.312
52.90	35	4.59	1.40	0.267

M/MO= 0.704

CHART 23 Z= 45 CM UO= 383 CM/SEC CONSISTENCY=0.75 PERCENT

GUESS UM=103.2 RZ= 38.30 RC= 3.94

RELPOS (CM)	U (CM/SEC)	ACTPOS (CM)	R/RC	U/UM
44.50	18	6.20	1.57	0.174
44.05	24	5.75	1.46	0.233
43.70	28	5.40	1.37	0.271
43.30	34	5.00	1.27	0.330
43.00	39	4.70	1.19	0.378
42.45	48	4.15	1.05	0.465
42.20	52	3.90	0.99	0.504
41.60	62	3.30	0.84	0.601
41.25	70	2.95	0.75	0.678
40.70	80	2.40	0.61	0.775
40.20	88	1.90	0.48	0.853
39.70	95	1.40	0.36	0.921
39.15	100	0.85	0.22	0.969
38.85	102	0.55	0.14	0.989
38.55	103	0.25	0.06	0.998
38.05	103	-0.25	-0.06	0.998
37.70	101	-0.60	-0.15	0.979
37.45	100	-0.85	-0.22	0.969
36.90	94	-1.40	-0.35	0.911
36.20	85	-2.10	-0.53	0.824
35.70	76	-2.60	-0.66	0.737
34.95	63	-3.35	-0.85	0.611
34.20	49	-4.10	-1.04	0.475
33.75	41	-4.55	-1.15	0.397
33.25	33	-5.05	-1.28	0.320
32.60	24	-5.70	-1.45	0.233
32.30	21	-6.00	-1.52	0.204

M/MO= 0.629

CHART 31 Z= 55 CM UO= 383 CM/SEC CONSISTENCY=0.75 PERCENT

UM= 85.3 RZ= 26.86 RC= 4.70

RELPOS (CM)	U (CM/SEC)	ACTPOS (CM)	R/RC	U/UM
19.90	19	-6.96	-1.48	0.223
20.70	27	-6.16	-1.31	0.317
21.55	36	-5.31	-1.13	0.422
22.20	44	-4.66	-0.99	0.516
22.65	49	-4.21	-0.89	0.575
23.15	55	-3.71	-0.79	0.645
23.80	64	-3.06	-0.65	0.751
24.40	71	-2.46	-0.52	0.833
24.90	76	-1.96	-0.42	0.891
25.40	80	-1.46	-0.31	0.938
25.95	83	-0.91	-0.19	0.973
26.55	85	-0.31	-0.07	0.997
26.80	85	-0.06	-0.01	0.997
27.25	85	0.39	0.08	0.997
27.75	83	0.89	0.19	0.973
28.35	80	1.49	0.32	0.938
28.85	75	1.99	0.42	0.880
29.50	68	2.64	0.56	0.798
30.00	62	3.14	0.67	0.727
30.65	54	3.79	0.81	0.633
31.15	47	4.29	0.91	0.551
31.75	40	4.89	1.04	0.469
32.50	30	5.64	1.20	0.352

M/MO= 0.611

CHART 35 Z= 25 CM UO= 475 CM/SEC CONSISTENCY=0.75 PERCENT

UM=228.9 RZ= 56.50 RC= 2.49

RELPOS (CM)	U (CM/SEC)	ACTPOS (CM)	R/RC	U/UM
52.05	26	-4.45	-1.79	0.114
52.40	36	-4.10	-1.65	0.157
52.75	49	-3.75	-1.51	0.214
53.30	75	-3.20	-1.29	0.328
53.70	94	-2.80	-1.13	0.411
54.00	112	-2.50	-1.01	0.489
54.40	140	-2.10	-0.84	0.612
54.85	166	-1.65	-0.66	0.725
55.40	198	-1.10	-0.44	0.865
55.80	215	-0.70	-0.28	0.939
56.10	226	-0.40	-0.16	0.987
56.40	230	-0.10	-0.04	1.005
56.80	228	0.30	0.12	0.996
57.20	217	0.70	0.28	0.948
57.65	199	1.15	0.46	0.869
58.15	168	1.65	0.66	0.734
58.50	146	2.00	0.80	0.638
58.95	115	2.45	0.99	0.502
59.40	90	2.90	1.17	0.393
59.70	71	3.20	1.29	0.310
59.95	59	3.45	1.39	0.258
60.30	46	3.80	1.53	0.201
60.60	35	4.10	1.65	0.153

M/MO= 0.801

CHART 32 Z= 35 CM UO= 475 CM/SEC CONSISTENCY=0.75 PERCENT

UM=168.4 RZ= 47.10 RC= 3.17

RELPOS (CM)	U (CM/SEC)	ACTPOS (CM)	R/RC	U/UM
52.10	30	5.00	1.58	0.178
51.20	52	4.10	1.29	0.309
50.10	91	3.00	0.95	0.540
49.65	108	2.55	0.81	0.641
49.10	128	2.00	0.63	0.760
48.55	146	1.45	0.46	0.867
47.95	161	0.85	0.27	0.956
47.45	167	0.35	0.11	0.992
47.05	168	-0.05	-0.02	0.998
46.60	165	-0.50	-0.16	0.980
45.95	153	-1.15	-0.36	0.909
45.45	139	-1.65	-0.52	0.826
45.00	124	-2.10	-0.66	0.736
44.55	107	-2.55	-0.81	0.636
44.05	89	-3.05	-0.96	0.529
43.65	73	-3.45	-1.09	0.434
43.10	56	-4.00	-1.26	0.333
42.70	44	-4.40	-1.39	0.261
42.20	31	-4.90	-1.55	0.184

M/MO= 0.702

CHART 26 Z= 45 CM UO= 475 CM/SEC CONSISTENCY=0.75 PERCENT

UM=131.5 RZ= 38.30 RC= 3.95

RELPOS (CM)	U (CM/SEC)	ACTPOS (CM)	R/RC	U/UM
32.35	26	-5.95	-1.50	0.198
33.15	41	-4.15	-1.30	0.312
33.70	52	-4.60	-1.16	0.396
34.35	66	-3.95	-1.00	0.502
34.90	78	-3.40	-0.86	0.593
35.50	92	-2.80	-0.71	0.700
36.10	106	-2.20	-0.56	0.806
36.60	115	-1.70	-0.43	0.875
36.95	121	-1.35	-0.34	0.920
37.40	127	-0.90	-0.23	0.966
38.00	131	-0.30	-0.08	0.996
38.65	131	0.35	0.09	0.996
39.15	128	0.85	0.21	0.974
39.60	122	1.30	0.33	0.928
40.15	113	1.85	0.47	0.859
40.60	104	2.30	0.58	0.791
41.30	88	3.00	0.76	0.669
41.70	79	3.40	0.86	0.601
42.30	65	4.00	1.01	0.494
42.90	52	4.60	1.16	0.396
43.40	41	5.10	1.29	0.312
43.95	33	5.65	1.43	0.251
44.30	26	6.00	1.52	0.198

M/MO= 0.668

CHART 30 Z= 55 CM UO= 475 CM/SEC CONSISTENCY=0.75 PERCENT

UM=108.8 RZ= 26.90 RC= 4.66

RELPOS (CM)	U (CM/SEC)	ACTPOS (CM)	R/RC	U/UM
33.20	30	6.30	1.35	0.276
32.60	39	5.70	1.22	0.358
32.10	44	5.20	1.12	0.404
31.45	54	4.55	0.98	0.496
31.00	62	4.10	0.88	0.570
30.50	71	3.60	0.77	0.653
29.80	83	2.90	0.62	0.763
29.20	93	2.30	0.49	0.855
28.70	99	1.80	0.39	0.910
28.00	105	1.10	0.24	0.965
27.40	109	0.50	0.11	1.002
26.95	109	0.05	0.01	1.002
26.25	107	-0.65	-0.14	0.983
25.65	103	-1.25	-0.27	0.947
25.10	98	-1.80	-0.39	0.901
24.60	91	-2.30	-0.49	0.836
23.80	80	-3.10	-0.66	0.735
23.30	71	-3.60	-0.77	0.653
22.50	61	-4.40	-0.94	0.561
21.75	47	-5.15	-1.10	0.432
21.10	39	-5.80	-1.24	0.358
20.40	30	-6.50	-1.39	0.276
19.90	24	-7.00	-1.50	0.221

M/MO= 0.637

CHART 34 Z= 25 CM UO= 538 CM/SEC CONSISTENCY=0.75 PERCENT

UM=274.5 RZ= 56.50 RC= 2.46

RELPOS (CM)	U (CM/SEC)	ACTPOS (CM)	R/RC	U/UM
60.90	24	4.40	1.79	0.087
60.35	49	3.85	1.56	0.179
59.90	72	3.40	1.38	0.262
59.55	94	3.05	1.24	0.342
59.05	130	2.55	1.04	0.474
58.70	157	2.20	0.89	0.572
58.35	186	1.85	0.75	0.678
57.95	215	1.45	0.59	0.783
57.25	254	0.75	0.30	0.925
56.90	269	0.40	0.16	0.980
56.40	274	-0.10	-0.04	0.998
55.95	266	-0.55	-0.22	0.969
55.35	237	-1.15	-0.47	0.863
54.95	209	-1.55	-0.63	0.761
54.40	168	-2.10	-0.85	0.612
54.20	152	-2.30	-0.93	0.554
53.70	114	-2.80	-1.14	0.415
53.20	81	-3.30	-1.34	0.295
52.75	56	-3.75	-1.52	0.204
52.40	39	-4.10	-1.66	0.142

M/MO= 0.880

CHART 33 Z= 35 CM UO= 538 CM/SEC CONSISTENCY=0.75 PERCENT

UM=200.2 RZ= 47.10 RC= 3.13

RELPOS (CM)	U (CM/SEC)	ACTPOS (CM)	R/RC	U/UM
41.90	27	-5.20	-1.66	0.135
42.45	44	-4.65	-1.48	0.220
43.05	64	-4.05	-1.29	0.320
43.40	77	-3.70	-1.18	0.385
43.85	96	-3.25	-1.04	0.480
44.20	111	-2.90	-0.93	0.555
44.60	129	-2.50	-0.80	0.644
44.95	142	-2.15	-0.69	0.709
45.35	161	-1.75	-0.56	0.804
46.15	188	-0.95	-0.30	0.939
46.50	195	-0.60	-0.19	0.974
46.90	199	-0.20	-0.06	0.994
47.35	199	0.25	0.08	0.994
47.75	195	0.65	0.21	0.974
48.20	184	1.10	0.35	0.919
48.75	165	1.65	0.53	0.824
49.10	151	2.00	0.64	0.754
49.65	127	2.55	0.81	0.634
49.95	113	2.85	0.91	0.565
50.35	96	3.25	1.04	0.480
50.75	78	3.65	1.16	0.390
51.20	62	4.10	1.31	0.310
51.60	47	4.50	1.44	0.235
51.90	36	4.80	1.53	0.180

M/MO= 0.758

CHART 27 Z= 45 CM UO= 538 CM/SEC CONSISTENCY=0.75 PERCENT

UM=157.3 RZ= 38.10 RC= 3.82

RELPOS (CM)	U (CM/SEC)	ACTPOS (CM)	R/RC	U/UM
44.30	25	6.20	1.62	0.159
43.70	36	5.60	1.47	0.229
43.00	51	4.90	1.28	0.324
42.60	61	4.50	1.18	0.388
42.00	77	3.90	1.02	0.490
41.60	88	3.50	0.92	0.560
41.00	105	2.90	0.76	0.668
40.60	117	2.50	0.65	0.744
39.75	138	1.65	0.43	0.877
39.25	148	1.15	0.30	0.941
38.90	153	0.80	0.21	0.973
38.40	157	0.30	0.08	0.998
37.90	157	-0.20	-0.05	0.998
37.40	153	-0.70	-0.18	0.973
36.90	147	-1.20	-0.31	0.935
36.30	134	-1.80	-0.47	0.852
35.55	115	-2.55	-0.67	0.731
35.05	101	-3.05	-0.80	0.642
34.35	81	-3.75	-0.98	0.515
33.85	67	-4.25	-1.11	0.426
33.20	50	-4.90	-1.28	0.318
32.85	42	-5.25	-1.37	0.267
32.10	25	-6.00	-1.57	0.159

M/MO= 0.696

CHART 29 Z= 55 CM UO= 538 CM/SEC CONSISTENCY=0.75 PERCENT

UM=127.0 RZ= 26.90 RC= 4.58

RELPOS (CM)	U (CM/SEC)	ACTPOS (CM)	R/RC	U/UM
20.40	31	-6.50	-1.42	0.244
20.90	38	-6.00	-1.31	0.299
21.35	45	-5.55	-1.21	0.354
22.00	58	-4.90	-1.07	0.457
22.60	69	-4.30	-0.94	0.543
23.10	77	-3.80	-0.83	0.606
23.60	87	-3.30	-0.72	0.685
24.15	100	-2.75	-0.60	0.787
24.60	106	-2.30	-0.50	0.835
25.30	117	-1.60	-0.35	0.921
25.90	123	-1.00	-0.22	0.968
26.40	126	-0.50	-0.11	0.992
26.90	126	-0.00	-0.00	0.992
27.40	126	0.50	0.11	0.992
27.85	123	0.95	0.21	0.968
28.50	117	1.60	0.35	0.921
28.95	110	2.05	0.45	0.866
29.40	104	2.50	0.55	0.819
29.90	96	3.00	0.66	0.756
30.60	82	3.70	0.81	0.646
31.10	71	4.20	0.92	0.559
31.40	65	4.50	0.98	0.512
32.10	52	5.20	1.14	0.409
32.70	42	5.80	1.27	0.331
33.20	34	6.30	1.38	0.268

M/MO= 0.651

VELOCITY PROFILES

Water

Measured velocity profiles

u_{o_1} = 383 cm/sec	Fig. 44
u_{o_1} = 475	Fig. 17 (page 77)
u_{o_1} = 538	Fig. 45

Reduced velocity profiles

u_{o_1} = 383 cm/sec	Fig. 46
u_{o_1} = 475	Fig. 18 (page 78)
u_{o_1} = 538	Fig. 47

0.75% Consistency

Measured velocity profiles

u_{o_1} = 383 cm/sec	Fig. 48
u_{o_1} = 475	Fig. 20 (page 82)
u_{o_1} = 538	Fig. 49

Reduced velocity profiles

u_{o_1} = 383 cm/sec	Fig. 50
u_{o_1} = 475	Fig. 21 (page 83)
u_{o_1} = 538	Fig. 51

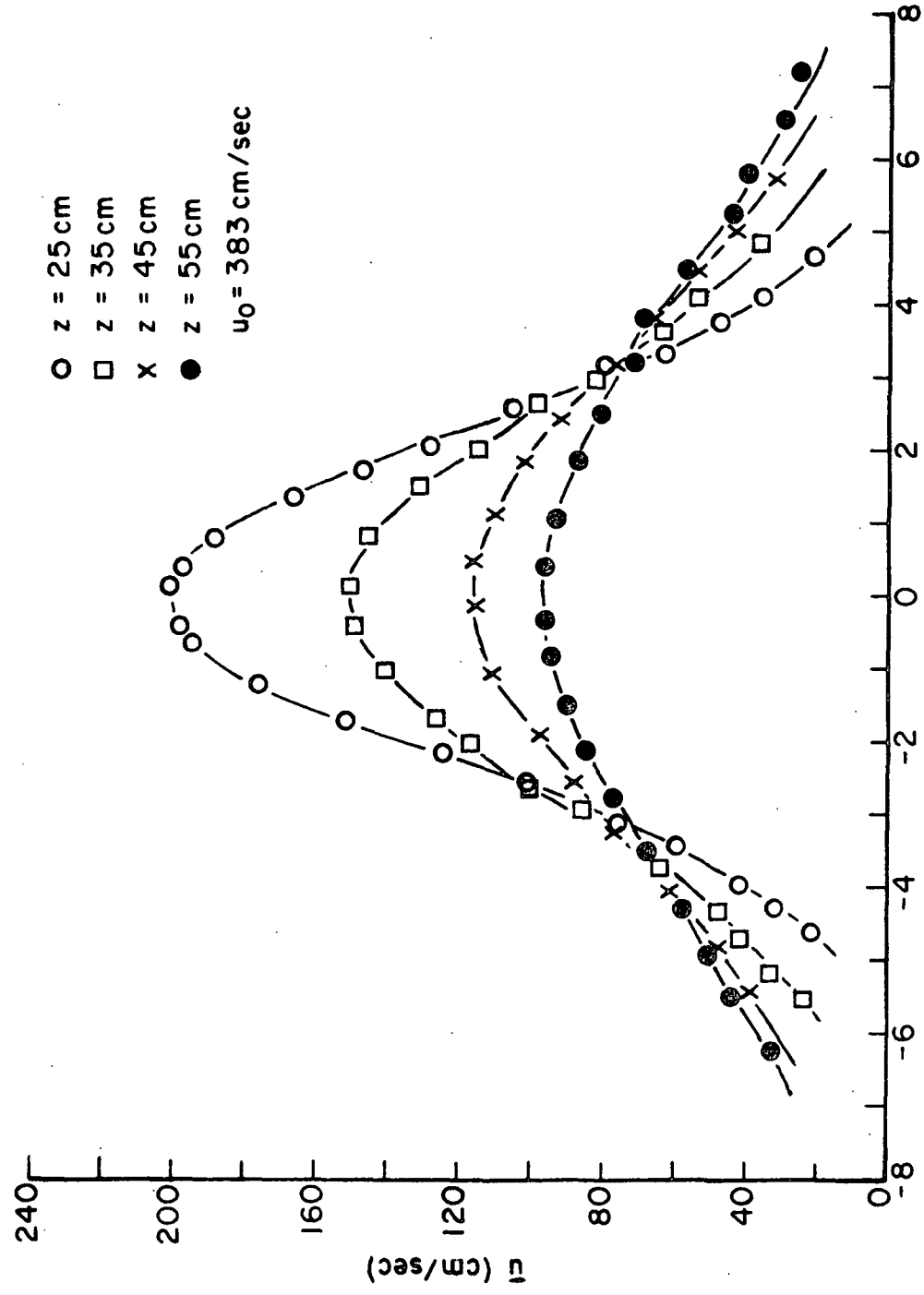

Figure 44. Velocity Profiles, 0% Consistency

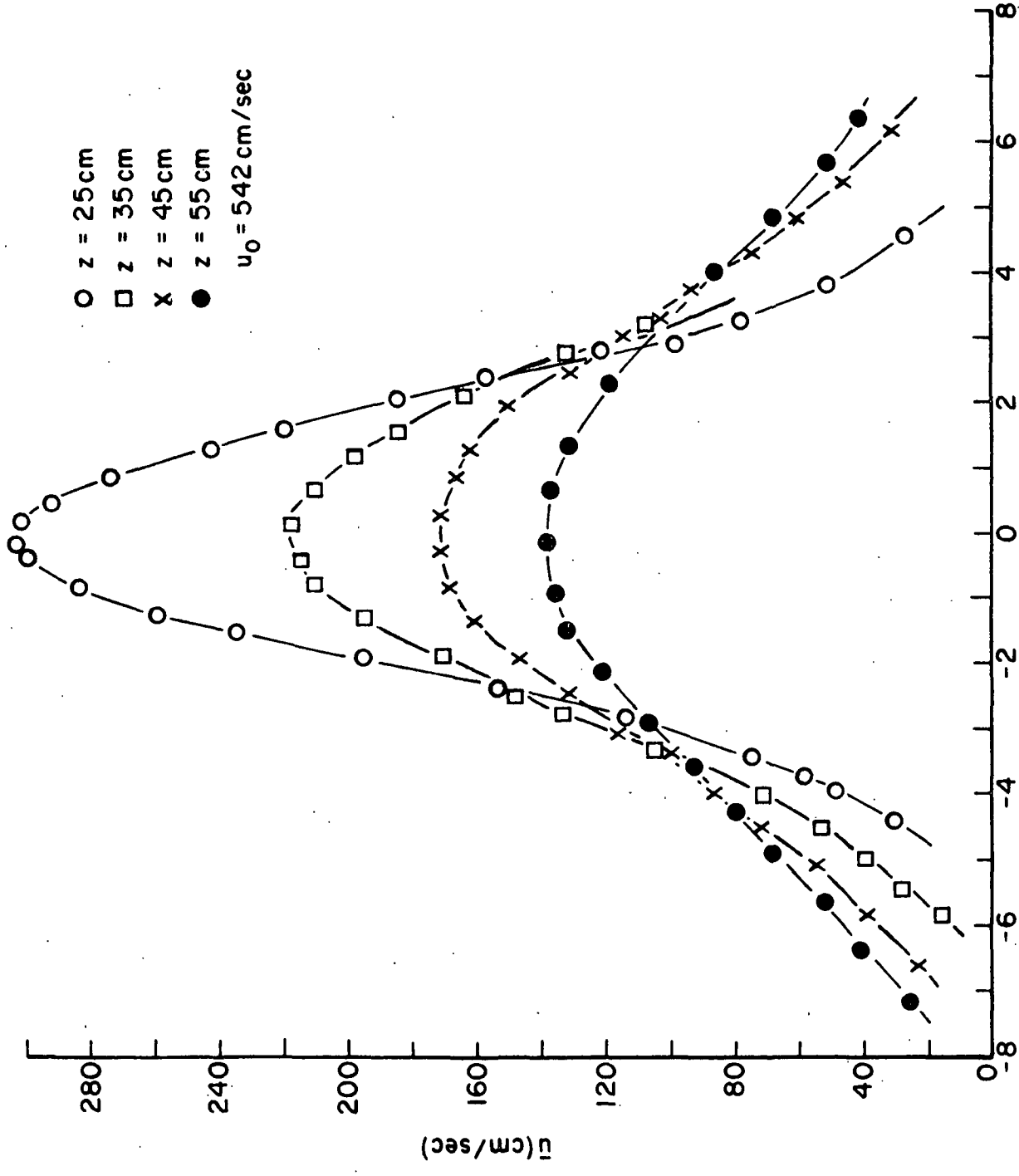

Figure 45. Velocity Profiles, 0% Consistency

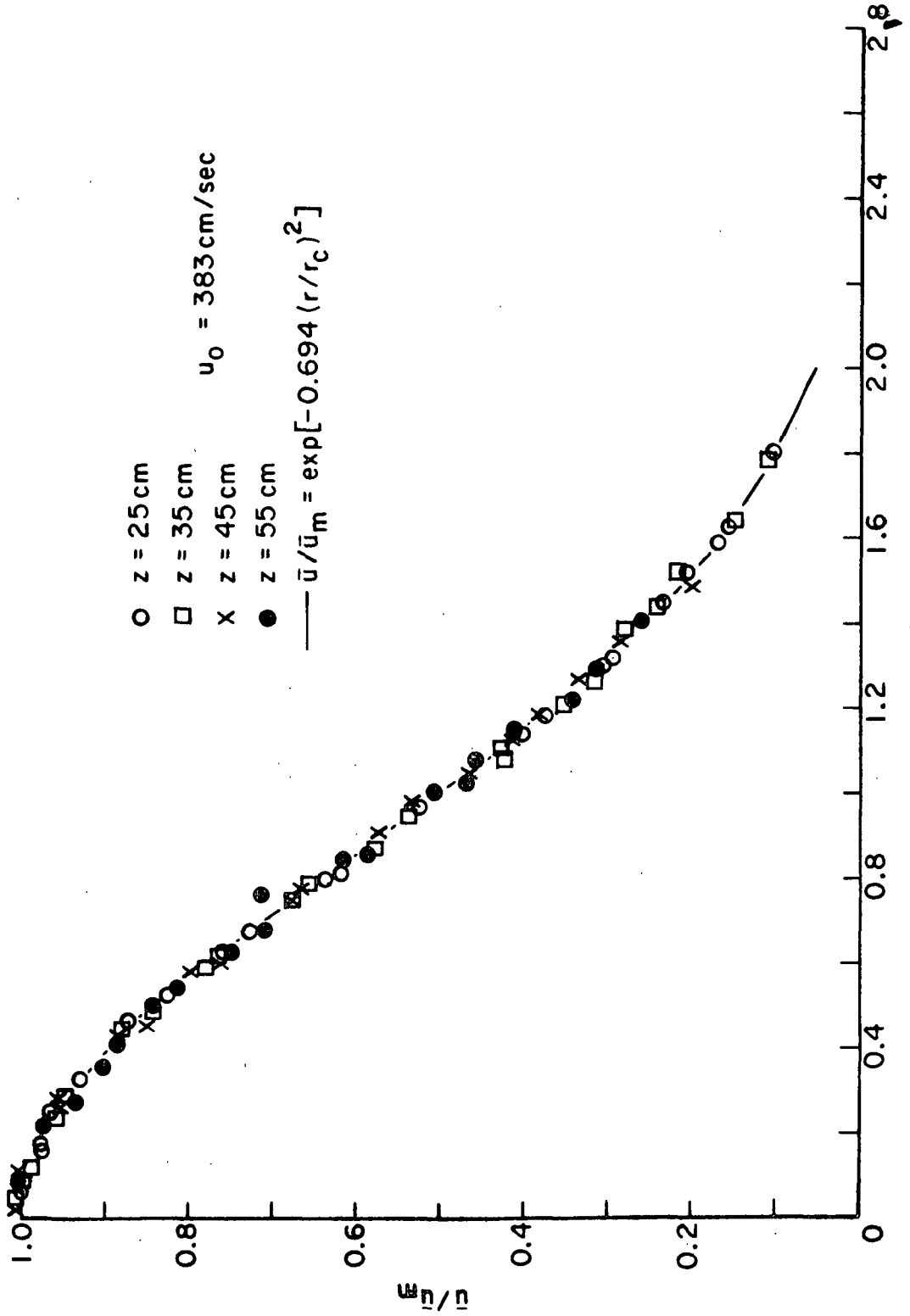

Figure 46. Reduced Velocity Profiles, 0% Consistency

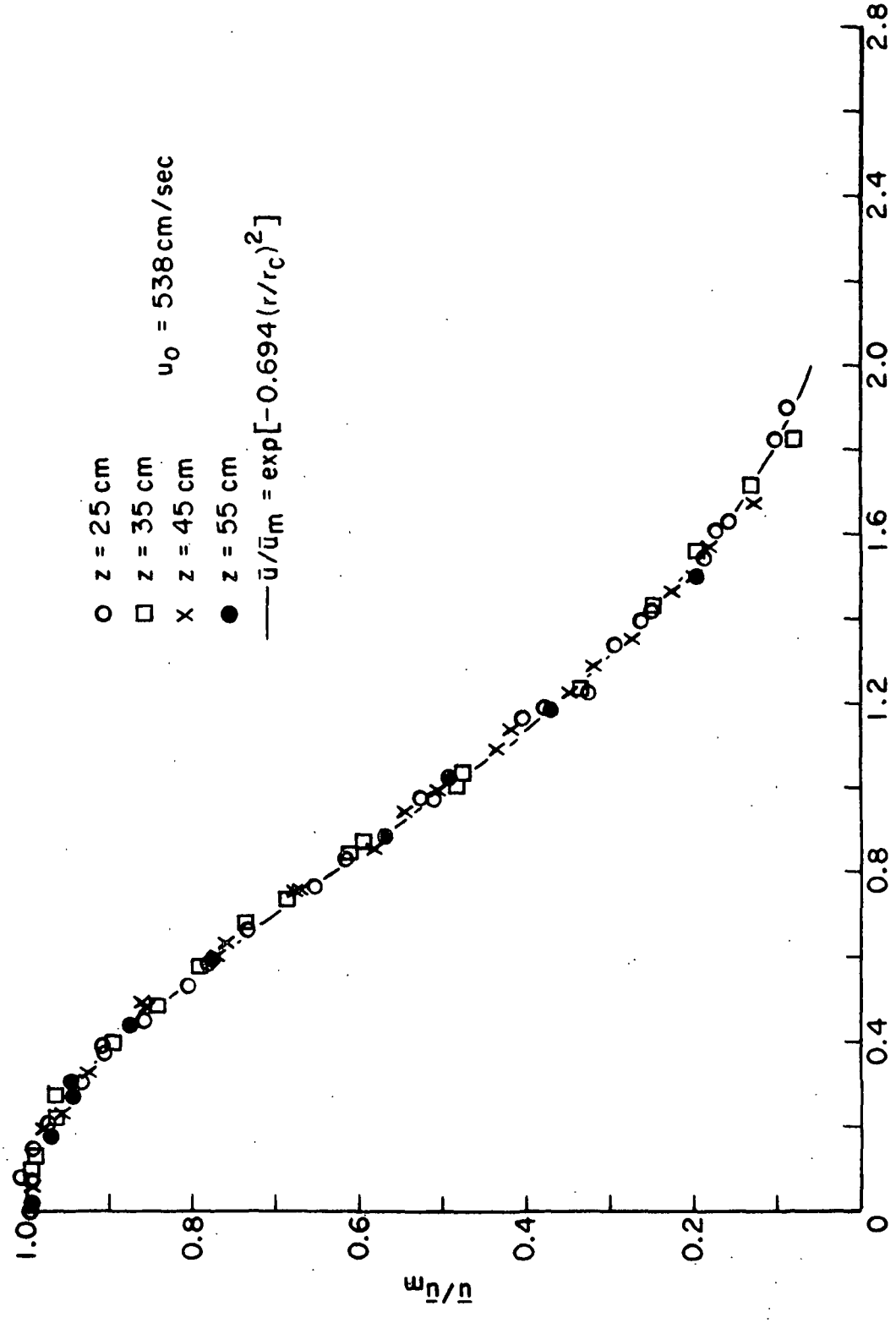

Figure 47. Reduced Velocity Profiles, 0% Consistency

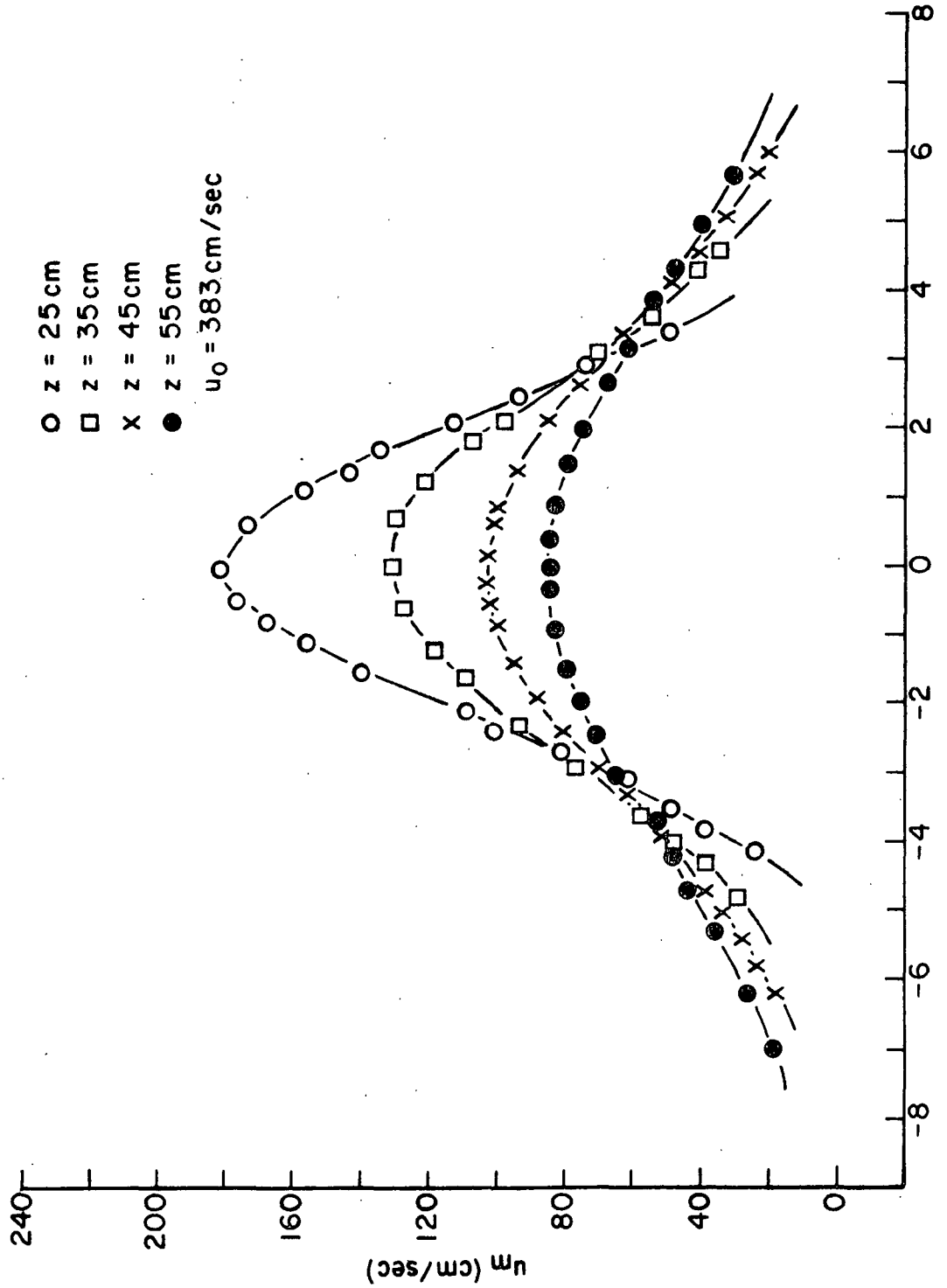

Figure 48. Velocity Profiles, 0.75% Consistency

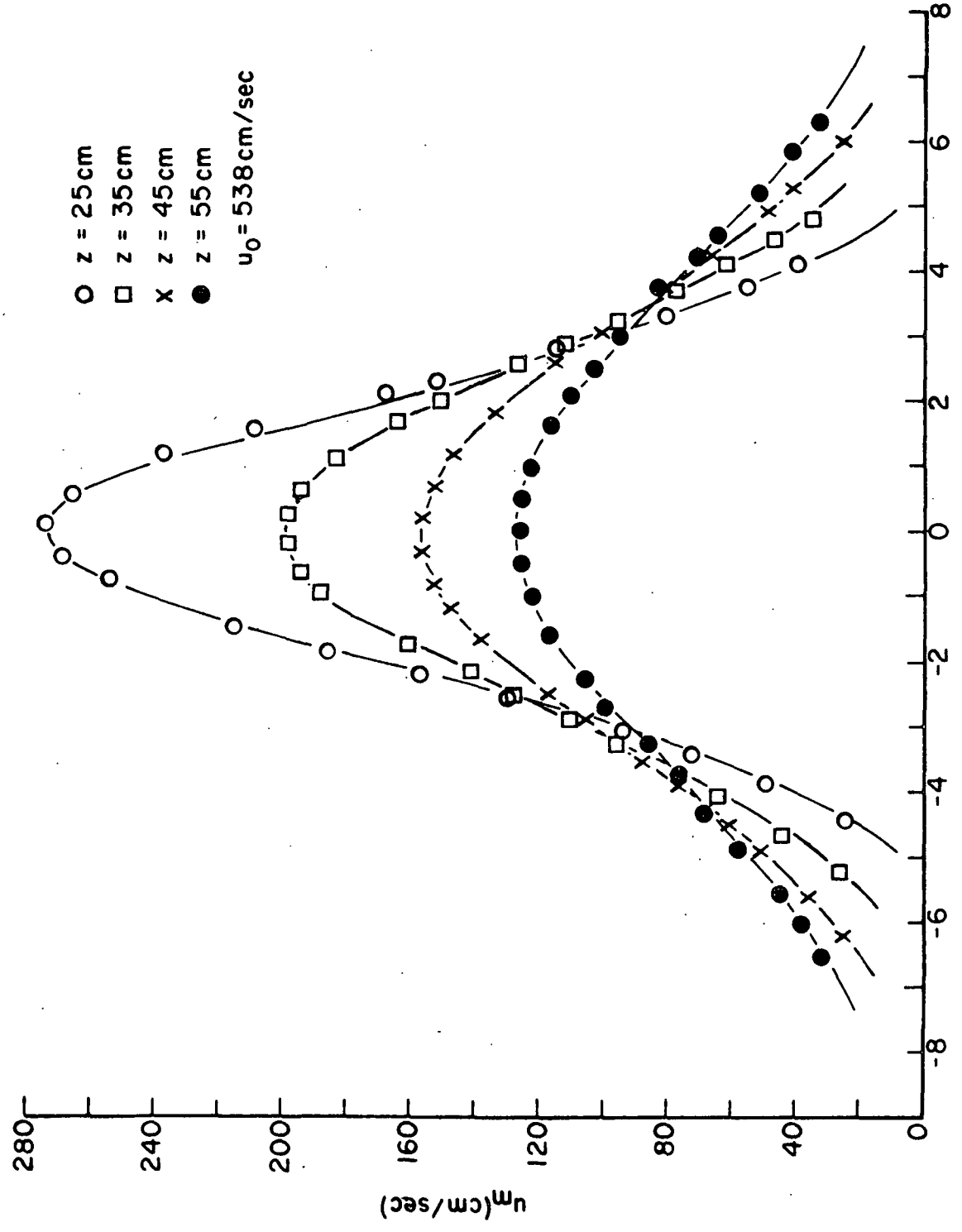

Figure 49. Velocity Profiles, 0.75% Consistency

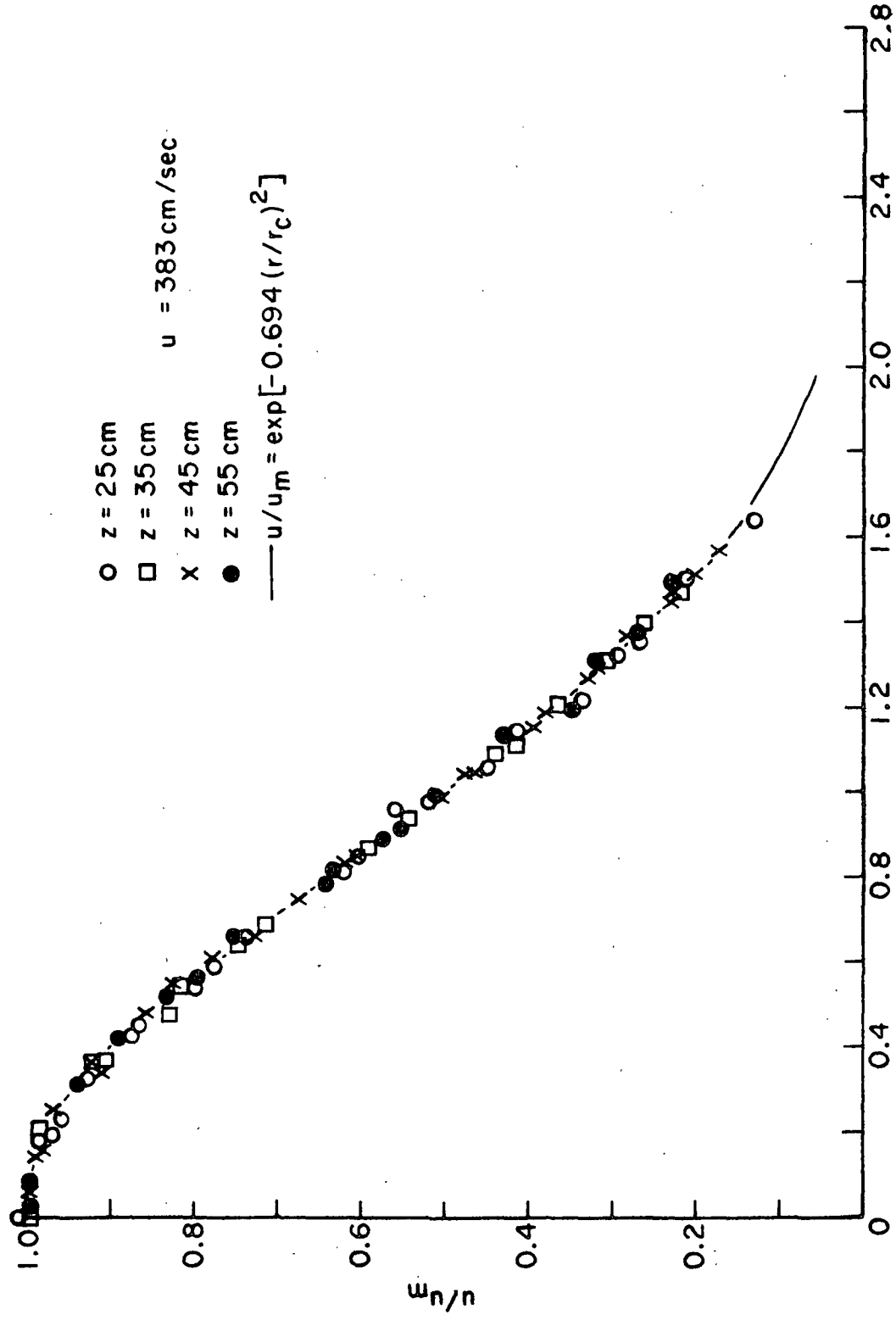

Figure 50. Reduced Velocity Profiles, 0.75% Consistency

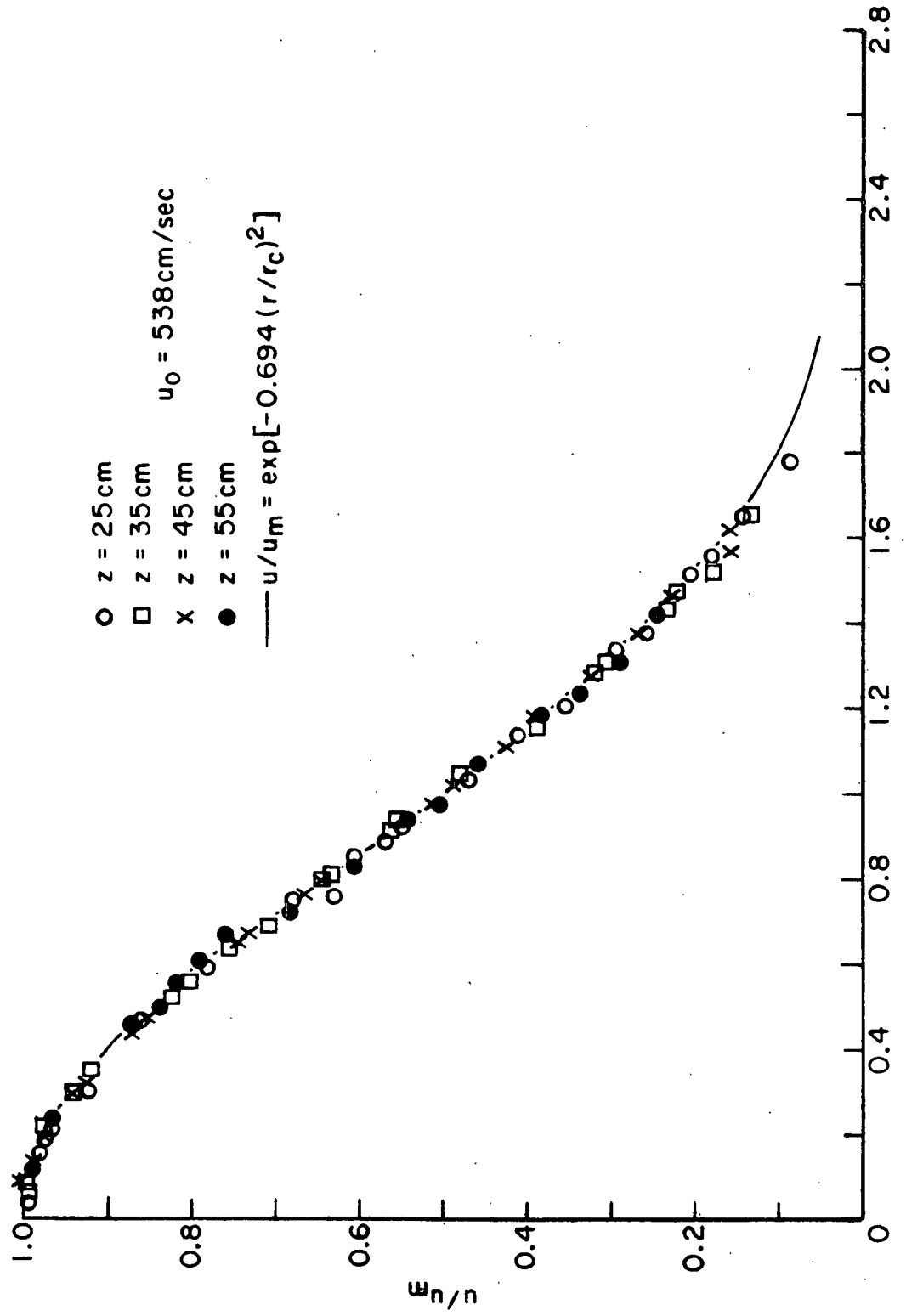

Figure 51. Reduced Velocity Profiles, 0.75% Consistency

APPENDIX VII

CONSISTENCY PROBE MEASUREMENTS

0.30% Consistency
u_o = 383 cm/sec

s = 25 cm

Position	r(cm)	Reading
39.8	-4.2	0.320
40.5	-3.5	0.325
41.2	-2.8	0.330
42.0	-2.0	0.335
42.7	-1.3	0.340
43.5	-0.5	0.345
44.2	0.2	0.345
45.0	1.0	0.345
45.7	1.7	0.345
46.5	2.5	0.340
47.2	3.2	0.335
48.0	4.0	0.325

s = 35 cm

Position	r(cm)	Reading
40.5	5.0	0.335
39.8	4.3	0.340
39.0	3.5	0.345
38.2	2.7	0.345
37.5	2.0	0.345
36.8	1.3	0.350
36.0	0.5	0.350
35.2	-0.3	0.350
34.5	-1.0	0.350
33.7	-1.8	0.350
33.0	-2.5	0.345
32.3	-3.2	0.345
31.6	-3.9	0.340
30.8	-4.7	0.335
30.1	-5.4	0.330

s = 45 cm

Position	r(cm)	Reading
20.0	-5.5	0.345
20.8	-4.7	0.350
21.6	-3.9	0.350
22.3	-3.2	0.350
23.0	-2.5	0.350
23.8	-1.7	0.355
24.5	-1.0	0.355
25.2	-0.3	0.355
26.0	0.5	0.355
26.8	1.3	0.355
27.5	2.0	0.355
28.2	2.7	0.355
29.0	3.5	0.355
29.8	4.3	0.355
30.6	5.1	0.355
31.3	5.8	0.350

s = 55 cm

Position	r(cm)	Reading
22.2	6.7	0.360
21.4	5.9	0.360
20.7	5.2	0.360
20.0	4.5	0.360
19.2	3.7	0.360
18.4	2.9	0.360
17.6	2.1	0.360
16.9	1.4	0.360
16.1	0.6	0.360
15.3	0.2	0.360
14.6	-0.9	0.360
13.8	-1.7	0.360
13.0	-2.5	0.360
12.3	-3.2	0.360
11.5	-4.0	0.355
10.8	-4.7	0.355
10.0	-5.5	0.355
9.2	-6.3	0.355

0.30% Consistency
u_o = 475 cm/sec

s = 25 cm

Position	r(cm)	Reading
39.5	-4.0	0.315
40.2	-3.3	0.320
41.0	-2.5	0.325
41.7	-1.8	0.330
42.4	-1.1	0.340
43.1	-0.4	0.345
43.8	0.3	0.345
44.6	1.1	0.345
45.2	1.7	0.340
45.9	2.4	0.340
46.6	3.1	0.335
47.4	3.9	0.325
48.1	4.6	0.320

s = 35 cm

Position	r(cm)	Reading
41.2	6.2	0.330
40.5	5.5	0.330
39.8	4.8	0.335
39.0	4.0	0.335
38.3	3.3	0.340
37.6	2.6	0.340
36.9	1.9	0.345
36.1	1.1	0.345
35.3	0.3	0.345
34.5	-0.5	0.345
33.7	-1.3	0.340
33.0	-2.0	0.340
32.3	-2.7	0.335
31.6	-3.4	0.335
30.9	-4.1	0.330
30.0	-5.0	0.330

s = 45 cm

19.2	-5.8	0.335
20.1	-4.9	0.340
20.9	-4.1	0.345
21.7	-3.3	0.350
22.5	-2.5	0.350
23.2	-1.8	0.350
24.0	-1.0	0.350
24.7	-0.3	0.355
25.5	0.5	0.355
26.3	1.3	0.355
27.0	2.0	0.350
27.7	2.7	0.350
28.5	3.5	0.350
29.3	4.3	0.345
30.1	5.1	0.340
30.9	5.9	0.335
31.7	6.7	0.335

s = 55 cm

21.8	6.7	0.360
21.0	5.9	0.360
20.3	5.2	0.365
19.6	4.5	0.365
18.9	3.8	0.365
18.1	3.0	0.365
17.3	2.2	0.365
16.5	1.4	0.365
15.8	0.7	0.365
15.1	0	0.365
14.4	-0.7	0.360
13.7	-1.4	0.360
13.0	-2.1	0.360
12.3	-2.8	0.360
11.5	-3.6	0.360
10.9	-4.2	0.355
10.0	-5.1	0.350
9.2	-5.9	0.350

0.30% Consistency
u_o = 538 cm/sec

s = 25 cm			s = 35 cm		
Position	r(cm)	Reading	Position	r(cm)	Reading
48.0	4.5	0.330	30.7	-4.8	0.335
47.2	3.7	0.335	31.4	-4.1	0.340
46.5	3.0	0.340	32.2	-3.3	0.345
45.8	2.3	0.345	33.0	-2.5	0.350
45.0	1.5	0.345	33.7	-1.8	0.350
44.3	0.8	0.345	34.5	-1.0	0.350
43.5	0	0.350	35.3	-0.2	0.355
42.7	-0.8	0.345	36.0	0.5	0.350
42.0	-1.5	0.345	36.7	1.2	0.350
41.3	-2.2	0.345	37.4	1.9	0.350
40.5	-3.0	0.340	38.2	2.7	0.350
39.7	-3.8	0.330	39.0	3.5	0.345
39.0	-4.5	0.325	39.9	4.4	0.345
			40.6	5.1	0.340
s = 45 cm			s = 55 cm		
31.7	6.2	0.355	9.0	-6.5	0.355
31.0	5.5	0.355	9.7	-5.8	0.355
30.3	4.8	0.355	10.5	-5.0	0.355
29.5	4.0	0.355	11.2	-4.3	0.355
28.7	3.2	0.355	12.0	-3.5	0.355
28.0	2.5	0.355	12.7	-2.8	0.355
27.3	1.8	0.355	13.4	-2.1	0.355
26.7	1.2	0.355	14.2	-1.3	0.360
26.0	0.5	0.360	14.9	-0.6	0.355
25.2	-0.3	0.360	15.7	0.2	0.360
24.7	-0.8	0.360	16.4	0.9	0.355
24.0	-1.5	0.355	17.1	1.6	0.355
23.2	-2.3	0.355	17.8	2.3	0.360
22.5	-3.0	0.355	18.6	3.1	0.360
21.8	-3.7	0.355	19.3	3.8	0.360
21.0	-4.5	0.350	20.0	4.5	0.355
20.2	-5.3	0.350	20.8	5.3	0.355
19.4	-6.1	0.345	21.5	6.0	0.355
			22.2	6.7	0.355

0.47% Consistency
u_o = 383 cm/sec

s = 25 cm			s = 35 cm		
Position	r(cm)	Reading	Position	r(cm)	Reading
38.4	-4.6	0.480	40.1	5.1	0.490
39.1	-3.9	0.485	39.2	4.2	0.500
39.9	-3.1	0.490	38.5	3.5	0.505
40.7	-2.3	0.495	37.7	2.7	0.510
41.4	-1.6	0.500	37.0	2.0	0.510
42.1	-0.9	0.505	36.2	1.2	0.510
42.8	-0.2	0.510	35.4	0.4	0.515
43.5	0.5	0.510	34.7	-0.3	0.515
44.2	1.2	0.510	34.0	-1.0	0.515
45.0	2.0	0.505	33.2	-1.8	0.510
45.7	2.7	0.500	32.5	-2.5	0.510
46.4	3.4	0.500	31.7	-3.3	0.500
47.1	4.1	0.490	30.9	-4.1	0.495
47.8	4.8	0.485	30.0	-5.0	0.490
s = 45 cm			s = 55 cm		
19.4	-5.6	0.500	22.4	7.4	0.520
20.1	-4.9	0.505	21.6	6.6	0.520
20.9	-4.1	0.510	20.9	5.9	0.520
21.7	-3.3	0.510	20.1	5.1	0.520
22.5	-2.5	0.510	19.3	4.3	0.520
23.3	-1.7	0.510	18.5	3.5	0.520
24.0	-1.0	0.510	17.7	2.7	0.520
24.7	-1.3	0.515	17.0	2.0	0.520
25.5	0.5	0.515			
26.2	1.2	0.515			
27.0	2.0	0.515			
27.7	2.7	0.515			
28.5	3.5	0.515			
29.3	4.3	0.515			
30.0	5.0	0.510			
30.8	5.8	0.510			

0.47% Consistency
u_o = 475 cm/sec

s = 25 cm			s = 35 cm		
Position	r(cm)	Reading	Position	r(cm)	Reading
47.4	4.4	0.490	30.0	-5.5	0.480
46.7	3.7	0.495	30.8	-4.7	0.480
46.0	3.0	0.500	31.7	-3.8	0.485
45.4	2.4	0.505	32.4	-3.1	0.495
44.7	1.7	0.505	33.0	-2.5	0.495
43.9	0.9	0.510	33.8	-1.7	0.500
43.1	0.1	0.510	34.5	-1.0	0.505
42.3	-0.7	0.505	35.2	-0.3	0.505
41.5	-1.5	0.500	36.0	0.5	0.505
40.7	-2.3	0.490	36.7	1.2	0.500
40.0	-3.0	0.480	37.4	1.9	0.495
39.1	-3.9	0.480	38.1	2.6	0.495
38.4	-4.6	0.480	38.8	3.3	0.485
			39.5	4.0	0.480
			40.3	4.8	0.480
			41.0	5.5	0.480
s = 45 cm			s = 55 cm		
31.2	6.2	0.500	9.0	-6.0	0.505
30.4	5.4	0.500	9.7	-5.3	0.505
29.7	4.7	0.505	10.6	-4.4	0.510
29.0	4.0	0.505	11.3	-3.7	0.510
28.2	3.2	0.505	12.1	-2.9	0.515
27.5	2.5	0.505	12.9	-2.1	0.515
26.7	1.7	0.505	13.7	-1.3	0.515
26.0	1.0	0.505	14.5	-0.5	0.515
25.2	0.2	0.510	15.2	0.2	0.515
24.5	-0.5	0.510	16.0	1.0	0.515
23.7	-1.3	0.510	16.7	1.7	0.515
23.0	-2.0	0.510	17.5	2.5	0.515
22.2	-2.8	0.505	18.2	3.2	0.515
21.4	-3.6	0.505	19.0	4.0	0.515
20.7	-4.3	0.500	19.7	4.7	0.515
19.9	-5.1	0.500	20.5	5.5	0.510
			21.2	6.2	0.510
			22.0	7.0	0.505

0.47% Consistency
u_o = 538 cm/sec

s = 25 cm

Position	r(cm)	Reading
48.8	5.3	0.490
48.0	4.5	0.485
47.3	3.8	0.490
46.7	3.2	0.500
46.0	2.5	0.500
45.2	1.7	0.500
44.4	0.9	0.505
43.6	0.1	0.505
42.8	-0.7	0.510
42.2	-1.3	0.505

s = 35 cm

Position	r(cm)	Reading
30.1	-5.4	0.510
30.8	-4.7	0.510
31.6	-3.9	0.515
32.4	-3.1	0.515
33.2	-2.3	0.515
34.0	-1.5	0.515
34.8	-0.7	0.515
35.5	0	0.515
36.3	0.8	0.515
37.0	1.5	0.520
37.6	2.1	0.515
38.3	2.8	0.515
39.0	3.5	0.515
39.7	4.2	0.515
40.5	5.0	0.510
41.2	5.7	0.505

s = 45 cm

31.0	6.0	0.540
30.1	5.1	0.540
29.4	4.4	0.540
28.8	3.8	0.535
28.0	3.0	0.535
27.3	2.3	0.535
26.5	1.5	0.530
25.6	0.6	0.530
24.9	-0.1	0.530
24.1	-0.9	0.530
23.3	-1.7	0.530
22.5	-2.5	0.530
21.7	-3.3	0.530
21.0	-4.0	0.530
20.3	-4.7	0.530
19.5	-5.5	0.535
18.8	-6.2	0.535

s = 55 cm

49.4	5.9	0.500
48.8	5.3	0.490
48.0	4.5	0.485
47.3	3.8	0.490
46.7	3.2	0.500
46.0	2.5	0.500
45.2	1.7	0.500
44.4	0.9	0.505
43.6	0.1	0.505
42.8	-0.7	0.510
42.2	-1.3	0.505

0.59% Consistency
u_o = 475 cm/sec

s = 25 cm			s = 35 cm		
Position	r(cm)	Reading	Position	r(cm)	Reading
40.2	-4.3	0.565	40.5	5.0	0.590
41.0	-3.5	0.565	39.7	4.2	0.590
41.7	-2.8	0.570	39.0	3.5	0.590
42.5	-2.0	0.575	38.3	2.8	0.590
43.2	-1.3	0.580	37.5	2.0	0.590
44.0	-0.5	0.585	36.8	1.3	0.595
44.8	0.3	0.585	36.0	0.5	0.595
45.5	1.0	0.580	35.2	-0.3	0.600
46.2	1.7	0.575	34.5	-1.0	0.600
47.0	2.5	0.570	33.7	-1.8	0.595
47.7	3.2	0.560	33.0	-2.5	0.590
48.5	4.0	0.560	32.3	-3.2	0.590
49.3	4.8	0.560	31.5	-4.0	0.585
			30.8	-4.7	0.590
			30.0	-5.5	0.580
s = 45 cm			s = 55 cm		
19.2	-6.3	0.610	22.0	6.5	0.630
20.0	-5.5	0.610	21.3	5.8	0.630
20.7	-4.8	0.610	20.5	5.0	0.625
21.5	-4.0	0.610	19.8	4.3	0.625
22.3	-3.2	0.610	19.0	3.5	0.625
23.0	-2.5	0.610	18.3	2.8	0.625
23.7	-1.8	0.605	17.5	2.0	0.620
24.5	-1.0	0.610	16.8	1.3	0.620
25.2	-0.3	0.610	16.0	0.5	0.620
26.0	0.5	0.610	15.2	-0.3	0.620
26.8	1.3	0.610	14.5	-1.0	0.620
27.5	2.0	0.610	13.8	-1.7	0.620
28.2	2.7	0.610	13.0	-2.5	0.620
29.0	3.5	0.615	12.3	-3.2	0.620
29.8	4.3	0.615	11.5	-4.0	0.620
30.6	5.1	0.610	10.8	-4.7	0.620
31.5	6.0	0.605	10.0	-5.5	0.620
			9.2	-6.3	0.620

0.59% Consistency
u_o = 538 cm/sec

s = 25 cm			s = 35 cm		
Position	r(cm)	Reading	Postion	r(cm)	Reading
49.2	4.7	0.570	30.3	-5.2	0.585
48.5	4.0	0.570	31.0	-4.5	0.590
47.8	3.3	0.570	31.8	-3.7	0.595
47.0	2.5	0.575	32.5	-3.0	0.595
46.3	1.8	0.575	33.3	-2.2	0.595
45.5	1.0	0.580	34.0	-1.5	0.600
44.8	0.3	0.585	34.8	-0.7	0.600
44.0	-0.5	0.585	35.5	0	0.600
43.2	-1.3	0.585	36.3	0.8	0.595
42.5	-2.0	0.580	37.0	1.5	0.595
41.7	-2.8	0.575	37.8	2.3	0.595
40.9	-3.6	0.570	38.5	3.0	0.595
40.1	-4.4	0.570	39.3	3.8	0.595
			40.2	4.7	0.590
s = 45 cm			s = 55 cm		
9.0	-6.5	0.625	31.5	6.0	0.610
9.8	-5.7	0.625	30.8	5.3	0.610
10.5	-5.0	0.625	30.0	4.5	0.615
11.3	-4.2	0.625	29.3	3.8	0.610
12.0	-3.5	0.625	28.6	3.1	0.610
12.8	-2.7	0.625	27.9	2.4	0.610
13.5	-2.0	0.620	27.1	1.6	0.610
14.3	-1.2	0.625	26.3	0.8	0.615
15.0	-0.5	0.620	25.5	0	0.610
15.5	0	0.625	24.8	-0.7	0.610
15.8	0.3	0.620	24.0	-1.5	0.610
16.5	1.0	0.625	23.3	-2.2	0.610
17.3	1.8	0.625	22.5	-3.0	0.610
18.1	2.6	0.625	21.8	-3.7	0.610
18.9	3.4	0.625	21.0	-4.5	0.610
19.7	4.2	0.630	20.2	-5.3	0.610
20.5	5.0	0.630	19.5	-6.0	0.610
21.2	5.7	0.630	19.0	-6.5	0.610
22.0	6.5	0.630			

0.73% Consistency
u_o = 383 cm/sec

s = 25 cm

Position	r(cm)	Reading
40.2	-4.3	0.695
41.0	-3.5	0.690
41.7	-2.8	0.690
42.5	-2.0	0.690
43.2	-1.3	0.700
44.0	-0.5	0.700
44.8	0.3	0.700
45.5	1.0	0.700
46.2	1.7	0.695
47.0	2.5	0.695
47.7	3.2	0.690
48.5	4.0	0.685

s = 35 cm

Postion	r(cm)	Reading
40.7	5.2	0.720
40.0	4.5	0.720
39.2	3.7	0.725
38.5	3.0	0.725
37.8	2.3	0.725
37.0	1.5	0.725
36.3	0.8	0.725
35.5	0	0.720
34.8	-0.7	0.720
34.0	-1.5	0.720
33.3	-2.2	0.725
32.6	-2.9	0.720
31.8	-3.7	0.725
31.1	-4.4	0.725
30.4	-5.1	0.720

s = 45 cm

19.8	-5.7	0.750
20.6	-4.9	0.750
21.4	-4.1	0.750
22.1	-3.4	0.750
22.9	-2.6	0.745
23.7	-1.8	0.740
24.5	-1.0	0.740
25.3	-0.2	0.740
26.0	0.5	0.740
26.8	1.3	0.740
27.5	2.0	0.745
28.3	2.8	0.745
29.1	3.6	0.745
29.9	4.4	0.745
30.7	5.2	0.750

s = 55 cm

21.4	5.9	0.750
20.6	5.1	0.760
19.8	4.3	0.760
19.0	3.5	0.765
18.3	2.8	0.765
17.5	2.0	0.765
16.8	1.3	0.760
16.0	0.5	0.755
15.2	-0.3	0.750
14.5	-1.0	0.755
13.7	-1.8	0.750
13.0	-2.5	0.750
12.2	-3.3	0.760
11.4	-4.1	0.755
10.6	-4.9	0.750
9.8	-5.7	0.755

0.73% Consistency
u_o = 475 cm/sec

s = 25 cm			s = 35 cm		
Position	r(cm)	Reading	Position	r(cm)	Reading
48.7	4.2	0.675	30.1	-5.4	0.690
48.0	3.5	0.670	30.9	-4.6	0.695
47.3	2.8	0.670	31.7	-3.8	0.695
46.5	2.0	0.670	32.4	-3.1	0.690
45.8	1.3	0.670	33.1	-2.4	0.690
45.0	0.5	0.675	33.9	-1.6	0.690
44.3	0.2	0.680	34.6	-0.9	0.700
43.6	-0.9	0.680	35.3	-0.2	0.700
42.9	-1.6	0.675	36.0	0.5	0.695
42.1	-2.4	0.665	36.7	1.2	0.695
41.4	-3.1	0.665	37.4	1.9	0.695
40.7	-3.8	0.665	38.2	2.7	0.690
40.0	-4.5	0.660	39.0	3.5	0.690
			39.7	4.2	0.680

s = 45 cm			s = 55 cm		
31.8	6.3	0.720	9.3	-6.2	0.740
31.0	5.5	0.720	10.1	-5.4	0.735
30.2	4.7	0.720	10.9	-4.6	0.735
29.5	4.0	0.720	11.6	-3.9	0.730
28.8	3.3	0.720	12.2	-3.3	0.730
28.0	2.5	0.720	12.9	-2.6	0.730
27.3	1.8	0.720	13.7	-1.8	0.730
26.6	1.1	0.720	14.4	-1.1	0.725
25.9	0.5	0.720	15.2	-0.3	0.730
25.1	-0.4	0.720	16.0	0.5	0.730
24.4	-1.1	0.720	16.7	1.2	0.730
23.6	-1.9	0.720	17.5	2.0	0.730
22.9	-2.6	0.715	18.2	2.7	0.735
22.1	-3.4	0.720	19.0	3.5	0.730
21.4	-4.1	0.720	19.7	4.2	0.730
20.6	-4.9	0.720	20.4	4.9	0.730
19.9	-5.6	0.720	21.2	5.7	0.730
19.1	-6.4	0.720	22.0	6.5	0.730

0.73% Consistency
u_o = 538 cm/sec

s = 25 cm			s = 35 cm		
Position	r(cm)	Reading	Position	r(cm)	Reading
39.0	-5.5	0.670	40.9	5.4	0.700
39.8	-4.7	0.675	40.1	4.6	0.700
40.5	-4.0	0.675	39.3	3.8	0.700
41.2	-3.3	0.675	38.6	3.1	0.700
42.0	-2.5	0.680	38.0	2.5	0.705
42.7	-1.8	0.685	37.2	1.7	0.705
43.5	-1.0	0.685	36.5	1.0	0.700
44.3	-0.2	0.685	35.8	0.3	0.700
45.0	0.5	0.685	35.0	-0.5	0.705
45.7	1.2	0.685	34.2	-1.3	0.700
46.5	2.0	0.680	33.5	-2.0	0.700
47.2	2.7	0.680	32.8	-2.8	0.700
48.0	3.5	0.680	32.0	-3.5	0.700
48.7	4.2	0.675	31.2	-4.3	0.700
49.5	5.0	0.675	30.5	-5.0	0.700
			29.8	-5.7	0.695
s = 45 cm			s = 55 cm		
20.0	-5.5	0.720	22.0	6.5	0.740
20.7	-4.8	0.715	21.2	5.7	0.735
21.5	-4.0	0.715	20.5	5.0	0.735
22.2	-3.3	0.715	19.7	4.2	0.735
23.0	-2.5	0.715	19.0	3.5	0.735
23.8	-1.7	0.715	18.2	2.7	0.730
24.5	-1.0	0.715	17.5	2.0	0.735
25.2	-0.3	0.715	16.7	1.2	0.730
26.0	0.5	0.715	16.0	0.5	0.730
26.8	1.3	0.715	15.2	-0.3	0.730
27.5	2.0	0.715	14.4	-1.1	0.730
28.2	2.7	0.715	13.7	-1.8	0.730
29.0	3.5	0.720	13.0	-2.5	0.730
29.7	4.2	0.720	12.3	-3.2	0.730
30.5	5.0	0.720	11.5	-4.0	0.730
31.3	5.8	0.725	10.8	-4.7	0.730
			10.0	-5.5	0.730
			9.3	-6.2	0.735